

AD-A108 299

UTAH STATE UNIV LOGAN ELECTRO-DYNAMICS LAB
DOWN-LOOKING INTERFEROMETER STUDY II, VOLUME I, (U)
MAR 80 A S ZACHOR
SCIENTIFIC-2

F/G 13/2

F19626-77-C-0203

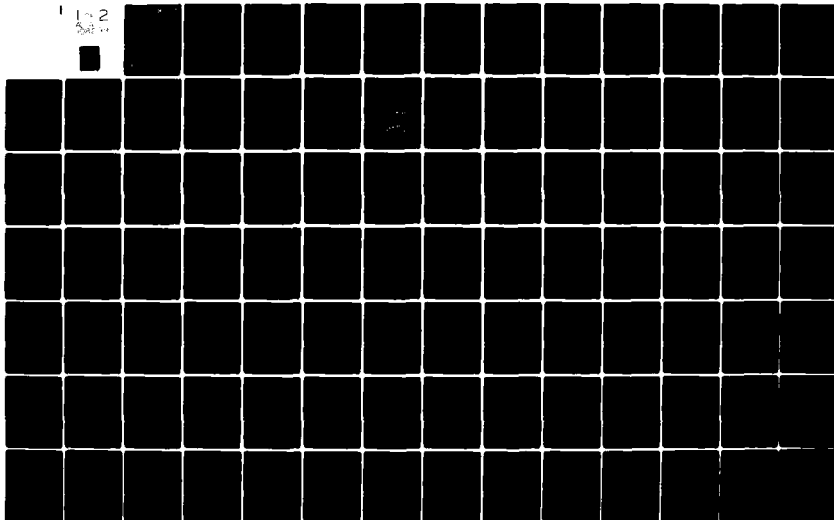
UNCLASSIFIED

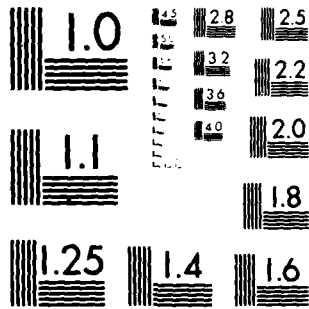
AFGL-TR-80-0236

NL

1-2

Sub





MICROCOPY RESOLUTION TEST CHART
NATIONAL BUREAU OF STANDARDS-1963-A

e
AFGL-TR-80-0236

LEVEL III

(12)

AD A108299

DOWN-LOOKING INTERFEROMETER STUDY II
VOLUME I

ALEXANDER S. ZACHOR

ELECTRO-DYNAMICS LABORATORIES
UTAH STATE UNIVERSITY *123890*
LOGAN, UTAH 84322 *III*

MARCH 1980

SCIENTIFIC REPORT NO. 2

DTIC
ELECTE
S DEC 09 1981 **D**
E

12 11 1980
APPROVED FOR PUBLIC RELEASE; DISTRIBUTION UNLIMITED.

DTIC FILE COPY

AIR FORCE GEOPHYSICS LABORATORY
AIR FORCE SYSTEMS COMMAND
UNITED STATES AIR FORCE
HANSCOM AFB, MASSACHUSETTS 01731

12 11 1980
81 12 08 233

Qualified requestors may obtain additional copies from the Defense Technical Information Center. All others should apply to the National Technical Information Service.

Unclassified

SECURITY CLASSIFICATION OF THIS PAGE (When Data Entered)

REPORT DOCUMENTATION PAGE		READ INSTRUCTIONS BEFORE COMPLETING FORM
1. REPORT NUMBER AFGL-TR-80-0236	2. GOVT ACCESSION NO. 7D-A708	3. RECIPIENT'S CATALOG NUMBER 299
4. TITLE (and Subtitle) DOWN-LOOKING INTERFEROMETER STUDY II VOLUME I		5. TYPE OF REPORT & PERIOD COVERED Scientific Report No. 2
		6. PERFORMING ORG. REPORT NUMBER
7. AUTHOR(s) Alexander S. Zachor		8. CONTRACT OR GRANT NUMBER(s) F19628-77-C-0203
9. PERFORMING ORGANIZATION NAME AND ADDRESS Atmospheric Radiation Consultants, Inc. 59 High Street Acton, Massachusetts 01720		10. PROGRAM ELEMENT, PROJECT, TASK AREA & WORK UNIT NUMBERS 62101F 76701QAB
11. CONTROLLING OFFICE NAME AND ADDRESS Air Force Geophysics Laboratory Hanscom AFB, Massachusetts 01731 Monitor/Dean F. Kimball/OPR		12. REPORT DATE March 1980
		13. NUMBER OF PAGES 145
14. MONITORING AGENCY NAME & ADDRESS (if different from Controlling Office) Electro-Dynamics Laboratories Utah State University Logan, Utah 84322		15. SECURITY CLASS. (of this report) Unclassified
		15a. DECLASSIFICATION/DOWNGRADING SCHEDULE
16. DISTRIBUTION STATEMENT (of this Report) Approved for public release; distribution unlimited.		
17. DISTRIBUTION STATEMENT (of the abstract entered in Block 20, if different from Report)		
18. SUPPLEMENTARY NOTES		
19. KEY WORDS (Continue on reverse side if necessary and identify by block number) Atmospheric transmission, interferometer spectrometers, spectral correlation techniques, minor contaminant species detection.		
20. ABSTRACT (Continue on reverse side if necessary and identify by block number) This study defines parametrically the capability of a high-flying spectrometer system to detect and characterize particular gaseous emissions by ground level stationary sources. The systems considered utilize a Fourier Transform Spectrometer (FTS) employing mosaic focal planes together with optical designs or data processing techniques that effect "background subtraction". Detection and quantification are based on the correlation of the observed target spectral contrast with predicted target spectral signatures.		

DD FORM 1 JAN 73 1473 EDITION OF 1 NOV 65 IS OBSOLETE

Unclassified

SECURITY CLASSIFICATION OF THIS PAGE (When Data Entered)

PREFACE

I am grateful to AFGL personnel, especially to Drs. A. T. Stair and Frank DelGreco for their guidance and encouragement, to Dr. Shepard Clough and Jim Chetwynd, Jr. for providing the FASCOD1 computer program (and instructions in its use), to Dr. Larry Rothman and Bill Gallery for providing other codes/data, and to Drs. George Vanasse and Jim Bunting for useful discussions. ARC was assisted by Bartlett Systems, Inc. in selecting the baseline configurations (Section 3), and was provided detector data by Mike Anapol of SSG, Inc. The Aerospace Corporation provided calculations and measurements of the spectral absorption coefficients of some of the target gases. The unflagging interest and organizational skills of "Tom" were an inspiration in this effort, and are gratefully acknowledged. This effort was performed for Utah State University (under subcontract SC-79-012 and U.S. Air Force prime contract F19628-77-C-0203), and was monitored by the Air Force Geophysics Laboratory. Mr. Dean Kimball was the contract monitor.

Accession For	
NTIS GRA&I	<input checked="checked" type="checkbox"/>
DTIC TAB	<input type="checkbox"/>
Unannounced	<input type="checkbox"/>
Justification	
By _____	
Distribution /	
Availability Codes	
Dist	Special
A	

TABLE OF CONTENTS

	<u>PAGE</u>
SECTION 1 INTRODUCTION AND SUMMARY	1
1.1 Minimum Detectable Quantities	16
1.2 Effects of Uniform Scene Variations	22
1.3 Effects of Spatial Scene Variations	24
1.4 The Scaling Nomographs.	25
SECTION 2 THEORETICAL BASIS.	31
2.1 Notation.	31
2.2 The Observable Quantity	35
2.3 Method of Detection and Quantification.	38
2.4 Computation of Normalized Contrast Spectrum $\tau_v \alpha_{gv}$	50
2.5 Computation of the System \overline{NESR} and Required Dynamic Range.	54
2.6 Basis of the Scaling Nomographs	60
SECTION 3 THE BASELINE SYSTEMS	67
SECTION 4 EFFECTS OF ATMOSPHERIC TRANSMITTANCE (RADIANCE) VARIATIONS AND OFF-NADIR VIEWING	75
4.1 Summary	75
4.2 Details of the Calculations	80
SECTION 5 EFFECTS OF INACCURATE PREDICTIONS OF ATMOSPHERIC AND/OR TARGET GAS ABSORPTIONS, OF SPECTRAL INTER- FERENCES AMONG TARGET SPECIES, AND OF INCOMPLETE BACKGROUND SUBTRACTION	93
5.1 Real-World Effects in the Observed Contrast Spectral Radiance	94
5.2 Generalized Expressions for the Coefficient of Correlation ρ	98

TABLE OF CONTENTS (Continued)

	<u>PAGE</u>
5.3 General Influence of Real-World Effects in p , in the Detection/False Detection Probabilities, and in the Minimum Detectable Quantities.	104
5.4 Modified Detection Procedure.	109
5.5 Interference Model Used to Estimate Revised MDQ's .	112
5.6 Some Revised MDQ's.	114
REFERENCES.	130
APPENDIX A.	131
APPENDIX B.	135

LIST OF ILLUSTRATIONS

<u>FIGURE</u>		<u>PAGE</u>
1.1	SO ₂ ν_1 Band.	10
1.2	P(T T), P(T 0) Nomograph for SO ₂ ν_1 Band	12
1.3	Scaling Nomograph for Band-Average Noise-Equivalent Spectral Radiance ($\overline{\text{NESR}}$)	26
1.4	Scaling Nomograph for Detection Band Required Dynamic Range (DR)	27
2.1	P(T T) versus P(T 0) for Z = 0.5	45
2.2	P(T T) versus P(T 0) for Z = 1.0	46
2.3	P(T T) versus P(T 0) for Z = 1.5	47
2.4	Schematic of an $\overline{\text{NESR}}$ Scaling Nomograph	64
2.5	Schematic of a Dynamic Range Scaling Nomograph	66
3.1	Optical Layout for Baseline Configuration 2.	71
4.1	Meridional Profiles of the Zonal Mean Vertically Integrated Moisture Content [w] for each of the Years Studied	78
4.2	Atmospheric Transmittance of a Vertical Path through the Midlatitude Winter Model Atmosphere and a Path at 45 Degrees Zenith Angle through the Midlatitude Summer Model Atmosphere	83
4.3	Format of Table 4.4 for Relative MDQ Values.	89
5.1	Pdf's of $ \rho $ for the Ideal Case.	105
5.2	Pdf's of $ \rho $; Ideal vs. Non-Ideal Case.	107
5.3	Effects of Strong Atmospheric Lines on the Mean of the Contrast Spectral Radiance	110

LIST OF ILLUSTRATIONS (Continued)

<u>FIGURE</u>		<u>PAGE</u>
5.4	Normalized Contrast Spectral Radiance for the SO_2 ν_1 Band. .	116
5.5	Same as Fig. 5.4 (different conditions).	118
5.6	Same as Fig. 5.4 (different conditions).	120
5.7	Same as Fig. 5.5 (different conditions).	120
5.8	Normalized Contrast Spectral Radiance for the HCL 2900-3000 cm^{-1} Band.	123
5.9	Same as Fig. 5.8 (different conditions).	125
5.10	Normalized Contrast Spectral Radiance for the HBr 2450-2650 cm^{-1} Band.	126
5.11	Same as Fig. 5.10 (different conditions)	128

LIST OF TABLES

<u>TABLE</u>		<u>PAGE</u>
1.1	Selected Baseline Configuration	6
1.2	Radiometric Model of Baseline System.	8
1.3	Detection Parameters for SO_2 ν_1 Band.	11
1.4	Summary of Detection Performance for Bandidate Bands.	17
1.5	Performance Scaled to 10-Second Dwell Time for Candidate Bands	19
1.6	Scaled Performance for "Best" Bands	20
1.7	Summary of Selected Detection Bands, and Performance for 10-Second Dwell Time.	23
1.8	Variation of MDQ Between Midlatitude Winter, $\theta = 0$, and Midlatitude Summer, $\theta = 45^\circ$	24
2.1	Vertical Distributions used for NO , NO_2 and HNO_3	55
3.1	Baseline Configuration 1.	68
3.2	Baseline Configuration 2.	69
4.1	Vertically Integrated Moisture Content w of the LOWTRAN Model Atmospheres	77
4.2	Maximum Variation of MDQ for the Model Atmospheres/ Nadir Angles Considered	78
4.3	Average Atmospheric Spectral Transmission over the Selected Detection Bands for Midlatitude Winter and Summer Model Atmospheres and Nadir View Angles of 0 and 45 Degrees.	81
4.4	Relative MDQ, Band Photon Radiances, and σ' for Midlatitude Winter and Summer Model Atmospheres and for $\theta = 0$ and 45 Degrees.	90

SECTION 1

INTRODUCTION AND SUMMARY

This study has sought to define parametrically the capability of a high-flying spectrometer system to detect and characterize particular gaseous emissions by ground-level stationary sources. The systems considered utilize a Fourier Transform Spectrometer (FTS), although many of the study results are applicable, with suitable redefinition of parameters, to non-multiplexing spectrometers. The baseline systems employ mosaic focal planes together with optical designs or data processing techniques that effect "background subtraction". This is a basic requirement of the sensor because the target spectral emission or absorption is but a small perturbation in the normal background spectrum. Detection and quantification are based on the correlation of the observed target spectral contrast with predicted target spectral signatures. Spectral correlation detection implies a resolution requirement (resolved spectral interval) of the order of 0.1 cm^{-1} , which is the approximate halfwidth of spectral lines in the target emissions and atmospheric interferences.

The system must have a very small instantaneous field-of-view to isolate the target, and a telescope large enough to collect sufficient power for detection. For the IFOV's and telescope sizes envisioned, the $A\Omega$ product, or system throughput, is small compared to that achieved in other, more common, FTS applications; i.e., the system throughput can be accommodated by a Michelson cube with dimensions of one or two inches. However, the FTS system still enjoys a considerable throughput advantage over a grating

spectrometer system.* The system detectors can achieve background-limited performance under typical operating conditions, which negates the FTS "multiplex advantage".

A related hardware development feasibility study performed by SSG, Inc.¹ compared both FTS and grating spectrometer concepts as candidates for this application. The study showed that when the relative throughputs and efficiencies and detector array requirements are compared, the FTS is clearly superior, assuming the detector arrays are representative of current technology. It showed also that the FTS system has sensitivity equal to or better than a grating system even when mosaic array technology beyond the current state-of-the-art is assumed for the grating concepts.

The basic radiometric design requirements and available tradeoffs for this type of FTS application were established in the previous "Down-Looking Interferometer Study".² That study also evaluated some of the impacts of "then-current" technology relative to detectors and A/D converters, and discussed the merits of cooling the system foreoptics. Since it is not generally available, salient points from that report are developed here as needed.

The following were the specific objectives of this study:

- a.) to define several baseline radiometric concepts of a system employing a telescoped, small FOV, state-of-the-art interferometer spectrometer designs, cold-filtered detection bands and a mosaic focal plane of background-limited detectors. The IFOV and telescope sizes were suggested by the Air Force. The selected baselines represent different levels of technology in the optics and focal plane designs.

* With a grating equal in area to the telescope aperture and a required resolving power of 50,000 (0.1 cm^{-1} at 5000 cm^{-1}) the FTS system has a throughput advantage of 30 for the assumed IFOV of 6.56×10^{-4} radians.¹

- b.) to define the performance (achievable noise-equivalent radiance, NESR) of these configurations as a function of design/mission parameters such as IFOV and available measurement time. It was decided subsequently to identify one concept as the baseline configuration, to evaluate its performance, and to provide nomographs that allow performance scaling with respect to basic system design parameters such as collector diameter, IFOV, measurement time, f/number, etc.
- c.) to define a spectral data processing method that promises near optimal performance: maximal false target rejection capability consistent with reasonable detection probability and small uncertainty in the inferred gaseous amounts. This part of the study analyzed a simple technique of normalized spectral correlation, and yielded prescriptions for evaluating detection and false detection probabilities as functions of system NESR, amount of target gas present, threshold value of the correlation coefficient, etc. The computed performance predictions indicate that the selected method is, indeed, very close to optimum.
- d.) to determine a "minimum detectable quantity" of target gas for each of 15 molecular species of interest to the Air Force, and the uncertainty in the deduced amounts. The minimum detectable quantity may be used to determine the molecular column thickness that will yield desired levels of detection and false detection probability for given values of the temperature difference between the gas and the underlying earth background. This part of the effort also determined the best spectral region (absorption band) for the detection of each target species. These initial estimates of minimum detectable quantity and uncertainty ignore all interference effects except detector noise, and assume a particular model for the earth/atmosphere scene.
- e.) to determine how normal variations in the scene model affect the minimum detectable quantities.
- f.) to quantify the effects on minimum detectable quantity of other possible interferences. These interferences include spatial

inhomogeneities in the atmosphere or background (which reduce the effectiveness of the background subtraction techniques), and errors in the predicted atmospheric spectral transmittance and/or target gas spectral absorption coefficient (whose product $\tau_v \alpha_{gv}$ is the spectral correlation reference).

The target species for which minimum detectable quantities were determined are $C_2H_4O_2$, CH_4 , CH_3I , CO , CO_2 , DF , HBr , HCl , HF , HI , HNO_3 , NH_3 , N_2O , NO_2 and SO_2 .

The minimum detectable quantity (MDQ) of target gas is defined as the smallest value of

$$D \equiv Fu\overline{\Delta B}_v(T_g, T_s) \quad (1)$$

that can be detected with high probability (~95 percent) and low false detection probability (~1 percent). In this expression F is the fraction of the IFOV occupied by the target gas cloud, u is the column thickness of the target (molec/cm^2), and $\overline{\Delta B}_v$ is the average Planck spectral radiance difference between the target and the underlying surface, which is determined by the target and surface temperatures, T_g and T_s . The definition of D and MDQ derive from the fact that the observable spectral radiance difference ("contrast") between a part of the scene containing the target and one not containing the target is, ideally,

$$\Delta N_v = D\tau_v \alpha_{gv}, \quad (2)$$

where τ_v is the atmospheric spectral transmittance between the target and sensor, and α_{gv} is the spectral absorption coefficient of the target gas.

Detection of the target gas cloud in an actual mission would consist of first computing the normalized coefficient of spectral correlation ρ ,

defined by

$$\rho \equiv \frac{\text{spectral covariance of } \Delta N_v \text{ and } \tau_v \alpha_{gv}}{(\text{standard deviation of } \Delta N_v) \cdot (\text{standard deviation of } \tau_v \alpha_{gv})} \quad (3)$$

where $\tau_v \alpha_{gv}$ is the "reference spectrum", an estimate of the actual spectrum $\tau_v \alpha_{gv}$. If $|\rho|$ exceeds a predetermined threshold R , the target species would be presumed present. The statistics of $|\rho|$ when the contrast spectral radiance ΔN_v contains system noise (and/or atmospheric/background interferences) determines the probability of detection $P(T|T)$ and the probability of false detection $P(T|0)$. These probabilities vary with the selected threshold R , the number of resolved spectral elements in the detection band, the variance of $\Delta N_v = D\tau_v \alpha_{gv}$ relative to the mean square spectrum noise ($\overline{NESR^2}$), and on several other variances/covariances that characterize atmospheric/background interferences.

The amount D of target gas present is inferred from a least-squares fit of ΔN_v to the reference spectrum $\tau_v \alpha_{gv}$.

The basis of the detection and quantification methods, and the procedures or codes used to obtain $\tau_v \alpha_{gv}$, $P(T|T)$, $P(T|0)$ and the target MDQ's are described in Section 2.

The baseline system configuration used in computing the target MDQ's is described in Section 3 (which refers to the selected concept as baseline Configuration 2). This system configuration uses a four-port Michelson interferometer with two dichroics, which allows the simultaneous observation of up to four different target species. The fourth port (second input port) provides for illumination of the back side of the interferometer beamsplitter by an internal blackbody reference or by a different portion of the external scene than is viewed by the primary input port. This arrangement effects an

optical subtraction (gives the spectral difference of the displaced scenes, or the scene spectrum minus the reference blackbody spectrum), and also a potentially large reduction in the interferogram dynamic range (see Vanasse *et al*³). The basic configuration could also be used without the fourth port. Then, post-detection subtraction of the outputs of different detector pairs would suppress the background (perhaps even more effectively than the four-port optical subtraction), but would not reduce dynamic range in the detector outputs (interferograms).

Table 1.1 lists the gross radiometric parameters that enter into the computation of \overline{NESR} and dynamic range for the selected baseline system. The

Table 1.1 Selected Baseline Configuration

SYSTEM	<p>FOUR-PORT INTERFEROMETER WITH TWO DICHROICS AND FOUR SPECTRALLY OPTIMIZED DETECTOR ARRAYS</p> <p>Resolved spectral interval, $\Delta\nu = 0.1 \text{ cm}^{-1}$ (one-sided interferogram)</p> <p>Spectral range 2.3 - 13 μm</p> <p>Scan time (before scaling) = minimum for BLIP performance</p>
OPTICS	<p>Collector diameter $D = 4$ inches</p> <p>$F\# = 3$</p> <p>IFOV = $0.656 \times 0.656 \text{ mr}$ ($\approx 10 \text{ m}$ footprint at 50,000 foot range)</p> <p>Overall system efficiency $\bar{\xi} = 0.195$</p> <p>Emissivity to detector $\bar{\epsilon} = 0.249$</p> <p>Optics transmission $\tau = 0.261$</p>
DETECTORS	<p>For 3 to 4.8 μm region,</p> <p>$\text{InSb}, \eta = 0.5, D^*f^* = 5 \times 10^{16}$</p> <p>For 7.0 to 12.7 μm region, assume</p> <p>$\text{HgCdTe}, \eta = 0.7, D^*f^* = 8 \times 10^{17}$</p> <p>Element size $x = 9.5 \text{ mils} = 0.24 \text{ mm}$</p> <p>Array size (four arrays), $4 \times 4 = 16$ detectors per array</p>

selection of detector materials, quantum efficiencies η , and D^*f^* is based on Ref. 1. Note that the selection of HgCdTe detectors for the 7.0 - 12.7 μm region is tentative; extrinsic Si:xx detectors (xx = Ga, Bi or As) are also candidates at these wavelengths. Note, also, that the scan time is specified as the minimum corresponding to background-limited detector performance; i.e., the scan time for each detection band corresponds to the frequency $D^*f^*/\text{BLIP } D^*$. This convention is used merely to facilitate scaling of system performance according to a pair of nomographs (see Section 1.4).

Table 1.2 gives the emissivities and loss factors used in the radiometric model of the interferometer, and shows how the effective emissivity $\bar{\epsilon} = 0.249$ was calculated. Note that all losses are represented by emissivities, and that obscurations and back-reflections are represented as elements of unspecified temperature. An example is the secondary mirror and its support structure (spider), which in a Cassegrain telescope system is assumed to obscure 20 percent of the primary. The spider is represented as a black emitter occupying one percent of the clear aperture. The primary and secondary are assumed to have a combined reflectance of 95 percent, or an emissivity of five percent. The dewar window, represented by two elements, has a net transmission, after reflection and absorption losses, of $(1-0.08)(1-0.02) \approx 0.902$, and has an emissivity of 0.02. The contribution of each 300-degree element to the effective system emissivity $\bar{\epsilon}$ is obtained by multiplying its emissivity by the product of transmittances ($1-\epsilon$ values) of the elements between it and the detector. The total optics transmission is simply the product of the $1-\epsilon$ values for all elements.

The computation of the system average noise equivalent radiance $\overline{\text{NESR}}$ for each detection band, and the corresponding dynamic range in the interferogram is described in Section 2.4. These two performance parameters

Table 1.2 Radiometric Model of Baseline System

Optical Element	Emissivity ϵ	Temperature (°K)
1 Spider/secondary obscuration	0.20	--
2 Spider emission	0.01	300
3 Primary and secondary	0.05	300
4 Interferometer (beamsplitter) reflection	0.50	--
5 Beamsplitter emission	0.10	300
6 Interferometer mirrors	0.05	300
7 Dichroic	0.10	300
8 Dewar window loss	0.08	--
9 Dewar window emission	0.02	300
10 Cold shield	--	--
11 Cold filter	0.0	--
12 Detectors	--	(NA)

(2) Spider	$0.01 \times 0.3295 = .0033$
(3) Primary, secondary	$0.05 \times 0.3469 = .0173$
(5) Beamsplitter	$0.10 \times 0.7709 = .0771$
(6) Interferometer mirrors	$0.05 \times 0.8114 = .0406$
(7) Dichroic	$0.10 \times 0.9016 = .0902$
(9) Dewar window	$0.02 \times 1.0 = .02$

EFFECTIVE EMISSIVITY $\bar{\epsilon}$ 0.249

TOTAL OPTICS TRANSMISSION τ 0.261

depend on the detector photon flux density, in addition to the system radiometric parameters given in Tables 1.1 and 1.2. The total detector photon flux density is the sum of the system internal photon flux density to the detector and the external atmosphere-plus-background photon flux density reaching the detector. A pre-release version of the AFGL code FASCOD1 was used to compute the atmosphere/background spectral radiances, which were converted to photon spectral radiances and then integrated to obtain band photon radiances (BPR's). FASCOD1 was also used to obtain the atmospheric spectral transmittance τ_v and, for some of the target species, the spectral absorption coefficient α_{gv} , which are both required in evaluating the MDQ's of the target species (see Section 2.4).

The major results of the study are presented in a standard format, consisting of two figures and one table for each candidate detection band (as many as three different molecular bands or segments of a single band were considered for some of the target molecules). Figure 1.1, Table 1.3, and Fig. 1.2 are a sample of the results; they represent the ν_1 band of SO_2 ($1090\text{--}1210\text{ cm}^{-1}$). Results in this standard format are given in Vol. II for all of the candidate detection bands. All of the tabular/plotted values in Vol. II are based on the Midlatitude Summer model atmosphere (see Ref. 3 and Section 2.4.1), and assume nadir viewing of the target. Also, they assume no atmospheric/background interferences (no spatial variations), and that the reference spectrum $\tau_v \alpha_{gv}$ is known exactly.

The uppermost curve of Fig. 1.1 gives the spectral radiance between 1090 and 1210 cm^{-1} that would be observed by a nadir-viewing sensor viewing a 300K earth surface through a Midlatitude Summer model atmosphere. This radiance corresponds to the case of no SO_2 in the detector field-of-

Figure 1.1 SO_2 ν_1 Band

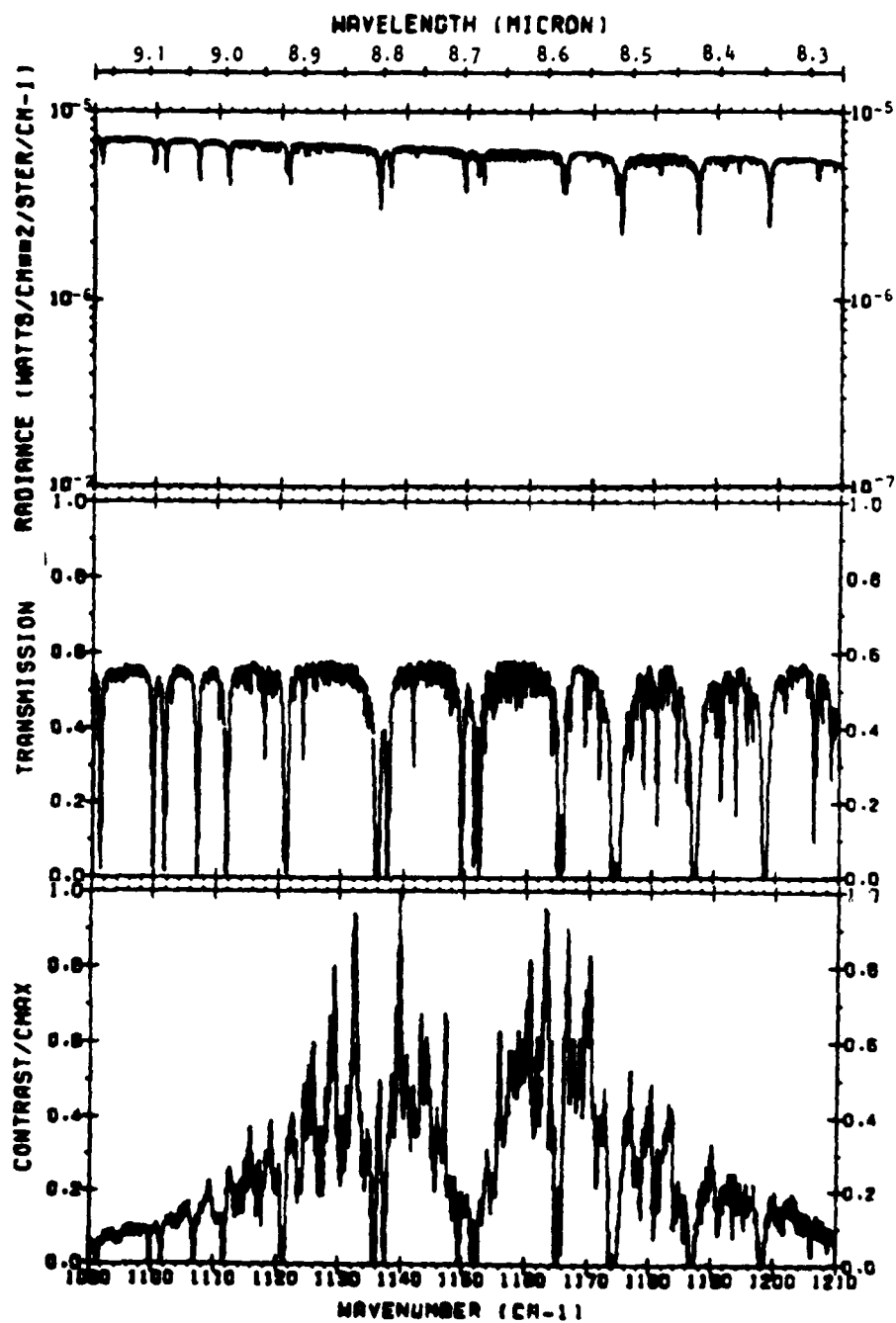
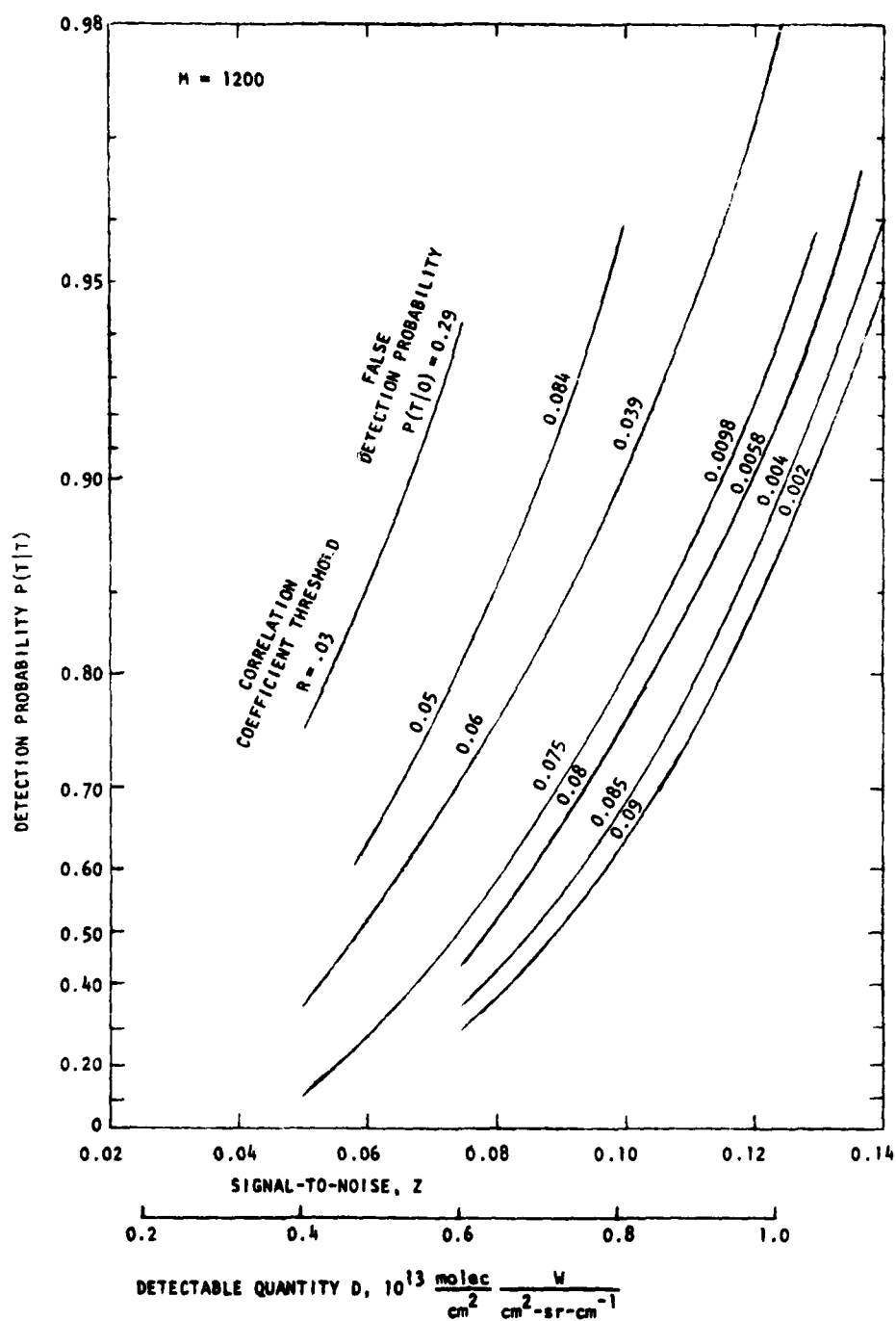


Table 1.3 Detection Parameters for SO₂ ν_1 band

QUANTITY	SYMBOL, VALUE	UNITS
DETECTION BAND	1090-1210	cm ⁻¹
Approximate wavelength	8.7	μm
* NO. OF SPECTRAL ELEMENTS (for $\Delta\nu = 0.10$)	M = 1200	
BAND PHOTON RADIANCE (scene)	3.18×10^{16}	ph/sec cm ² sr
Maximum of contrast $\tau_v \alpha_{gv}$	C _{MAX} = 5.13×10^{-20}	cm ² /molec
Mean contrast	$\mu' = 1.30 \times 10^{-20}$	cm ² /molec
STANDARD DEVIATION OF CONTRAST	$\sigma' = 9.61 \times 10^{-21}$	cm ² /molec
<hr/>		
* Photon flux density on detector		
* from scene.	7.3×10^{14}	phot/sec cm ²
* from internal sources	8.2×10^{14}	phot/sec cm ²
* TOTAL	$J = 1.5 \times 10^{15}$	phot/sec cm ²
* BLIP $D_{\lambda_c}^*$	4.7×10^{11}	cm $\sqrt{\text{Hz/W}}$
<hr/>		
* MINIMUM SCAN TIME FOR BLIP PERFORMANCE	min $t_d = 7.07 \times 10^{-3}$	sec
* CORRESPONDING BASELINE NESR.	$(\text{NESR})_0 = 5.5 \times 10^{-7}$	W/cm ² sr cm ⁻¹
* MINIMUM DETECTABLE QUANTITY D (see figure)	min D = $0.3 - 1.0 \times 10^{13}{}^{\dagger}$	(molec/cm ²) (W/cm ² sr cm ⁻¹)
* UNCERTAINTY IN D	$\sigma_{D'} = 1.4 \times 10^{12}$	(molec/cm ²) (W/cm ² sr cm ⁻¹)

[†]The larger value (1×10^{13}) is the MDQ.

Figure 1.2 $P(T|T)$, $P(T|0)$ Nomograph for SO_2 ν_1 Band



view (on the scale of the figure, the spectral radiance added by SO_2 would be barely discernible, since the minimum detectable quantity is very small). The middle part of the figure shows the spectral transmittance of the atmosphere. FASCOD1 was used to obtain the radiance and transmittance spectra and also to degrade them to a spectral resolution of 0.1 cm^{-1} ($\sin v/v$ Full Width at Half Maximum). The lowest part of the figure shows the "normalized spectral contrast" of the $\text{SO}_2 \nu_1$ band. This quantity is $\alpha_{gv} \tau_v$ normalized to its maximum value; i.e., it is ideally the normalized contrast spectral radiance (Eq. 2) and the normalized correlation reference spectrum.

Table 1.3 (the second page of the standard output) gives various parameters of the detection band, system performance parameters, and the resulting minimum detectable quantity corresponding to approximately 95 percent detection probability and approximately one percent false detection probability. Quantities preceded by an asterisk would change if any of the system radiometric parameters were changed. The spectral resolution should really be considered a constant since $\Delta v = 0.1 \text{ cm}^{-1}$ is close to an optimal value. However, for some of the target species α_{gv} had to be determined from measurements corresponding to lower resolution ($\Delta v > 0.1$). In the standard-format outputs, the MDQ is always based on a scan time equal to "min t_d "; again, this convention was adopted only to facilitate scaling of the MDQ results. Table 1.3 gives the value 1×10^{13} for the MDQ of $\text{SO}_2 (\nu_1)$.

It should be noted that the photon fluxes listed in the summary tables (e.g., Table 1.3) do not include the contribution from the fourth interferometer port. The fourth port approximately doubles the listed photon fluxes, which means that the BLIP $D_{\lambda_c}^*$ should be divided by $\sqrt{2}$, and the $(\text{NESR})_0$ s multiplied by $\sqrt{2}$. The effect of the fourth port is included,

however, in the listed MDQ's and uncertainties in D . In other words, the tables really apply to the case where background subtraction is performed in the data processing (three-port interferometer) rather than optically (four-port interferometer). The post-detection subtraction effectively increases the $\overline{\text{NESR}}$ by $\sqrt{2}$; hence, both techniques yield the same MDQ and uncertainty. The fourth port would be used primarily to reduce dynamic range.

Figure 1.2 displays, for the SO_2 ν_1 band, the tradeoff available between detection and false detection probabilities for various threshold levels on the spectral correlation coefficient. The figure shows that the threshold value R corresponding to the MDQ given in Table 1.3 is approximately 0.07. Note that the figure has two abscissa scales. One is used according to the amount D of target gas present. The other gives the corresponding "correlation signal-to-noise" Z , defined as $\sigma' D / \sqrt{2} \overline{\text{NESR}}$, where σ' is the standard deviation of the reference spectrum $\tau_{\nu} \alpha_{\nu}$. According to Eq. (2), Z is the standard deviation of the observed contrast spectral radiance ΔN_{ν} divided by the effective rms system noise. In this example, Z is approximately 0.12 at the MDQ level. This means that the observed ΔN_{ν} would look more like noise than the characteristic $\tau_{\nu} \alpha_{\nu}$ spectral signature of the SO_2 ν_1 band.

It is worth noting that Z , at the MDQ level, is always between approximately 0.1 and 0.3 for all of the candidate detection bands (see Vol. II). This implies that it is generally not possible to determine the temperature of the target gas by examination of the distribution of rotational line strengths in the ΔN_{ν} spectrum (unless $D \gg \text{MDQ}$). Thus, it is not possible to determine the "minimum" target gas column thickness u independently of

$\Delta B(T_g, T_s)$ solely by the FTS spectral measurements. However, it is possible, for many of the detection bands, to determine the background temperature T_s from one of the two measurements used to calculate ΔN_v , provided the baseline configuration is used in the three-port rather than (or in addition to) the four-port mode.

The fact that the target gases can be detected and quantified using spectral measurements of rather low signal-to-noise justifies the use of a spectral correlation process that involves but one threshold parameter. In other words, the use of a multidimensional decision space corresponding to a Bayes test (likelihood ratios) on the spectral elements would not be expected to yield a very large increase in detectability, since the expected large noise tends to make the decision region a hypersphere. The selected correlation process could, perhaps, be made more nearly optimum by the simple procedure of excluding the minority negative or positive spectral contrast radiances ΔN_v (it is assumed that phase correlation would be used in the recovery of FTS spectra).

It is pointed out in Section 5 that spectral elements containing strong atmospheric absorptions must be excluded to ensure that atmospheric/background spatial variations do not represent overwhelming interferences. The fact that spectral information can be manipulated, in the computer, on an element-by-element basis makes the proposed technique far superior to the well-known analog method of gas-cell correlation.

The performance figures given in the standard outputs and in the following summary tables may contain small errors resulting from a bug in the pre-release FASCOD1 that was not discovered until most of the computations were completed. The FASCOD1 error was in the definition of function F3, which

is one of the four line shape functions used to synthesize the Voigt line shape (cf. Clough and Kneizys⁴). This error can have a significant effect only for very strong lines and/or large optical depths, and, hence, in the present application is important only when the target species is overlapped by very strong atmospheric lines (as in the case of the SO_2 ν_1 band, shown in Fig. 1.1). Re-evaluation of some of the computed results indicated that the $\overline{\text{NESR}}$'s, MDQ's and computed uncertainties in D contain errors which are generally less than a few percent.

1.1 Minimum Detectable Quantities

The following tables summarize the performance capabilities of the selected baseline configuration under "standard" and "ideal" conditions. The tables list minimum detectable quantities, and also the corresponding $\overline{\text{NESR}}$ s. The MDQ's scale directly as the system $\overline{\text{NESR}}$ s, and the required dynamic range is inversely proportional to $\overline{\text{NESR}}$ under conditions of BLIP performance. The complete scaling relations for $\overline{\text{NESR}}$ and dynamic range are provided in Section 1.4. The effects of non-standard conditions (climatic scene variations) are summarized in Section 1.2. The effects of non-ideal conditions (atmospheric/background interferences in the background-subtraction process) are reported in Section 1.3.

Table 1.4 lists all of the candidate detection bands considered in this study, the computed values for $\min t_d$, and the corresponding $(\overline{\text{NESR}})_0$ s, MDQ's and uncertainties in the minimum detectable quantities. Note that the HCl and DF bands have been divided arbitrarily into sub-bands of width 100 or 200 cm^{-1} , since it was anticipated that detection bands of width greater than 200 cm^{-1} would correspond to unrealistically large dynamic range in the interferogram.

Table 1.4 Summary of Detection Performance for Candidate Bands

Molecule	Detection Band (cm^{-1})	$\min t_d$ (sec)	$(\text{NESR})_0$ ($\text{W}/\text{cm}^2\text{-sr-cm}^{-1}$)	MDQ (molec/cm^2) ($\text{W}/\text{cm}^2\text{-sr-cm}^{-1}$)	Uncertainty in θ	
					θ_0 (molec/cm^2) ($\text{W}/\text{cm}^2\text{-sr-cm}^{-1}$)	(molec/cm^2) ($\text{W}/\text{cm}^2\text{-sr-cm}^{-1}$)
HF	3240-3440	5.52	1.2×10^{-9}	9.0×10^{13}		2.1×10^{13}
CH_4 (ν_3) (ν_4)	3000-3025	7.79	6.0×10^{-10}	8.0×10^{10}		1.6×10^{10}
	1295-1310	2.85×10^{-2}	7.4×10^{-8}	4.0×10^{13}		8.7×10^{12}
NO_2 ($\nu_1 + \nu_3$) (ν_2)	2850-2935	2.84	2.7×10^{-9}	2.5×10^{10}		4.3×10^9
	710-795	5.13×10^{-3}	5.9×10^{-7}	1.75×10^{13}		4.0×10^{12}
H_2O ($2\nu_1$) (ν_3) (ν_1)	2525-2590	1.63	5.4×10^{-9}	1.4×10^{11}		1.9×10^{10}
	2160-2210	0.978	9.9×10^{-9}	1.0×10^{11}		1.4×10^{10}
	1250-1320	1.27×10^{-2}	2.5×10^{-7}	1.0×10^{13}		2.1×10^{12}
HCl	2500-2700	1.02	1.1×10^{-8}	9.0×10^{11}		2.3×10^{11}
	2700-2900	1.53	6.6×10^{-9}	1.25×10^{10}		3.1×10^9
	2900-3000	3.09	2.4×10^{-9}	4.5×10^9		1.1×10^9
DF	2500-2700	1.02	1.1×10^{-8}	2.3×10^{11}		5.6×10^{10}
	2700-2900	1.53	6.6×10^{-9}	9.0×10^9		2.2×10^9
	2900-3000	3.09	2.4×10^{-9}	2.3×10^{10}		5.8×10^9
HBr	2450-2650	0.930	1.3×10^{-8}	8.0×10^{10}		1.9×10^{10}
SO_2 ($\nu_1 + \nu_3$) (ν_1)	2450-2525	1.32	7.2×10^{-9}	2.5×10^{11}		3.8×10^{10}
	1090-1210	7.07×10^{-3}	5.5×10^{-7}	1.0×10^{13}		1.4×10^{12}
CO_2	2375-2400	2.24	3.1×10^{-9}	2.5×10^{11}		5.7×10^{10}
CO ($1-0$)	2130-2185	0.833	1.2×10^{-8}	8.5×10^{10}		1.8×10^{10}
HI	2100-2200	0.629	1.9×10^{-8}	3.5×10^{13}		8.9×10^{12}
NH_3 (ν_2)	915-970	7.46×10^{-3}	4.1×10^{-7}	7.3×10^{11}		1.7×10^{11}
HNO_3 ($2\nu_9$)	887.5-902.5	1.82×10^{-2}	1.4×10^{-7}	8.0×10^{11}		1.8×10^{11}
$\text{C}_2\text{H}_2\text{O}_2$	880-1000	6.54×10^{-4}	2.5×10^{-7}	7.0×10^{12}		5.1×10^{11}
CH_3	790-990	3.63×10^{-3}	1.2×10^{-6}	3.5×10^{13}		6.0×10^{12}

Table 1.5 gives corresponding system performance figures scaled to an interferometer scan time of 10 seconds. In the BLIP region, system $\overline{\text{NESR}}$ scales simply as $[\min t_d(\text{sec})/10]^{1/2}$ which is the quantity listed as "Scaling Factor". The fifth column in Table 1.5 is the minimum detectable column thickness u , in molec/cm², corresponding to a temperature difference of 1°C between the target gas and an ideal black background. Since column thickness (or gas density or mass flow rate) is assumed to be of greater interest than the detectable quantity D , we used the former minimum quantity to select the "best" detection bands. The relationship between $\text{MIN } u(\Delta T = 1^\circ\text{C})$ and MDQ is, of course, strongly dependent on the spectral location of the detection band (the derivative of the Planck function with respect to temperature). The underscored MIN u values in column 5 indicate the preferred detection bands.

Table 1.6 lists the preferred detection bands for the 15 different target species, the MIN u 's, and also the corresponding minimum detectable volume concentrations of the target species (in parts per million volume) for a gas-cloud thickness of 10 meters and a 5°C difference in target-background temperature. Note that the CO₂ blue spike detection band is a special case, corresponding to detection on the basis of an assumed large temperature difference rather than excess column thickness (see Section 2.4). Note, also, that two candidate detection bands for NO₂ are included in this summary table. The reason is that the preferred NO₂ band requires that the system include a detection capability extending to approximately 14.1 μm; if lower performance can be tolerated for NO₂, the longwave system cutoff would be 12.7 μm, which might dictate a different choice of detector for the longwave detection bands.

Table 1.5 Performance Scaled to 10-Second Dwell Time for Candidate Bands

Molecule	Detection Band (cm^{-1})	WESR	Scaling Factor	Minimum Detectable Column Thickness u (molec/cm^2) for $\Delta T = 1^\circ\text{C}$	Uncertainty (molec/cm^2)
HF	3240-3440	8.6×10^{-10}	0.743	2.6×10^{23}	6.0×10^{22}
$\text{CH}_4(\nu_2)$ (ν_4)	3000-3025	5.3×10^{-10}	0.882	8.5×10^{19}	1.7×10^{19}
	1295-1310	3.9×10^{-9}	5.34×10^{-2}	2.0×10^{19}	4.4×10^{18}
$\text{NO}_2(\nu_1 + \nu_3)$ (ν_2)	2850-2935	1.44×10^{-9}	0.533	1.1×10^{19}	1.9×10^{18}
	710-795	1.3×10^{-8}	2.26×10^{-2}	2.3×10^{18}	5.2×10^{17}
$\text{N}_2\text{O}(2\nu_1)$ (ν_2) (ν_1)	2525-2590	2.2×10^{-9}	0.404	1.5×10^{19}	2.0×10^{18}
	2160-2210	3.1×10^{-9}	0.313	2.6×10^{18}	3.6×10^{17}
	1250-1320	8.9×10^{-9}	3.56×10^{-2}	3.2×10^{18}	6.8×10^{17}
HCl	2500-2700	3.51×10^{-9}	0.319	8.8×10^{19}	2.3×10^{19}
	2700-2900	2.35×10^{-9}	0.391	2.9×10^{18}	7.2×10^{17}
	2900-3000	1.33×10^{-9}	0.556	2.5×10^{18}	6.1×10^{17}
DF	2500-2700	3.51×10^{-9}	0.319	2.3×10^{19}	5.5×10^{18}
	2700-2900	2.58×10^{-9}	0.391	2.1×10^{18}	5.2×10^{17}
	2900-3000	1.33×10^{-9}	0.556	1.3×10^{19}	3.2×10^{18}
HBr	2450-2650	3.9×10^{-9}	0.305	6.2×10^{18}	1.5×10^{18}
	2450-2525	2.6×10^{-9}	0.363	1.9×10^{19}	2.9×10^{18}
$\text{SO}_2(\nu_1 + \nu_3)$ (ν_1)	1090-1210	1.5×10^{-8}	2.66×10^{-2}	2.0×10^{18}	2.8×10^{17}
	2375-2400	1.5×10^{-9}	0.474	(NA)	(NA)
CO_2	2130-2184	3.6×10^{-9}	0.289	1.9×10^{18}	3.9×10^{17}
$\text{CO}(1-0)$	2100-2200	4.8×10^{-9}	0.251	6.5×10^{20}	1.6×10^{20}
NH	915-970	1.12×10^{-8}	0.0273	1.2×10^{17}	2.8×10^{16}
NH_3	887.5-902.5	5.99×10^{-9}	0.0427	2.0×10^{17}	4.5×10^{16}
HNO_3	880-1000	2.0×10^{-9}	8.09×10^{-3}	2.4×10^{17}	2.5×10^{17}
$\text{C}_2\text{H}_4\text{O}_2$	790-990	2.35×10^{-8}	0.0191	2.9×10^{18}	6.7×10^{17}

Table 1.6 Scaled Performance for "Best" Bands

Molecule	Detection Band (cm^{-1})	* MIN u (molec/ cm^2) for $\Delta T = 1^\circ\text{C}$	** MIN v (ppmV)
HF	3240-3440	2.6×10^{23}	2.1×10^6
HCl	2900-3000	2.5×10^{18}	20
$\text{NO}_2(\nu_1 + \nu_3)$	2850-2935	1.1×10^{19}	92
DF	2700-2900	2.1×10^{18}	17
HBr	2450-2650	6.2×10^{18}	51
CO_2	2375-2400	(NA)	*** 0.047
$\text{N}_2\text{O}(\nu_3)$	2160-2210	2.6×10^{18}	22
$\text{CO}(1-0)$	2130-2185	1.9×10^{18}	16
HI	2100-2200	6.5×10^{20}	5310
<hr/>			
$\text{CH}_4(\nu_4)$	1295-1310	2.0×10^{19}	163
$\text{SO}_2(\nu_1)$	1090-1210	2.0×10^{18}	16
$\text{NH}_3(\nu_2)$	915-970	1.8×10^{17}	1.0
$\text{HNO}_3(2 \nu_9)$	887.5-902.5	2.0×10^{17}	1.6
$\text{C}_2\text{H}_4\text{O}_2$	880-1000	3.4×10^{17}	2.8
CH_3I	790-990	3.9×10^{18}	32
$\text{NO}_2(\nu_2)$	710-795	2.3×10^{18}	19

SEE following page for footnotes.

Table 1.6 (Continued)

*For baseline system, except dwell time $t_d = 10$ secs.

** $t_d = 10$ secs., cloud thickness = 10 m, $\Delta T = 5^\circ\text{C}$, $T_{\text{sfc}} = 300\text{K}$

$$\begin{aligned} \text{MIN } v &= \frac{\text{MIN } u \text{ (molec/cm}^2\text{) for } \Delta T = 1^\circ\text{C}}{0.269 \times 10^2 \left(\frac{273}{300}\right) \frac{\text{molec}}{\text{cm}^3} \times L \text{ (1000 cm)} \times \Delta T (5^\circ\text{C})} \times 10^6 \\ &= \text{MIN } u \times 8.17 \times 10^{-18} \end{aligned}$$

***For $t_d = 10$ secs., cloud thickness = 10 m, and $\Delta T = 550^\circ\text{C}$ ($T_{\text{gas}} = 850\text{K}$, $T_{\text{sfc}} = 300\text{K}$):

$$\begin{aligned} \text{MIN } v &= \frac{\text{MIN } u \text{ (molec/cm}^2\text{) for } \Delta T = 550^\circ\text{C and } v = 2400 \text{ cm}^{-1}}{0.269 \times 10^2 \left(\frac{273}{850}\right) \times 1000} \times 10^6 \\ &= \frac{(\text{MIN } D \text{ for } t_d = 10 \text{ secs}) / [B(850) - B(300) \text{ at } 2400 \text{ cm}^{-1}]}{0.269 \times 10^{20} \left(\frac{273}{850}\right) \times 1000} \times 10^6 \\ &= \frac{\left(\frac{2.24}{10}\right)^{1/2} 2.5 \times 10^{11} / (2.89 \times 10^{-4})}{0.269 \times 10^{20} \left(\frac{273}{850}\right) \times 1000} \times 10^6 \\ &= 0.047 \text{ ppmV} \end{aligned}$$

The minimum quantities given for NO_2 in any of these tables may be somewhat pessimistic because of the model used for the vertical distribution of "normal" atmospheric NO_2 . The atmospheric vertical column thickness for NO_2 was approximately 1.7 times greater than we had intended it to be as the result of a keypunch error (see footnote below Table 2.1). However, the variability and/or uncertainty in atmospheric NO_2 concentrations is probably on the order of a factor of two.⁶

The MDQ and MIN u for HNO_3 are somewhat pessimistic because the detection band includes the $2\nu_5$ transition, but not the nearby ν_5 transition (which was not in AFGL trace gas line parameters compilation).

Table 1.7 is a grand summary of system requirements and detection capabilities for the 15 molecules of interest. The table segregates the selected shortwave bands (3-5 μm) and longwave bands (7.5-14 μm), and includes the dynamic range requirements of the system. The listed dynamic range values do not include the potentially large reduction that could be effected by the use of the fourth port (second input port) in the selected baseline configuration.

1.2 Effects of Uniform Scene Variations

The MDQ's will depend, obviously, on the atmospheric transmittance between the target and sensor, and also on the brightness of the scene, since the latter influences the received total photon flux and, hence, the system NESRs. For a few of the detection bands we recalculated the MDQ's using the LOWTRAN Midlatitude Winter model in place of the Midlatitude Summer, and for nadir viewing angles equal to zero and 45 degrees (see Section 4). Table 1.8 gives the lowest and highest recalculated MDQ's normalized to those for the standard case. The lowest correspond to

Table 1.7 Summary of Selected Detection Bands, and Performance for 10-Second Dwell Time

Molecule	Band (cm^{-1})	Bandwidth	$\lambda_1 (\mu\text{m})$	λ_2	$\min t_d (\text{sec})$	NESR (10 sec)	Dynamic Range (10 sec)	\dagger MIN v (ppmV)
^2HF	3240-3440	200	2.907-3.086		5.52	8.6×10^{-10}	1.51×10^4	2.1×10^6
HCl	2900-3000	100	3.333-3.448		3.09	1.3×10^{-9}	2.66×10^4	20
$\text{NO}_2(\nu_1+\nu_3)$	2850-2935	85	3.407-3.509		2.84	1.4×10^{-9}	2.89×10^4	92
DF	2700-2900	200	3.448-3.704		1.53	2.6×10^{-9}	5.45×10^4	17
HBr	2450-2650	200	3.774-4.082		0.930	3.9×10^{-9}	9.04×10^4	51
CO_2	2375-2400	25	4.167-4.211		2.24	1.5×10^{-9}	3.61×10^4	$\dagger 0.047$
$\text{N}_2\text{O}(\nu_3)$	2160-2210	50	4.525-4.630		0.978	3.1×10^{-9}	8.34×10^4	22
CO	2130-2185	55	4.577-4.695		0.833	3.6×10^{-9}	9.79×10^4	16
HI	2100-2200	100	4.546-4.762		0.629	4.8×10^{-9}	1.31×10^5	5310

$\text{CH}_4(\nu_4)$	1295-1310	15	7.634-7.722		2.9×10^{-2}	3.9×10^{-9}	2.49×10^5	163
$\text{SO}_2(\nu_1)$	1090-1210	120	8.265-9.174		7.1×10^{-3}	1.5×10^{-8}	1.05×10^6	16
$\text{NH}_3(\nu_2)$	915-970	55	10.309-10.929		7.5×10^{-3}	1.1×10^{-8}	9.71×10^5	1.0
$\text{HNO}_3(2\nu_9)$	887.5-902.5	15	11.080-11.268		1.8×10^{-2}	6.0×10^{-9}	5.42×10^5	1.6
$^{\text{***}}\text{C}_2\text{H}_4\text{O}_2$	880-1000	120	10.000-11.364		6.5×10^{-4}	2.0×10^{-9}	1.44×10^6	2.8
CH_3I	790-990	200	10.101-12.658		3.6×10^{-3}	2.4×10^{-8}	2.00×10^6	32
$\text{NO}_2(\nu_2)$	710-795	85	12.579-14.085		5.1×10^{-3}	1.3×10^{-8}	1.20×10^6	19

* not detectable

** 2.9 - 4.8 μm region uses InSb detectors with $\eta = 0.5$, $D^*f^* = 5 \times 10^{16} \text{ cm Hz}^{3/2}/\text{W}$
 7.5 - 12.7 μm region uses HgCdTe detectors with $\eta = 0.7$, $D^*f^* = 8 \times 10^{17} \text{ cm Hz}^{3/2}/\text{W}$

*** resolution $\Delta\nu$ is 0.8 cm^{-1} ; $\Delta\nu = 0.1$ for other bands.

\dagger for 10-sec scan time, cloud thickness = 10 m, and $\Delta T = 5^\circ\text{C}$ (except $\Delta T = 550^\circ\text{C}$ for CO_2)

Table 1.8 Variation of MDQ Between Midlatitude Winter, $\theta = 0$, and Midlatitude Summer, $\theta = 45^\circ$

<u>Molecule</u>	<u>Detection Band (cm^{-1})</u>	<u>MDQ Relative to Standard Case</u>	
		<u>(lowest)</u>	<u>(highest)</u>
HCl	(2900-3000)	0.73	1.53
$\text{NO}_2(\nu_1 + \nu_3)$	(2850-2935)	0.75	1.05
DF	(2700-2900)	0.75	1.06
HBr	(2450-2650)	0.74	1.05
$\text{CH}_4(\nu_4)$	(1295-1310)	0.39	2.80
$\text{SO}_2(\nu_1)$	(1090-1210)	0.53	1.26

Midlatitude Winter, a nadir angle of zero and a surface temperature of 273K. The highest correspond to Midlatitude Summer, nadir angle equal to 45 degrees and a surface temperature of 300K.

The MDQ variations are small except for the CH_4 and SO_2 bands. The variation for these two bands is due to the fact that they contain significant H_2O absorptions, and that approximately five times more water vapor is contained in the inclined summer path than the vertical winter path. Over the entire range of latitudes, seasons and zenith angles (0 to 45°), the H_2O path column thickness could vary by a factor of 15.

The MDQ's variations given in Table 1.8 do not incorporate any kind of geometrical viewing effects; i.e., the column thickness u in the definition of MDQ is measured along the line-of-sight.

1.3 Effects of Spatial Scene Variations

Section 5 deals with the effects of scene non-uniformity (incomplete background subtraction) and other possible types of interference in the detection process. A major interference is the presence of differing

atmospheric H_2O amounts in the two parts of the scene that are differenced, since this can result in very strong H_2O emission/absorption lines in the contrast radiance spectrum. In fact, we show in Section 5 that spectral resolution elements containing any strong atmospheric lines (especially H_2O lines) must be excluded in the spectral correlation processing in order to achieve useful MDQ levels. In other words, the effect is too large to be tolerated as an interference. The reduction in the number of useable spectral elements results, of course, in an increase in the MDQ.

We recalculated the MDQ's to reflect this modification of the correlation processing only for the selected SO_2 , HCl and HBr detection bands. The MDQ for SO_2 increased by the factor 1.5, and was essentially unchanged for the HCl and HBr bands. The selected SO_2 and HCl bands both contain strong H_2O lines, but there is less coincidence of H_2O and HCl lines than there is of H_2O and SO_2 lines, owing to the very different nature of these two bands.

The effects of spatial background temperature variations are also considered in Section 5, but only for the HBr detection band. It is shown that a difference of $10^\circ C$ in the subtracted backgrounds would lead to unacceptable performance, unless the corresponding Planck spectral radiance difference in the contrast spectrum can be removed. The implication is that the contrast radiance spectrum must be "prewhitened" before it is correlated with the reference spectrum.

1.4 The Scaling Nomographs

The performance of the baseline configuration can be scaled to other scan times t_d , instantaneous fields of view α , collector diameters D and f /numbers ($F^\#$), using the summary tables of Section 1.1 and Figs. 1.3 and 1.4. Figure 1.3 is a plot of "Relative NESR $\cdot\alpha D$ " versus "Relative t_d "; the

Figure 1.3 Scaling Nomograph for Band-Average Noise-Equivalent Spectral Radiance (NESR)

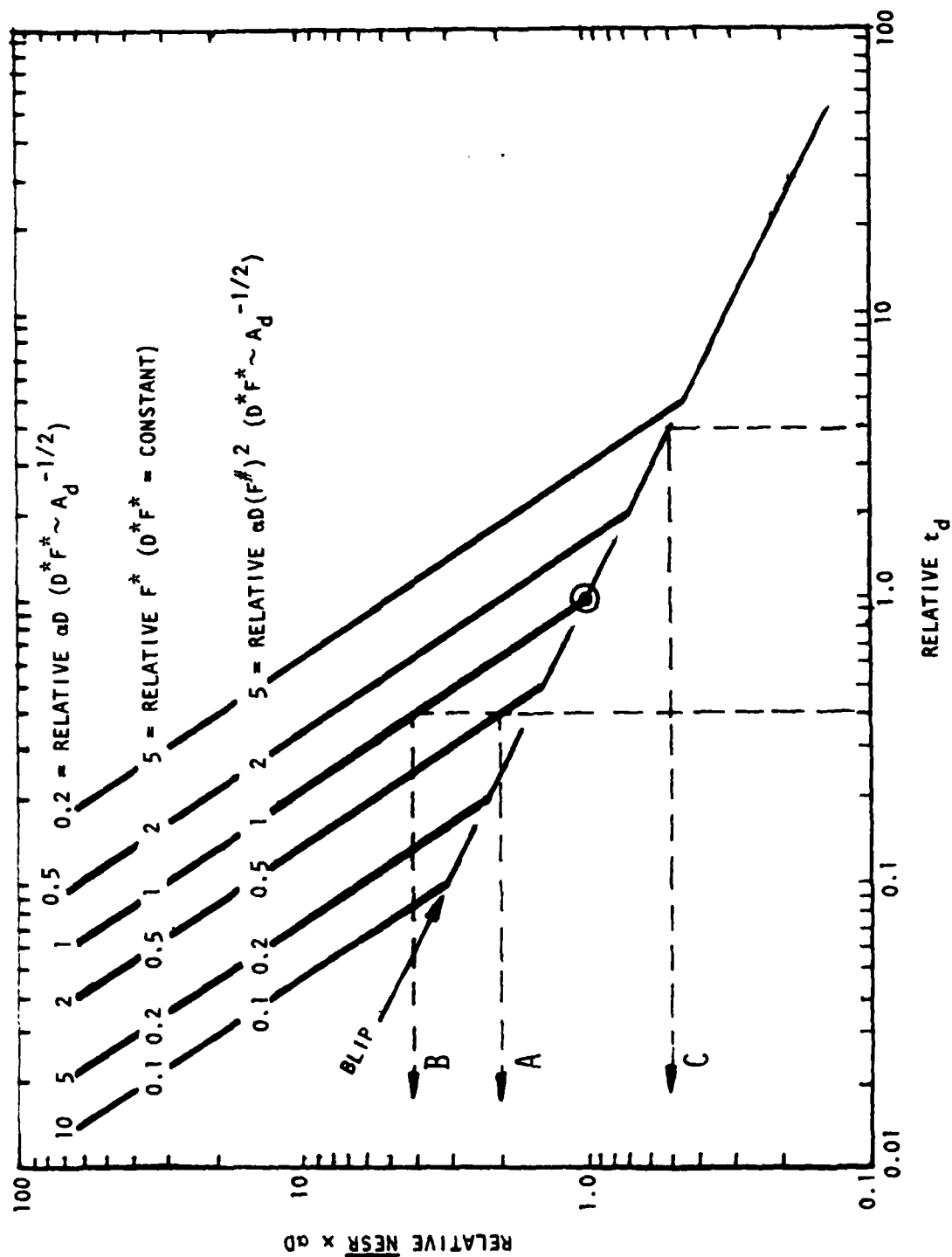
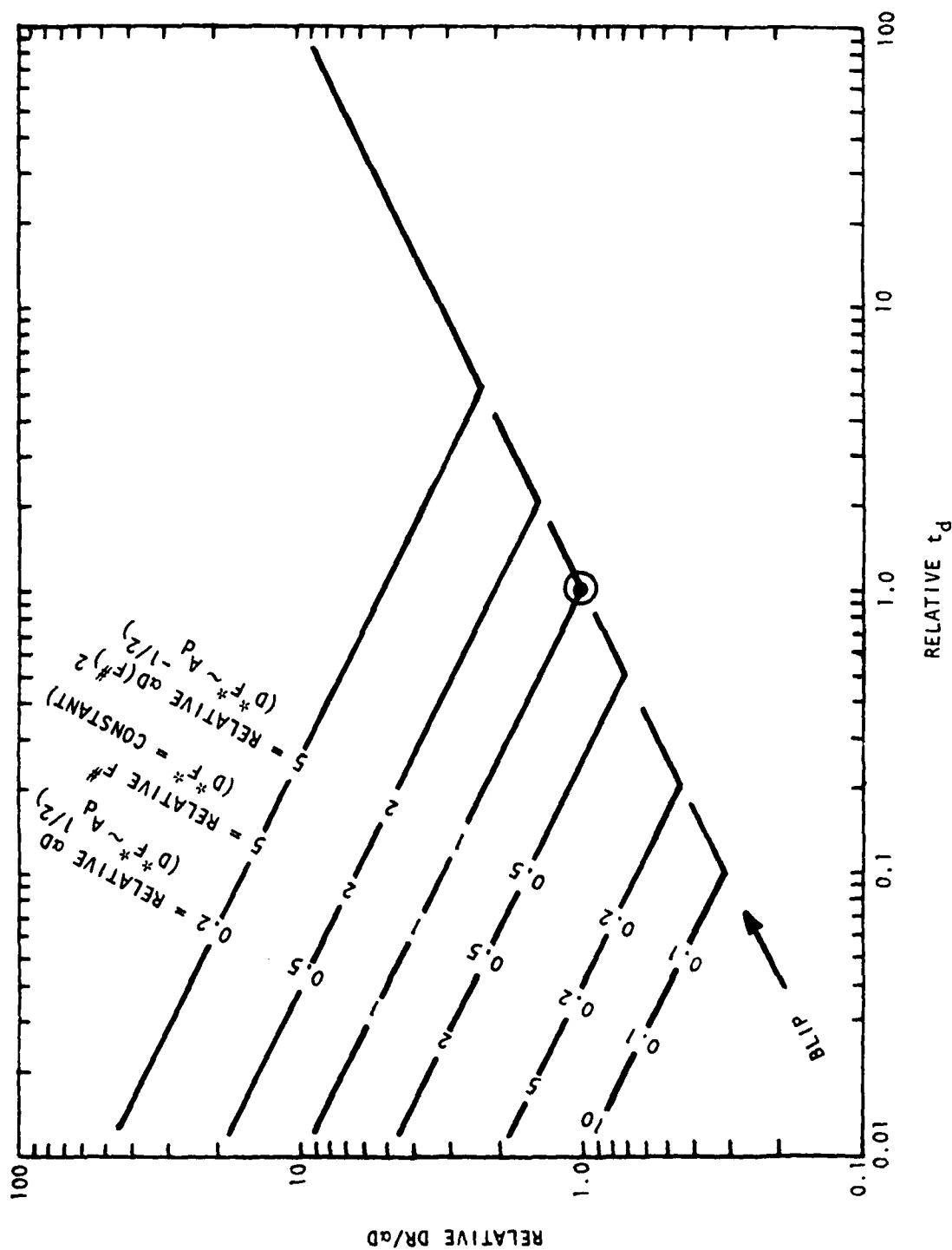


Figure 1.4 Scaling Nomograph for Detection Band Required Dynamic Range (DR)



point (1,1) represents the selected baseline configuration. This figure can be used to extrapolate the system \overline{NESR} . The detection band MDQ's and uncertainties in D scale directly as the \overline{NESR} . Figure 1.4 is a similar nomograph for scaling the system dynamic range DR.

The region of background limited performance is a single line in each of the figures. The use of the figures outside of the BLIP region (above the lines labeled "BLIP") depend on how the detector D^*F^* behaves with detector area A_d . For InSb detectors, $D^*F^* \sim A_d^{-1/2}$ while for Si:As detectors, $D^*F^* \sim A_d^{1/2}$. The nomographs can be used for these types of detectors and also for the case of D^*F^* independent of detector area. There appears to be no simple formula relating D^*F^* and A_d for HgCdTe. Hence, the nomographs should be used with caution for the detection bands that use HgCdTe detectors, when "Relative t_d " is close to unity and/or large changes are made in α , D or $F^\#$. The following examples illustrate the use of the nomographs:

EXAMPLE A

The selected dwell time is made equal to 40 percent of min t_d and the product αD is doubled (e.g., α might be doubled while D is held fixed). The system has a detector whose D^*F^* scales as $\sqrt{A_d}$; hence, we use the curve labeled "Relative $\alpha D = 2$ for $D^*F^* \sim \sqrt{A_d}$ " in Fig. 1.3. The value read from the abscissa shows that $\overline{NESR} \times \alpha D$ is now a factor of two greater. But αD was doubled; hence, the \overline{NESR} is unchanged. System performance is not in the BLIP range; also, it is unaffected by changes in system $F^\#$ for this type of detector.

Suppose the selected dwell time is, again, 40 percent of min t_d , and αD is unchanged. Suppose the system has a detector with constant D^*F^*

(independent of A_d). If we change the $F^\#$ to half the baseline value, the system $\overline{NESR} \times \alpha D$ doubles, (we use the curve labeled "Relative $F^* = 0.5$ for $D^*F^* = \text{CONSTANT}$ ") and, hence, the \overline{NESR} doubles. The curve we use for this type of detector is not dependent on changes in αD . However, if αD were doubled, then the \overline{NESR} would not change (since $\overline{NESR} \times \alpha D$ was doubled).

EXAMPLE B

Had we only changed the dwell time to $0.40 \times \text{min } t_d$ and not αD for the system whose D^*F^* varies as $\sqrt{A_d}$, the \overline{NESR} would increase by a factor of approximately four. Similarly, had we only changed the dwell time and not $F^\#$ or αD for the system whose D^*F^* is constant, the \overline{NESR} would also increase by a factor of four.

EXAMPLE C

Dwell time is increased to four times $\text{min } t_d$, αD is halved, and the detector D^*F^* varies as $\sqrt{A_d}$. The figure shows we are still in the BLIP range and that $\overline{NESR} \times \alpha D$ is half its original value; hence, \overline{NESR} is unchanged. Note that if αD were not changed, we would use the same curve, and \overline{NESR} would decrease to half its original value. Note, also, that if dwell time were increased four-fold and αD were decreased to 0.2 times its original value, we would be just outside the BLIP range; this would also happen if the detector D^*F^* were constant and $F^\#$ were increased to five times its original value.

The nomograph is used similarly for detectors whose D^*F^* varies as $A_d^{-1/2}$ (such as InSb), except that the choice of curve in the non-BLIP region depends on the relative value of $\alpha D(F^\#)^2$. The dynamic range nomograph is used in the same fashion as the \overline{NESR} nomograph.

SECTION 2

THEORETICAL BASIS

2.1 Notation

a, b, c	types of interferences
A	area of collecting aperture
A_c	projected area of gas cloud
A_d	area of detector
A_I	footprint area of sensor IFOV
$B_v(T)$	Planck's function for spectral radiance corresponding to temperature T
B_v^g	Planck's function for temperature T^g
$B(T_g)$	Planck's function for temperature T^g
$B(T^g)$	Planck's function for temperature T^g
$\overline{\Delta B}_v$	spectral average of the difference $B_v(T_g) - B_v(T_s)$
$\overline{\Delta B}_v(T_g, T_s)$	spectral average of the difference $B_v(T_g) - B_v(T_s)$
BLIP	background-limited performance
BPR	band photon radiance (photons/cm ² sr s)
c	speed of light
c_2	$= hc/k$: second radiation constant
D	diameter of collecting aperture, ALSO detectable quantity $Fu\overline{\Delta B}_v(T_g, T_s)$ of target gas
D_1, D_2, \dots	detectable quantities of other (spectrally interfering) target gases
D^*	band detectivity of detector
D_λ^*	spectral detectivity
$D_{\lambda_c}^*$	peak spectral detectivity
BLIP D^*	background-limited detector D^*
DR	dynamic range in the interferogram

f	focal length
Δf	system noise bandwidth
F	frequency in the interferogram, ALSO fraction of IFOV occupied by target gas
F^*	maximum frequency for BLIP performance (defined by detector D^*F^*)
$F^\#$	f/number
FTS	Fourier transform spectrometer
G	G-factor for detector
h	Planck's constant
$H(R)$	probability distribution function
IFOV	instantaneous field of view (single detector)
J	photon flux density on detector
J_E	photon flux density from external sources
J_I	photon flux density from internal sources
M	number of spectral resolution elements in detection band
MDQ	minimum detectable quantity (minimum D)
MIN v	minimum detectable volume concentration (ppmV) for $t_d =$ 10 secs, cloud thickness = 10 m, $T_g - T_s = 5^\circ\text{C}$ and $T_s = 300^\circ\text{K}$
n	detector noise in the contrast radiance spectrum
n_v	detector noise in contrast radiance spectrum and/or spectral radiance interferences in scene
N_v	spectral radiance of scene
ΔN	spectral radiance difference between two IFOV's
ΔN_v	spectral radiance difference between two IFOV's
N_1	spectral radiance in IFOV1
N_2	spectral radiance in IFOV2
N_1^a	atmospheric spectral emission in IFOV1

N_2^a	atmospheric spectral emission in IF0V2
N_1^s	surface radiance in IF0V1
N_2^s or N^s	surface radiance in IF0V2
N_v^s	spectral radiance of background surface
NEP	system noise equivalent power
NER	system noise equivalent radiance
NESR	noise equivalent spectral radiance
$\overline{\text{NESR}}$	average noise equivalent spectral radiance over detection band
p	probability density
$P(T T)$	detection probability
$P(T 0)$	false detection probability
R	threshold level on absolute value of normalized correlation coefficient ρ
t_d	dwelt time (interferometer scan time)
$\min t_d$	minimum t_d for BLIP performance
T	temperature
T_g	temperature of target gas
T^g	temperature of target gas
T_s	background (surface) temperature
T_{opt}	optics temperature
u	column thickness of target gas along the line-of-sight
x	$= c_2 v / (cT)$
x_i	unit normal random variate
z or Z	detection signal to noise
α	angular dimension of IF0V, ALSO spectral absorption coefficient of a target gas
α_{gv}	spectral absorption coefficient of a target gas

$\alpha_1, \alpha_2, \dots$	spectral absorption coefficients of other target gases that overlap α
α'	estimate of α or α_{gv}
β	$\alpha + (D/D_1)\alpha_1 + (D/D_2)\alpha_2 + \dots$ or $(D/D_1)\alpha_1 + (D/D_2)\alpha_2 + \dots$
$\tilde{\epsilon}$	effective emissivity of the optics toward the detector
η	quantum efficiency of the detector
λ	wavelength
λ_c	$= c/\nu_1$: longwave cutoff of the detector
μ	mean of ΔN_ν
μ'	mean of $\tau'\alpha'$ or $\tau_\nu\alpha_{gv}$
μ_ξ	mean of ξ/D
ν	wavenumber (c/λ)
$\Delta\nu$	resolved spectral interval or "resolution"
ν_c	c/λ_c
ν_1, ν_2	detection spectral band defined by cold filter
ξ	$= N_2$ ("no gas") - N_1 : difference in spectral radiance between two IFOV's when no target gas is present in either IFOV
$\bar{\xi}$	system efficiency
ξ_e	system efficiency due to non-optical effects
ρ	normalized coefficient of spectral correlation
$\tilde{\rho}$	value of ρ when there are interferences a and/or b and/or c but no system noise
σ'	standard deviation of the spectrum $\tau_\nu\alpha_{gv} \equiv \tau\alpha$
σ_0	standard deviation of the spectrum $\tau_\nu\alpha_{gv} \equiv \tau\alpha$
σ_1	standard deviation of $\tau'\alpha'$
σ_ξ	standard deviation of ξ/D
σ_{01}	covariance of $\tau\beta$ and $\tau'\alpha'$

$\sigma_{0\xi}$	covariance of τ_B and ξ/D
$\sigma_{1\xi}$	covariance of τ'_α and ξ/D
τ	optics transmission, ALSO atmospheric spectral transmittance
τ_v	atmospheric spectral transmittance
τ'_v	estimate of atmospheric spectral transmittance
τ'	estimate of atmospheric spectral transmittance
τ_1	atmospheric spectral transmittance in IFOV1
τ_2	atmospheric spectral transmittance in IFOV2
τ_v^*	transmittance computed in second run of FASCOD1
τ^g	spectral transmittance of target gas slab
τ_v^g	spectral transmittance of target gas slab
ω_d	cosine weighted solid angle of the system f-cone at the detector
Ω	solid angle of the IFOV

2.2 The Observable Quantity

It is assumed initially that all detectors (IFOV's) observe identical atmospheric layers and background surfaces, i.e., identical spectral radiances, when no target gases are present. The observed spectral radiance is equal to the atmospheric spectral emission plus a background contribution

$$\tau_v N_v^s, \quad (1)$$

where τ_v is the atmospheric spectral transmittance and N_v^s is the intrinsic spectral radiance of the background surface.

A slab of target gas of spectral transmittance τ_v^g has a spectral emissivity of $1-\tau_v^g$ and an intrinsic spectral radiance equal to $(1-\tau_v^g) B_v^g$, where $B_v^g \equiv B_v(T_g)$ is the Planck spectral radiance corresponding to the

temperature T_g of the gas. We will assume the target slab, lying just above the surface, is very thin; i.e., that the atmospheric transmittance between the top of the slab and the sensor is the same as the transmittance τ_v of the entire atmosphere. Then, the spectral radiance observed in an IFOV containing the target gas is equal to the atmospheric spectral emission plus

$$\tau_v(1-\tau_v^g) B_v^g + \tau_v \tau_v^g N_v^s . \quad (2)$$

The target gas adds to the observed emission via the first term and attenuates the background emission via the second term. It can be assumed that the observed atmospheric emission is not affected by the presence of a very thin target slab.

The spectral radiance difference, or contrast, between an IFOV containing the target and one not containing the target is the difference between expressions (2) and (1):

$$\begin{aligned} \Delta N_v &= \tau_v(1-\tau_v^g) B_v^g - \tau_v(1-\tau_v^g) N_v^s \\ &= \tau_v(1-\tau_v^g) (B_v^g - N_v^s) \end{aligned} \quad (3)$$

We will assume the target gases are present in very small amounts. That is, the slab is optically thin, which implies

$$\tau_v^g \approx 1 - u \alpha_{gv} , \quad (4)$$

where u is the column thickness of the gas along the line-of-sight and α_{gv} is its spectral absorption coefficient. Then the contrast spectral radiance, from Eqs. (3) and (4), is

$$\Delta N_v = \tau_v \alpha_{gv} u \cdot (B_v^g - N_v^s) , \quad (5)$$

We will make the additional assumption that the background has no sharp spectral structure (emits like a blackbody of temperature T_s), and that the detection spectral bands are narrow (100 cm^{-1} or less). Then, the Planck radiance difference in Eq. (5) can be approximated by its spectral average $\overline{\Delta B}_v$ over the detection band. If we allow for the occurrence of a target that does not fill the IFOV (occupies a fraction F of the IFOV), the observed contrast spectral radiance is

$$\begin{aligned} \Delta N_v &= \tau_v \alpha_{gv} D , \\ D &= F u \overline{\Delta B}_v(T_g, T_s) . \end{aligned} \quad (6)$$

D is defined as the observable or detectable quantity, since it can be determined approximately from the measurable spectra whose difference is ΔN_v , and a prediction of $\tau_v \alpha_{gv}$. It has the units of column thickness times spectral radiance; e.g., $(\text{molecules/cm}^2)(\text{W/cm}^2 \text{ sr cm}^{-1})$. The major purpose of this study was to determine the minimum detectable quantities (minimum D values or MDQ's) of specified target molecules when the measured ΔN_v includes a noise signal representative of a large-aperture, state-of-the-art FTS satellite system. In principle, the high-resolution spectral measurements allow an independent determination of the gas and surface temperatures; e.g., from the distribution of target rotational line intensities in ΔN_v and from the envelopes of the radiance spectra obtained for the two IFOV's. However, by using the correlation method described in Section 2.2, it is possible to detect target quantities that correspond to signal-to-noise levels much less than unity. In other words, the measured contrast spectrum

looks very much like noise at the MDQ level and, hence, it cannot be used to determine line intensities. On the other hand, the effective surface temperature can be obtained easily from the measured spectra for one or more detection bands. The implication is that T_g must be estimated by some other means if the quantity F_u rather than D is required; similarly, an independent estimate of F would be required to determine u .

The fraction F is the projected area of the target cloud A_c in the IFOV divided by the known IFOV "footprint" A_I . Thus,

$$\begin{aligned} A_I D &= A_c u \overline{\Delta B}_v \\ &= (\text{number of target molecules in IFOV}) \cdot \overline{\Delta B}_v. \end{aligned} \quad (7)$$

In other words, for a given Planck radiance difference (or given temperatures T_g, T_s) the spectral measurements yield the number of target molecules in the IFOV.

Most of Section 2 deals with "the ideal case", which assumes

- a.) the atmospheric spectral transmittance τ_v and target gas spectral absorption coefficient α_{gv} can be predicted exactly,
- b.) the absorptions of different target species do not overlap in the observed spectrum, and
- c.) the atmospheres and backgrounds in the two IFOV's are identical.

That is, system noise is assumed to be the only source of interference.

Some of the above assumptions are relaxed in Section 5.

2.3 Method of Detection and Quantification

The measured spectral data is intended to provide information on two levels:

- a.) Does the data imply sufficiently high estimated probability of the presence of a target, and is there sufficiently low

probability that noise or background signals will be falsely identified as a target?

b.) If the above conditions are true, what quantity D of target is present?

Sections 2.3.1 and 2.3.2 address the first question; the second is treated in Section 2.3.3.

2.3.1 Statistics of Detection/False Detection

One must first prescribe an operation on the spectral data that will enable recognition of the target. Generally, this operation will produce a value(s) to be compared to a predetermined threshold(s). If the threshold is exceeded, the presence of a target is declared. The fraction of the time this decision is correct is the detection probability $P(T|T)$. The fraction of the time a target is declared when, in fact, there is not a target present is the false detection probability $P(T|0)$.

Generally, by decreasing the detection threshold, detection probability can be gained at the price of increased false detection probability. Therefore, in selecting the threshold, the benefits of high confidence in the target event must be balanced against the risks accruing from false identification. A benign external scene and low system noise imply that high detection probability can be achieved together with low false detection probability.

When system noise and/or external interferences are included, the measured spectral radiance contrast between an IFOV containing the target and one not containing the target is

$$\Delta N_v = D \tau_v \alpha_{gv} + n_v . \quad (8)$$

D , τ_v and α_{gv} were defined above; n_v is a spectrally varying quantity that can represent detector noise and/or the effects of different atmospheric or background properties in the two IFOV's. A near-optimal process for target detection is based on the spectral correlation between ΔN_v and a prediction of $\tau_v \alpha_{gv}$. Specifically, we propose to use (threshold on) the magnitude of the normalized correlation coefficient

$$\rho = \frac{\langle (\Delta N_v - \mu) (\tau_v \alpha_{gv} - \mu') \rangle}{\left[\langle (\Delta N_v - \mu)^2 \rangle \langle (\tau_v \alpha_{gv} - \mu')^2 \rangle \right]^{1/2}} \quad (9)$$

where $\langle \rangle$ denotes a spectral sum or average over resolved spectral elements, μ is the mean of ΔN_v and μ' is the mean of $\tau_v \alpha_{gv}$, which is a theoretical estimate of the actual transmission-absorption coefficient product $\tau_v \alpha_{gv}$. Note that if $n_v = 0$ in Eq. (8) and $\tau_v \alpha_{gv} = \tau_v \alpha_{gv}$, then $\rho = \pm 1$. Negative ρ corresponds to negative D ; i.e., the target spectrum is observed in absorption because the target gas is cooler than the surface. When ρ and D are positive the target is observed in emission. Perfect detection corresponds to $|\rho| = 1$. In general, $|\rho|$ is less than unity when detector noise is present, and/or the background/atmosphere has different spectral radiances in the two IFOV's.

It is necessary to compute the probability distribution function of $|\rho|$ in order to determine the ability of the system to detect the target quantity D and reject false target signals. The distribution function, $H(R)$, is the probability or fraction of the time that $|\rho|$ exceeds the value R . If D is not zero, this is the same as the detection probability corresponding to the particular threshold level R and specified value of D . If D is zero, $H(R)$ is the false detection probability.

A reasonably complete determination of the probability distribution function of $|\rho|$ would require a detailed statistical description of the spatial and spectral properties of the background/atmospheric radiances, including spatial and spectral covariances. This information, however, is not readily available. Our only recourse in determining the effect on ρ of different background/atmospheric spectral radiances in the two IFOV's is to evaluate Eqs. (8) and (9) for a variety of different severe cases or a single "worst" case. Computations of this type are described in Section 5. The statistics of ρ are, of course, also determined by the detector noise in ΔN_v .

We will treat in this section the case in which the only source of error in the measured spectral radiance contrast ΔN_v is detector noise. Then the n_v 's for the resolved spectral elements can be regarded as independent random normal variates with zero mean and standard deviation $\sqrt{2} \overline{NESR}$, where \overline{NESR} is the average noise equivalent spectral radiance over the cold-filtered spectral band. The factor $\sqrt{2}$ results from the fact that ΔN_v is the difference of two measurements with independent noise contributions. We will also assume $\tau_v \alpha'_{gv} = \tau_v \alpha_{gv}$; i.e., that the atmospheric transmittance and target gas absorption coefficient are both known exactly.

It is shown in Appendix A that under the stated conditions (see Eqs. (A-3) and (A-13)),

$$\rho = \frac{1 + \frac{1}{DM(\sigma')^2} \sum^M n_v (\tau_v \alpha_{gv} - \mu')}{\left[1 + \frac{2}{DM(\sigma')^2} \sum^M n_v (\tau_v \alpha_{gv} - \mu') + \frac{1}{(D\sigma')^2} \sum n_v^2 \right]^{1/2}}$$

$$\rho = \frac{1 + \frac{1}{MZ} \sum_{i=1}^M x_i}{\left[\frac{1}{M} \sum_{i=1}^M \left(1 + \frac{1}{Z} x_i \right)^2 \right]^{1/2}} \quad (D \neq 0) \quad (10)$$

where σ' = the standard deviation of the reference spectrum $\tau_{\nu} \alpha_{g\nu}$

M = the number of spectral elements in the summations

x_i = a unit normal random variate

$Z = \sigma' D / (\sqrt{2} \text{ NESR})$ = the ratio of rms signal to rms noise in the contrast radiance spectrum (i.e., the "detection signal-to-noise")

If D is zero

$$\rho = \frac{1}{M^{1/2}} \frac{\sum_{i=1}^M x_i}{\left[\sum_{i=1}^M x_i^2 \right]^{1/2}} \quad (D = 0) \quad (11)$$

Thus, ρ is a random variate dependent on M random noise samples n_{ν} or M values selected at random from a unit normal population.

It is to be noted that according to the second form of Eq. (10) and Eq. (11), the statistics of ρ will not depend on the detailed shape of the spectrum $\tau_{\nu} \alpha_{g\nu}$, but only on the rms variation σ' of the spectrum samples. This is illustrated also by the first form of Eq. (10) when it is noticed that the spectrum samples $\tau_{\nu} \alpha_{g\nu}$ can be interchanged in any manner (since the noise samples are mutually independent and uncorrelated with the $\tau_{\nu} \alpha_{g\nu}$ samples) without affecting the value of ρ . Thus, for example, one could reorder the $\tau_{\nu} \alpha_{g\nu}$ samples according to decreasing amplitude and thereby convert what might originally be a very structured spectrum into a relatively smooth one. The reordered sample set would, of course, have the

same standard deviation as the original set, and, therefore, would yield the same value for ρ .

2.3.2 Evaluation of the Detection Probability $P(T|T)$ and False Detection Probability $P(T|0)$

It would be difficult to determine analytically the probability distribution functions of the variates given by Eqs. (10) and (11) (the $P(T|T)$ and $P(T|0)$, respectively). One might expect that closed form expressions could be obtained, at least for the corresponding probability densities, were it not for the fact that the M unit normal variates in the numerators are the same as those in the denominators; i.e., the numerator cannot be regarded as independent of the denominator unless M is very large.* We elected to evaluate $P(T|T)$ and $P(T|0)$ by repeated computations of Eqs. (10) and (11) using pseudo-random numbers generated on the computer.

Specifically, we first assigned a value to M , generated M random numbers having a unit normal distribution, and computed ρ (Eq. 10) and ρ (Eq. 11). In the case of ρ (Eq. 10) it is necessary to perform the calculation for various values of Z . This process was repeated 5,000 times. We then determined the fractions of the 5,000 ρ (Eq. 10) values that exceeded the threshold values $R = 0.1, 0.15, 0.20, \dots, 1.0$. These fractions represent $P(T|T)$ vs. R and Z for given M . Similarly, the ρ (Eq. 11) values were used to obtain $P(T|0)$ vs. R for given M . The entire procedure was performed for several values of M . The results were plotted in the form $P(T|T)$ vs. $P(T|0)$.

* If the numerator and denominator of Eq. (11) could be assumed independent, ρ (for $D=0$) would obey the t-distribution, which approaches a normal distribution for large M .

Figures 2.1, 2.2 and 2.3 represent a sample of the computed results. The three figures correspond to signal-to-noise values $Z = 0.5, 1.0$ and 1.5 , respectively, and show $P(T|T)$ vs. $P(T|0)$ for fixed M and/or R . Figure 2.2 for example, shows that a contrast radiance spectrum with 20 resolved spectral elements and unit signal-to-noise Z , yields $P(T|T) = 93$ percent and $P(T|0) = 1$ percent if the threshold on $|\rho|$ is 0.55. Alternately, if 93 percent and 1 percent are the required detection and false detection probabilities, and the molecule of interest is observable in 20 resolution elements, we would be required to

- a.) Set the threshold on $|\rho|$ at 0.55
- b.) Achieve $Z = 1.0$, or accept a detection capability D corresponding to $Z = \sigma^{-1}D/(\sqrt{2} \text{ NESR}) = 1.0$.

If σ is the given standard deviation of the 20 spectral elements of $\tau_v \alpha_{gv}$, and NESR denotes the achievable noise equivalent spectral radiance of a given system configuration, then the minimum detectable quantity MDQ is

$$\begin{aligned} \text{MDQ} \equiv D_{\min} &= \frac{\sqrt{2} \text{ NESR } Z}{\sigma} \\ &= \frac{\sqrt{2} \text{ NESR}}{\sigma} \quad (\text{in this example}) \end{aligned}$$

The three figures illustrate the expected trends:

- a.) Detection performance and false threat rejection capability both increase with Z and M .
- b.) For fixed M and Z , detection and false detection probabilities both decrease with increasing threshold R .

What is surprising, perhaps, is the very strong dependence of system performance on Z .

Figure 2.1 $P(T|T)$ versus $P(T|0)$ for $Z = 0.5$

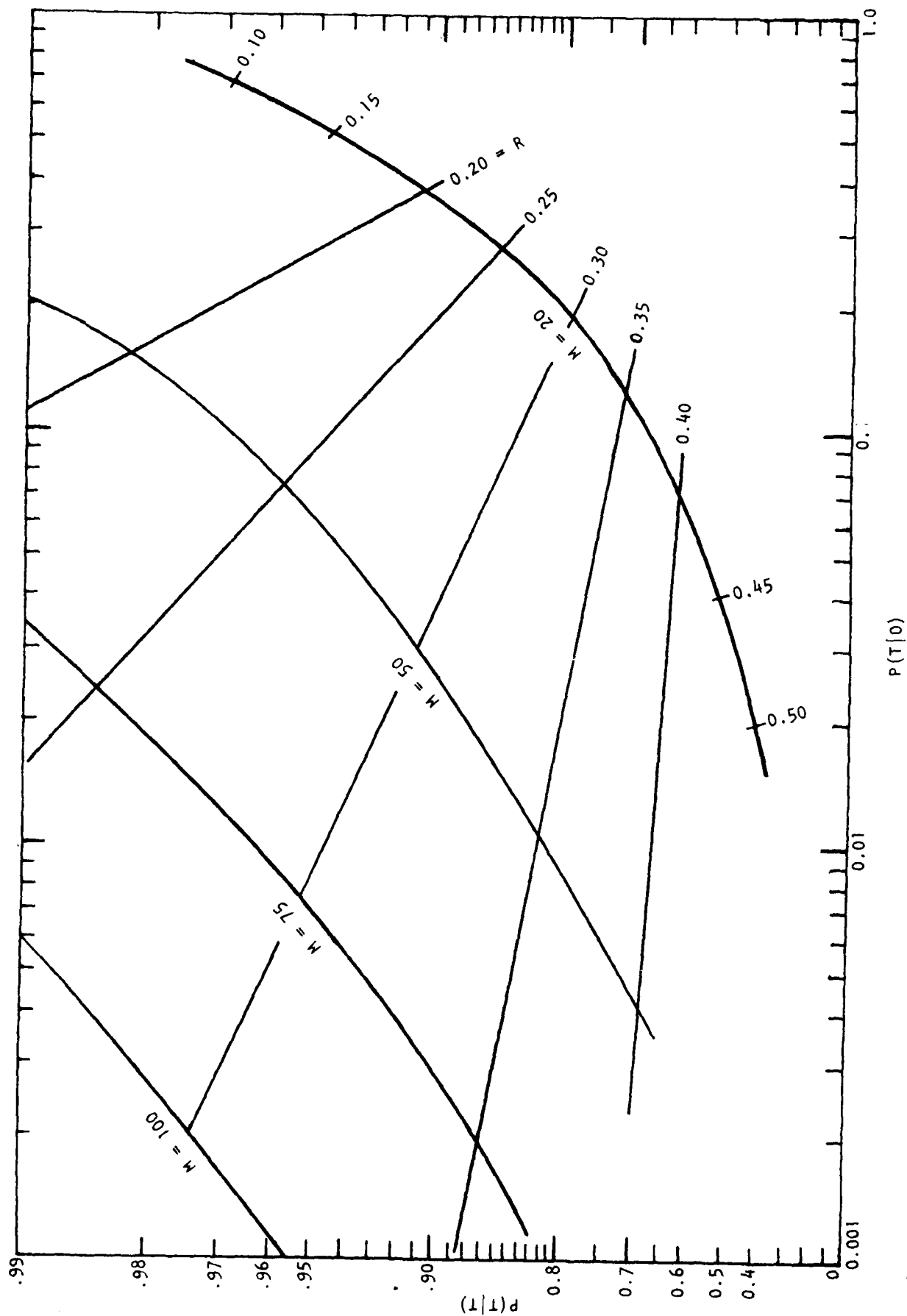


Figure 2.2 $P(T|T)$ versus $P(T|0)$ for $Z = 1.0$

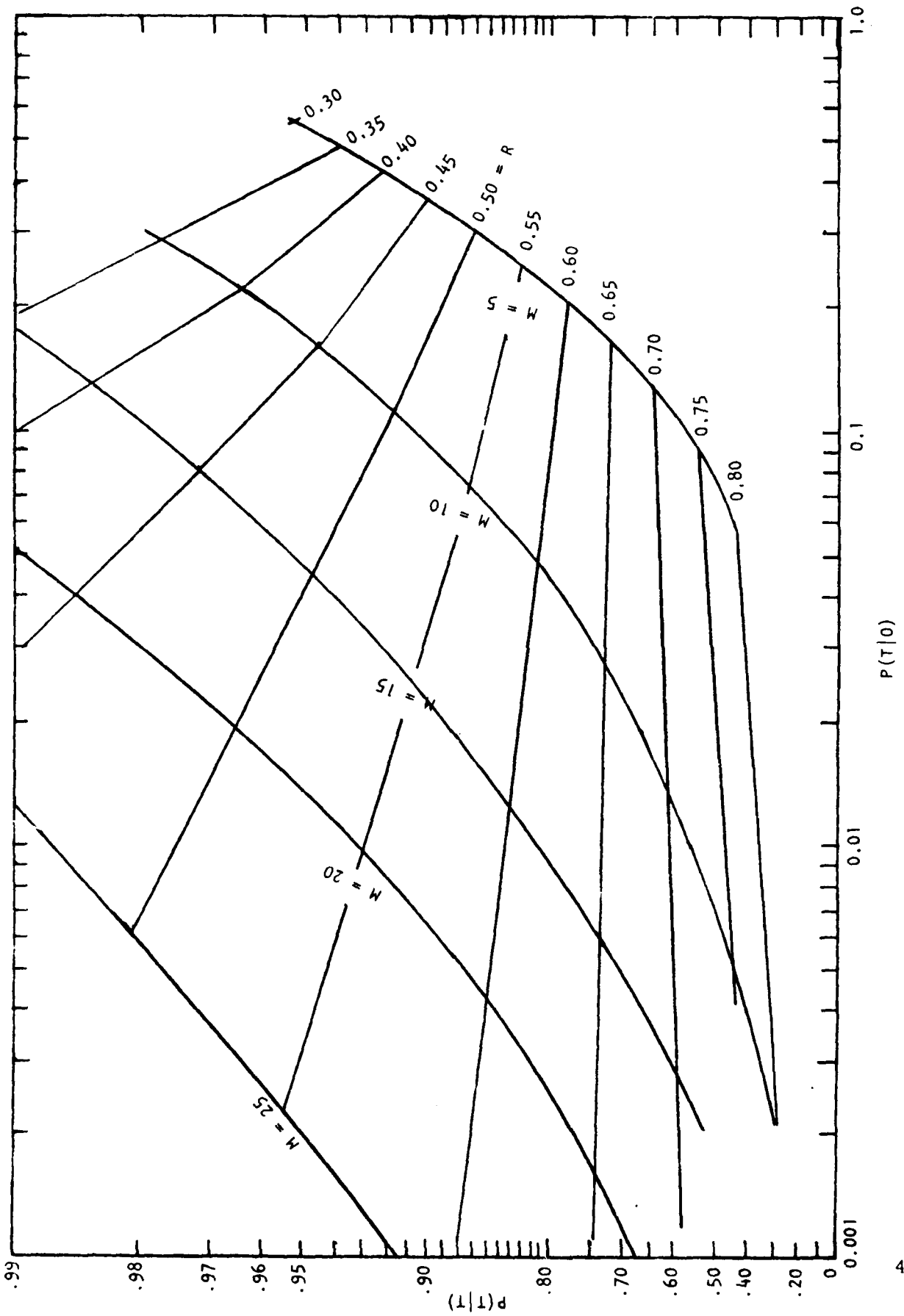
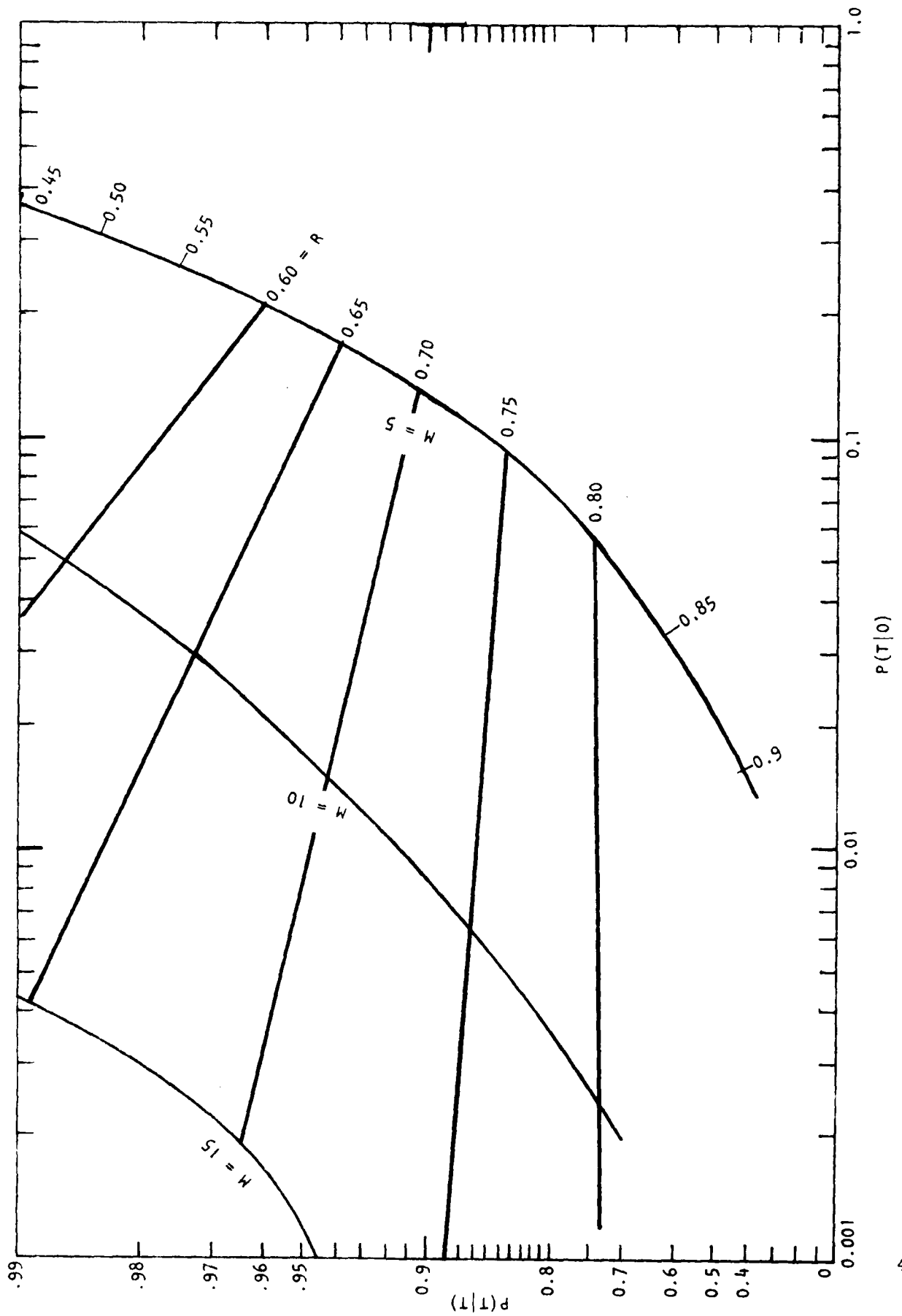


Figure 2.3 $P(T|T)$ versus $P(T|0)$ for $Z = 1.5$



Generally, optimal detection performance and false threat rejection capability will be realized by making the spectral resolution $\Delta\nu$ comparable to the width of any distinguishing spectral features in $\tau_{\nu} \alpha_{g\nu}$; e.g., to the line halfwidth if the spectrum has resolvable line structure (then $\Delta\nu$ should be approximately 0.1 cm^{-1}). That is, Z would be expected to have a maximum near this value of $\Delta\nu$ because of the way σ' and $\overline{\text{NESR}}$ vary with $\Delta\nu$. Note that as $\Delta\nu$ is made smaller, σ' will increase asymptotically to a constant value, while $\overline{\text{NESR}} = \text{NER}/\Delta\nu$ will continue to increase; hence, Z will decrease. If $\Delta\nu$ is much larger than the width of spectral features, then generally σ' will decrease more rapidly with $\Delta\nu$ than $\overline{\text{NESR}}$, and Z will, again, decrease. Once the spectral resolution is fixed we have very little control over the values of σ' and M (if there are two or more IR bands of a given species, we would, of course, choose the one with the largest σ' and/or M). Thus, in using Figs. 2.1-2.3, we would normally regard σ' and M as fixed. If the system performance requirements $P(T|T)$ and $P(T|0)$ are specified, and the $\overline{\text{NESR}}$ has been calculated, the figures would be used to determine the minimum detectable quantity, as in the above example. If the MDQ so determined is large compared to D values expected for typical targets, the implication is that the system must be redesigned; e.g., given a larger collecting aperture to achieve a smaller $\overline{\text{NESR}}$ and proportionately smaller MDQ.

Volume 11 contains plots of $P(T|T)$ vs. Z for different values of $P(T|0)$ and R , for each of the candidate detection bands (given σ' and M). The abscissa also have D -scales which were calculated from the band σ' 's and $\overline{\text{NESR}}$'s. Plots in this form are more convenient than the format of Figs. 2.1-2.3 for scaling the MDQ of the baseline sensor with respect to $\overline{\text{NESR}}$ (or

system parameters other than Δv). Like Figs. 2.1-2.3, they may also be used to trade between $P(T|T)$ and $P(T|0)$.

2.3.3 Estimation of Detectable Quantity D

The measured spectral radiance contrast is ideally

$$\Delta N_v = D \tau_v \alpha_{gv} \quad (12)$$

in the absence of noise. An optimal method of estimating D from the spectrum ΔN_v is to find the value D' that minimizes the mean squared spectral difference

$$\zeta = \sum_v \left(\Delta N_v - D' \tau_v \alpha'_{gv} \right)^2 \quad (13)$$

where the summation is over the M resolved spectral elements and $\tau_v \alpha'_{gv}$ is again a theoretical estimate of $\tau_v \alpha_{gv}$. Taking the derivative of ζ with respect to our estimate D' , setting the result to zero, and solving for D' we obtain

$$D' = \frac{\sum_v \tau_v \alpha'_{gv} \Delta N_v}{\sum_v \left(\tau_v \alpha'_{gv} \right)^2} \quad (14)$$

With detector noise n_v included, the spectral radiance contrast is

$$\Delta N_v = D \tau_v \alpha_{gv} + n_v \quad (15)$$

and our estimate of D becomes

$$D' = \frac{\sum_v \tau_v \alpha'_{gv} (D \tau_v \alpha_{gv} + n_v)}{\sum_v \left(\tau_v \alpha'_{gv} \right)^2} \quad (16)$$

If we assume τ_v and α_{gv} are accurately known ($\tau_v \alpha_{gv} = \tau_v \alpha_{gv}$), then

$$D' = D + \frac{\sum \tau_v \alpha_{gv} n_v}{\sum (\tau_v \alpha_{gv})^2} \quad (17)$$

This estimate is merely the true D plus a weighted sum of independent normal variates with zero mean and standard deviation $\sqrt{2 \text{ NESR}}$. Using the well-known theorem defining the statistics of a sum of normal variates (see Appendix A), we find that the uncertainty (standard deviation) of our estimate of D is

$$\sigma_{D'} = \frac{\sqrt{2 \text{ NESR}}}{\left[\sum (\tau_v \alpha_{gv})^2 \right]^{1/2}} \quad (18)$$

This can also be written

$$\sigma_{D'} = \sqrt{\frac{2}{M}} \frac{\text{NESR}}{\left[(\sigma')^2 + (\mu')^2 \right]^{1/2}}$$

where μ' and σ' are the mean and standard deviation of $\tau_v \alpha_{gv}$. The relative uncertainty is

$$\frac{\sigma_{D'}}{D} = \frac{1}{2M^{1/2}} \frac{\sigma'}{\left[(\sigma')^2 + (\mu')^2 \right]^{1/2}} \quad (19)$$

2.4 Computation of Normalized Contrast Spectrum $\tau_v \alpha_{gv}$

As shown above, the ability to detect and quantify the target gases depends, to a large extent, on the mean and variance of $\tau_v \alpha_{gv}$, which will be called the normalized contrast spectrum (since ΔN_v equals $D \tau_v \alpha_{gv}$ in the

absence of noise and other interferences), or the "reference spectrum", since it may also represent a predicted spectrum with which the actual ΔN_{ν} is correlated. The target gases represented by the spectral absorption coefficients $\alpha_{g\nu}$ are of two different types in this study:

- a.) Those included in the AFGL atmospheric and trace gas line parameters compilations.
- b.) Other molecules, not in the AFGL compilations, for which the Aerospace Corporation was able to provide ARC with either theoretical calculations of $\alpha_{g\nu}$ or spectral measurements of this quantity (at one-atmosphere pressure and temperatures near 300°K).

The "AFGL molecules" are the normal constituents of the atmosphere and several trace molecules present at all levels and/or near the surface in uncertain amounts. The first step in computing $\tau_{\nu}\alpha_{g\nu}$ consisted of setting up a model atmosphere for the AFGL molecules (see Section 2.4.1). The vertical distributions of temperature, pressure and the AFGL molecules with well-established vertical distributions were represented by the AFGL (LOWTRAN) Midlatitude Summer model atmosphere. The distributions of some molecules included in the AFGL line parameters compilations, but not in the LOWTRAN model atmospheres (such as NO_2 and HNO_3), were based on information collected by the Department of Transportation (FAA) during the HAPP Program.⁶ AFGL molecules not included in the HAPP data or LOWTRAN model (SO_2 and NH_3), and the "Aerospace molecules", were assumed to exist in small amounts only near ground level, as localized clouds.

For all of the AFGL target molecules, $\tau_{\nu}\alpha_{g\nu}$ was computed on the basis of two runs of a pre-release version of AFGL's FASCOD1 computer code. The first run obtained the spectral transmittance τ_{ν} and the spectral radiance

of a vertical path through the adopted atmospheric model. The second run obtained the spectral transmittance (τ_v^*) under the same conditions except that the target gas density in the bottom-most layer (0 to 10 meters) was increased by a nominal ten percent. We then calculated the difference $\tau_v - \tau_v^*$ and divided by Δu :

$$\begin{aligned} \frac{\tau_v - \tau_v^*}{\Delta u} &\approx \frac{\tau_v - \tau_v \tau_v(\Delta u)}{\Delta u} = \frac{\tau_v [1 - \tau_v(\Delta u)]}{\Delta u} \\ &\approx \frac{\tau_v \alpha_{gv} \Delta u}{\Delta u} = \tau_v \alpha_{gv} \end{aligned} \quad (20)$$

where Δu denotes the excess target column density resulting from the 10 percent increase. The term $\tau_v(\Delta u)$ denotes the transmittance of the excess column density of the target gas in the 10-meter slab, which is always optically thin. Hence, the difference $\tau_v - \tau_v^*$ normalized by Δu reduces to $\tau_v \alpha_{gv}$, which is independent of the selected Δu and corresponds to an α_{gv} representing ground-level temperature and pressure.

We made no attempt to compute the target gas spectral absorption coefficients for elevated temperature except for the case of CO_2 in the $4.3 \mu\text{m}$ "blue-spike" region. Increasing the temperature would generally cause the lines to become narrower (since the Lorentz halfwidth varies as $T^{-1/2}$) which would tend to increase detection capability. It would also effect a redistribution of rotational line intensities. However, except for the case of molecular hot bands, these effects would be expected to have an unimportant influence on the MDQ. That is, the change in MDQ would usually be small compared to the increase in the quantity D available for detection caused by the large increase in $\overline{\Delta B}_v$. The MDQ need not be known accurately if it is much smaller than the available D .

In the case of CO_2 , we selected the detection band to coincide with the blue-spike region of the $4.3 \mu\text{m}$ band. Since the observable blue-spike radiation arises from a hot band transition, we assumed that detection would be based solely on a large temperature increase rather than an excess column thickness u and a small $\overline{\Delta B}_v$. Accordingly, the two FASCOD1 runs used the same CO_2 column thickness for the 0-10 meter layer, but different temperatures. We used Eq. (20) to obtain $\tau_v \alpha_{gv}$, but set Δu equal to the total CO_2 column thickness of the layer. The resultant α_{gv} is the CO_2 absorption coefficient at the elevated temperature (850°K) used in the second FASCOD1 run. In the definition of MDQ (Eq. 6), u then represents the column thickness of the CO_2 at elevated temperature.

In the case of molecules for which Aerospace provided data on α_{gv} , we made a single FASCOD1 run to obtain τ_v , and then simply computed the product $\tau_v \alpha_{gv}$ of the merged spectra. The $\tau_v \alpha_{gv}$ spectrum obtained by either method corresponds to a spectral resolution (Full Width at Half Maximum) of approximately 0.10 cm^{-1} and to a $\sin v/v$ instrument line shape. The effect of instrument line shape was introduced in the FASCOD1 computations via its subroutine SCANFN. The $\sin v/v$ function is one of the four standard options in SCANFN.

The ARC computer code CNTRST used to obtain $\tau_v \alpha_{gv}$ from the FASCOD1/Aerospace spectra also obtained the standard deviation and mean of $\tau_v \alpha_{gv}$. It also computed the net photon radiance (by integrating the photon radiance spectrum equivalent to the FASCOD1 radiance spectrum obtained with τ_v). The photon radiance and baseline system parameters determine the system $\overline{\text{NESR}}$ and dynamic range (Section 2.5). The standard deviation and mean of $\tau_v \alpha_{gv}$, the $\overline{\text{NESR}}$, and the $P(T|T)$, $P(T|0)$ nomographs described in

Section 2.3.2 determine the MDQ for each detection band and the uncertainty in detected MDQ.

2.4.1 The Atmospheric Model

The atmospheric model used in most of the computations of $\tau_v \alpha_{gv}$ and the band photon radiance is the LOWTRAN Midlatitude Summer model.⁴ This model, and the five others in the LOWTRAN codes, give vertical distributions of temperature, pressure, H₂O, CO₂, O₃, N₂O, CO, CH₄ and O₂. The vertical distributions used for NO, NO₂ and HNO₃ are listed in Table 2.1 which is based on measurement data reported by Luther⁶ (the reported data shows considerable variations between measurements from different sources; the values in Table 2.1 represent approximate mean distributions). The molecules SO₂ and NH₃ were assumed to be present only in the bottom 10-meter layer in the amount 1×10^{13} molec/cm². The AFGL code ATMPH was used to integrate the LOWTRAN Midlatitude Summer model (to find mean temperatures and pressures and the column densities of the species H₂O, CO₂, O₃, N₂O, CO, CH₄ and O₂ for the 15 layers indicated in Table 2.1).

2.5 Computation of the System $\overline{\text{NESR}}$ and Required Dynamic Range

This section gives the equations used to obtain the background-limited specific detectivities (BLIP D^* 's) of the system detectors and the corresponding system $\overline{\text{NESR}}$'s and dynamic range. It is emphasized that these results assume the detectors are operating at frequencies where BLIP performance is achievable. The variation of D^* and $\overline{\text{NESR}}$ with frequency outside of the BLIP range is discussed in Section 2.6.

For an ideal photoconductive BLIP detector, the spectral detectivity is linear with wavelength out to its longwave cutoff λ_c :

Table 2.1 Vertical Distributions used for NO, NO₂ and HNO₃

Layer Boundaries (km)	LAYER COLUMN THICKNESSES (molec/cm ²)		
	NO	NO ₂	HNO ₃
0-0.01	3.9×10^{12}	1.0×10^{13}	1.0×10^{12}
0.01-4.0	1.24×10^{15}	3.1×10^{15}	4.4×10^{14}
4-7	6.6×10^{14}	1.15×10^{15}	4.2×10^{14}
7-11	6.4×10^{14}	9.0×10^{14}	7.2×10^{14}
11-14	3.0×10^{14}	5.1×10^{14}	7.2×10^{14}
14-17	2.1×10^{14}	4.8×10^{14}	9.6×10^{14}
17-20	1.5×10^{14}	5.15×10^{14}	1.2×10^{15}
20-25	3.0×10^{14}	9.9×10^{14}	1.85×10^{15}
25-30	4.25×10^{14}	1.0×10^{15}	7.0×10^{14}
30-35	3.75×10^{14}	$7.5 \times 10^{15*}$	1.15×10^{14}
35-40	2.1×10^{14}	2.5×10^{14}	2.2×10^{13}
40-45	1.1×10^{14}	1.0×10^{14}	0
45-54	0	7.0×10^{13}	0
54-75	0	0	0
75-∞	0	0	0

*This value was used in the computations; it should have been 7.5×10^{14} .

$$D_{\lambda}^* = \frac{\lambda}{\lambda_c} D_{\lambda_c}^* = \frac{v_c}{v} D_{\lambda_c}^* , \quad (21)$$

where the peak spectral detectivity $D_{\lambda_c}^*$ is given by

$$D_{\lambda_c}^* = \frac{\eta^{1/2} \lambda_c}{2hcJ^{1/2}} = \frac{\eta^{1/2}}{2hv_c (J_E + J_I)^{1/2}} , \quad (22)$$

where η is the detector quantum efficiency, h is Planck's constant, c is the speed of light, and J is the total photon flux density incident on the detector. The contribution to J from sources external to the sensor is obtained from

$$\begin{aligned} J_E &= \frac{\Omega A \tau}{A_d} \int_{v_1}^{v_2} \frac{N_v}{hv} dv \\ &= \frac{\pi \tau}{(2F\#)^2} \int_{v_1}^{v_2} \frac{N_v}{hv} dv \end{aligned} \quad (23)$$

where Ω = solid angle IFOV of the system = α^2 , the angular IFOV.

A = collecting aperture area

τ = optics transmittance

A_d = detector area

$F\#$ = system f/number at detector

N_v = external radiance spectrum (computed using FASCOD1)

v_1, v_2 = spectral band limits defined by the cold filter ($v_2 \leq v_c$).

The second form of Eq. (23) is obtained from the first by substituting

$A = \pi D^2/4$, $A_d = f^2 \Omega$ and $F\# = f/D$, where f is the system effective focal length and D is the effective aperture diameter. (Throughout this report,

D , $F^\#$ and Ω or $\alpha = \sqrt{\Omega}$ are regarded as the fundamental geometric parameters of the system.)

The contribution to J from internal sources (optics emission within the cone shielded f/cone) is given by

$$J_I = \omega_d \tilde{\epsilon} \int_{\nu_1}^{\nu_2} 2 \frac{B_\nu(T)}{h\nu} d\nu$$

$$\simeq \frac{\pi \tilde{\epsilon}}{1 + (2F^\#)^2} \frac{2\pi T}{cc_2\nu^2} \sum_{m=1}^5 e^{-mx} \left[1 + \frac{2}{mx} \left(1 + \frac{1}{mx} \right) \right] \bigg|_{\nu_2}^{\nu_1} \quad (24)$$

where $\omega_d = \pi/[1 + (2F^\#)^2]$ is the cosine-weighted solid angle of the system f-cone at the detector, $\tilde{\epsilon}$ is the effective emissivity of the optics towards the detector, $B_\nu(T)$ is the Planck radiance spectrum, $T = 300^\circ\text{K}$, $x = c_2\nu/cT$ and $c_2 = hc/k$, the second radiation constant. The series in Eq. (24) (of which only the first five terms are used in this study) is the infinite series expansion of a finite integral of the Planck spectral photon emittance of a blackbody.⁷ The series converges most rapidly for large x (small λT), and five terms gives sufficient accuracy for wavelengths as long as $30 \mu\text{m}$ when $T = 300^\circ\text{K}$.

The system performance parameters, such as noise equivalent radiance, depend on an average or band D^* which is related to the peak spectral detectivity $D_{\lambda_c}^*$ through the so-called G factor:

$$D^*(\lambda_1 \text{ to } \lambda_2) = D^*(\nu_1 \text{ to } \nu_2) = G D_{\lambda_c}^* \quad (25)$$

where

$$\begin{aligned}
 G &= \frac{1}{\lambda_2} \int_{\lambda_1}^{\lambda_2} \lambda N_{\lambda} d\lambda \quad \bigg/ \quad \int_{\lambda_1}^{\lambda_2} N_{\lambda} d\lambda \\
 &= \nu_2 \int_{\nu_1}^{\nu_2} \frac{N_{\nu}}{\nu} d\nu \quad \bigg/ \quad \int_{\nu_1}^{\nu_2} N_{\nu} d\nu
 \end{aligned} \tag{26}$$

where N_{ν} is, again, the external radiance spectrum. This equation is analogous to expressions which relate blackbody and monochromatic detectivities.⁸

Note that the only system parameters on which $J = J_E + J_I$ depends are system f/number, optics τ and $\bar{\epsilon}$, and, of course, the two spectral band cutoffs. Consequently, $D_{\lambda_c}^*$, D_{λ}^* and $D^*(\nu_1 \text{ to } \nu_2)$ depend only on these system parameters and on the detector quantum efficiency; i.e., on $F^\#$, $\bar{\epsilon}$, τ , ν_1 , ν_2 and η .

The system noise equivalent radiance at the entrance aperture can be written in the alternate forms

$$\begin{aligned}
 \text{NER} &= \frac{(A_d \Delta f)^{1/2}}{\bar{\epsilon} A \Omega} \frac{1}{D^*(\nu_1 \text{ to } \nu_2)} \\
 &= \frac{F^\# (\Delta f)^{1/2}}{\bar{\epsilon} \frac{\pi}{4} D \Omega^{1/2}} \frac{1}{D^*(\nu_1 \text{ to } \nu_2)}
 \end{aligned} \tag{27}$$

where $\Delta f = \pi/(4t_d)$ is the noise bandwidth, t_d is the dwell time (interferometer scan time), and $\bar{\epsilon}$ is the net system efficiency, equal to $\tau \epsilon_e$, where ϵ_e is the efficiency due to non-optical effects (e.g., the signal modulation efficiency).

The *average* noise equivalent spectral radiance of a multiplexing spectrometer (e.g., an interferometer) is equal to

$$\overline{\text{NESR}} = \text{NER}/\Delta\nu, \quad (28)$$

where $\Delta\nu$ is the resolved spectral interval. The actual NESR is given by

$$\begin{aligned} \text{NESR} &= \frac{\bar{\nu}}{\nu} \overline{\text{NESR}} = \frac{2\nu}{\nu_1 + \nu_2} \overline{\text{NESR}} = \frac{2\nu}{\nu_1 + \nu_2} \frac{\text{NER}}{\Delta\nu} \\ &= \frac{F^\#(\Delta f)^{1/2}}{\xi \frac{\pi}{4} D\Omega^{1/2}} \frac{2\nu}{(\nu_1 + \nu_2)\Delta\nu} \frac{1}{D^*(\nu_1 \text{ to } \nu_2)} \end{aligned} \quad (29)$$

where $\bar{\nu}$ in the first form is $(\nu_1 + \nu_2)/2$. Equation (29) results from the fact that the spectral NER is inversely proportional to the spectral D^* which is inversely proportional to the wavenumber ν ; i.e., NESR is directly proportional to ν and its average over (ν_1, ν_2) must be equal to $\overline{\text{NESR}}$.

The required dynamic range in the interferogram defined in terms of NER and other quantities referred to the aperture is

$$\text{Dynamic Range (DR)} = \frac{1}{\text{NER}} \left[\int_{\nu_1}^{\nu_2} N_\nu d\nu + \frac{\tilde{\epsilon}}{\tau} \int_{\nu_1}^{\nu_2} B_\nu(T_{\text{opt}}) d\nu \right] \quad (30)$$

where the second term in brackets is the "signal" contribution of optics emission after extrapolation to the aperture. In terms of photon flux density at the detector, this can be written (using Eqs. 25, 26 and 22-24)

$$\text{DR} = \frac{1}{2} \frac{F^\# D\Omega^{1/2} n^{1/2} \xi_e J^{1/2}}{(\Delta f)^{1/2}}. \quad (31)$$

Note that the factor $J^{1/2}$ in Eq. (31) is approximately proportional to $1/F^\#$ (see Eqs. 23 and 24). The approximation assumes that the denominator factor $1 + (2F^\#)^2$ can be replaced by $(2F^\#)^2$ or that $J_E \gg J_r$. This means that the dynamic range is very nearly independent of f/number for a cold-shielded system with fixed Ω and D .

The equations given above were programmed for the computer to obtain, for the various detection bands, the peak spectral detectivity within the passband ($D_{\nu_1}^*$), the band detectivity $D^*(\nu_1 \text{ to } \nu_2)$, the average noise equivalent spectral radiance \overline{NESR} , and the system dynamic range. The computed values apply to the selected baseline system and are reported in Section I and Vol. II.

2.6 Basis of the Scaling Nomographs

The nomographs presented in Section 1.4 may be used to scale the \overline{NESR} (MDQ's) and required dynamic range of the selected baseline system with respect to its basic radiometric parameters, such as collector diameter, IFOV, and scan time. This section defines the construction of the two scaling nomographs.

According to Eqs. (27) and (28) of the previous section, \overline{NESR} is proportional to

$$\begin{aligned} \overline{NESR} &\sim \frac{F^\# (\Delta f)^{1/2}}{D \Omega^{1/2}} \frac{1}{D^*} \\ &\sim \frac{F^\#}{D \alpha t_d^{1/2}} \frac{1}{D^*}, \end{aligned} \quad (32)$$

if the system resolution ($\Delta \nu$) and efficiency $\bar{\epsilon}$ are fixed. But to a very good approximation

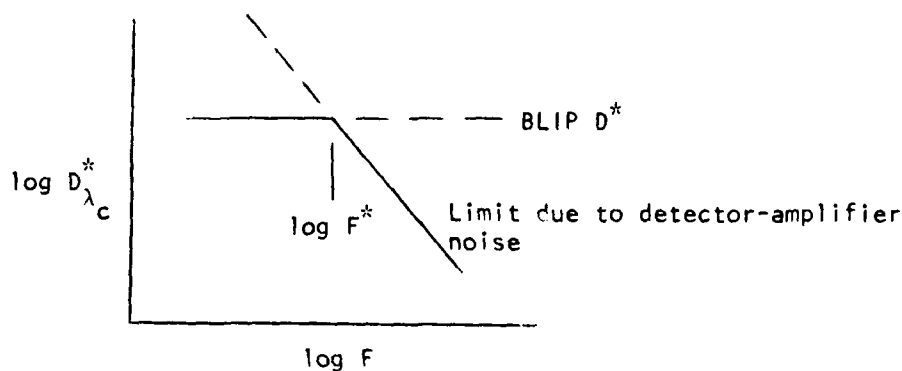
$$D_{\lambda_c}^* \sim F^\# \quad (33)$$

for a cold-shielded detector, if the detector is operating in the BLIP domain and $\tilde{\epsilon}$, τ , n , and T_{optics} are fixed (see Appendix B). Since $D^* \sim D_{\lambda_c}^*$, we have from Eqs. (32) and (33)

$$\overline{\text{NESR}} \sim \frac{1}{(\alpha D) t_d^{1/2}} \quad (34)$$

in the BLIP domain.

The sketch below shows schematically the variation of system $D_{\lambda_c}^*$ with electrical frequency F . For sufficiently low F the system will achieve BLIP performance, while, for higher frequencies ($F > F^*$), performance will be limited by detector-preamplifier noise.



The limit on $D_{\lambda_c}^*$ due to detector-amplifier noise will vary as

$$D_{\lambda_c}^* \sim \frac{\sqrt{A_d}}{F} = \frac{f_\alpha}{F} = \frac{F^\# D_\alpha}{F} \quad (35)$$

for some types of detector; e.g., an arsenic-doped silicon detector.² The D^* depends on detector area because this type of detector is more properly characterized by an area-independent NEP (noise-equivalent power) rather than a D^* .

The highest electrical frequency at which the detector must operate is the nominal number of interferogram samples $\nu_2/\Delta\nu$ divided by the scan time t_d :

$$F = \frac{\nu_2}{t_d \Delta\nu} \sim \frac{1}{t_d} . \quad (36)$$

Substituting (36) into (35) gives

$$D_{\lambda_c}^* \sim F^\# (\alpha D) t_d , \quad (37)$$

and substituting (37) into (32), with $D_{\lambda_c}^* \sim D^*$, gives

$$\overline{\text{NESR}} \sim \frac{1}{(\alpha D)^2 t_d^{3/2}} \quad (38a)$$

for the high-frequency (non-BLIP) domain. The equivalent relation for detectors with area-independent $D^* F^*$ (i.e., $D_{\lambda_c}^* \sim 1/F$) is

$$\overline{\text{NESR}} \sim \frac{F^\#}{(\alpha D) t_d^{3/2}} . \quad (38b)$$

For an InSb detector, whose $D^* F^*$ is proportional to $A_d^{-1/2}$, the equivalent relation is

$$\overline{\text{NESR}} \sim \frac{(F^\#)^2}{t_d^{3/2}} \quad (38c)$$

Equations (34) and (38a)-(38c) are the desired scaling relations for $\overline{\text{NESR}}$ for the BLIP and high-frequency domains, respectively.

A convenient nomograph based on the above scaling relations is shown schematically in Fig. 2.4. The quantity plotted is the relative $\overline{\text{NESR}} \times \alpha D$ vs. the relative dwell time t_d . The point (1,1) denotes the selected base-line system, whose dwell time is defined to be $\min t_d$, the lowest value for which BLIP performance can be achieved. According to Eqs. (34) and (38), $\overline{\text{NESR}} \times \alpha D$ varies $t_d^{-1/2}$ for t_d 's larger than $\min t_d$ (BLIP domain), and as $t_d^{-3/2}$ for relative t_d 's less than unity. Hence, the log-log plot has two lines of slopes $-1/2$ and $-3/2$ through the reference point (1,1); these curves are applicable provided only t_d is varied. The other lines of slope $-3/2$ in the non-BLIP region describe the $\overline{\text{NESR}} \times \alpha D$ variations with αD and/or $F^\#$ for the three types of detectors. Note that only one set of labels for these curves is applicable in a specific case, depending on which of the three types of detector is employed.

From Eqs. (31) and (22) of Section 2.5, the dynamic range (DR) in the interferogram varies as

$$\text{DR} \sim \frac{F^\# \alpha D J^{1/2}}{(\Delta f)^{1/2}} \sim \frac{F^\# \alpha D t_d^{1/2}}{D^*} \quad (39)$$

But in the BLIP domain, $D^* \sim F^\#$ to a very good approximation, and

$$\text{DR} \sim (\alpha D) t_d^{1/2} \quad (40)$$

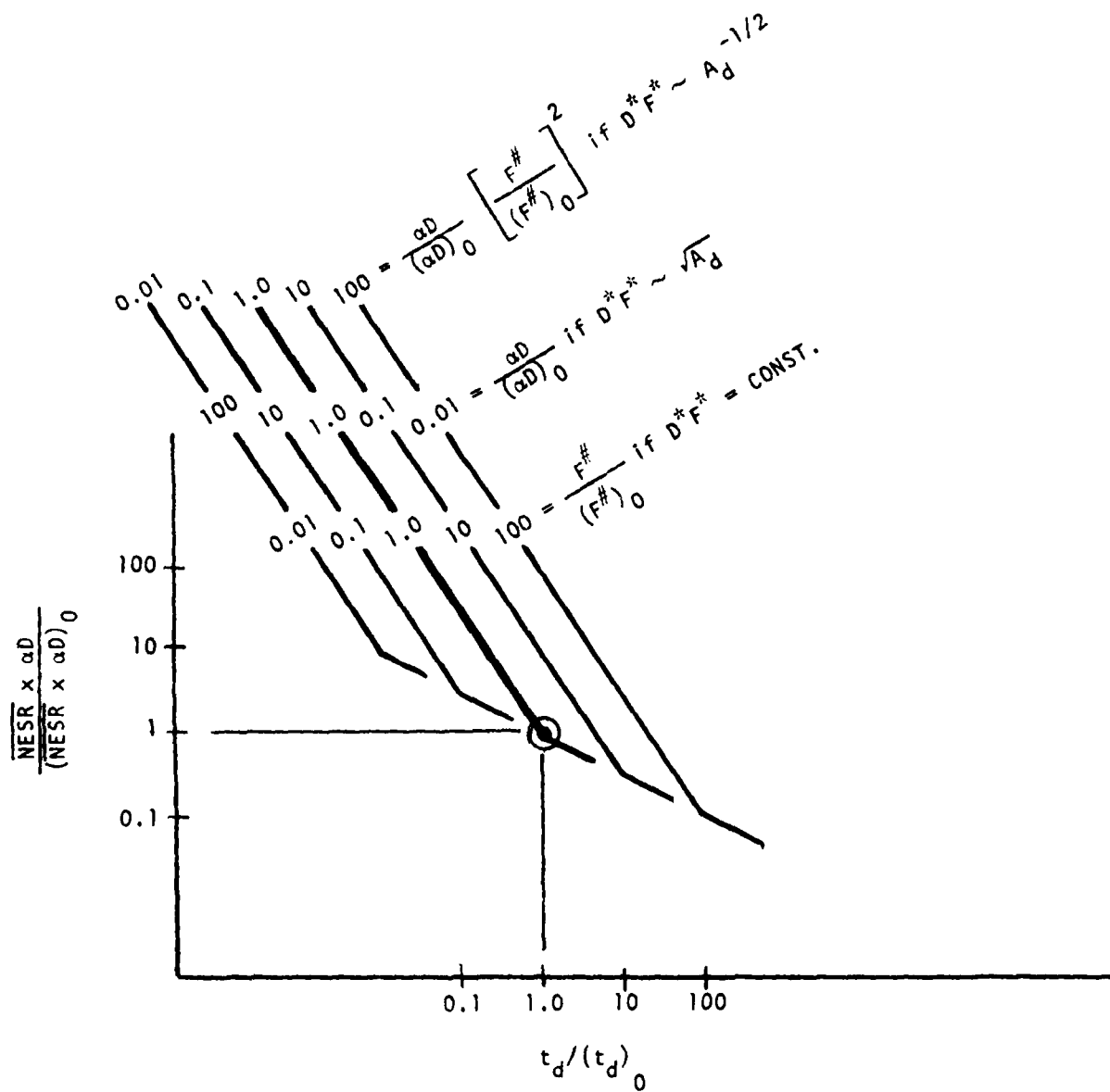


Figure 2.4 Schematic of an $\overline{\text{NESR}}$ Scaling Nomograph

In the region of detector-amplifier limited performance D^* varies as Eq. (37) if $D^*F^* \sim A_d^{1/2}$. Combining (37) and (39), we obtain

$$DR \sim \frac{1}{t_d^{1/2}} ; \quad (41a)$$

(again, $\Delta\nu$ is assumed fixed). The equivalent relation for detectors with area-independent D^*F^* is

$$DR \sim \frac{(\alpha D) F^\#}{t_d^{1/2}} , \quad (41b)$$

while for detectors with $D^*F^* \sim A_d^{-1/2}$, it is

$$DR \sim \frac{(\alpha D)^2 (F^\#)^2}{t_d^{1/2}} . \quad (41c)$$

A nomograph based on the dynamic range scaling relations is shown schematically in Fig. 2.5. This nomograph is used in the same manner as the NESR nomograph of Fig. 2.4. More detailed versions of the nomographs and examples of their use are given in Section 1.4.

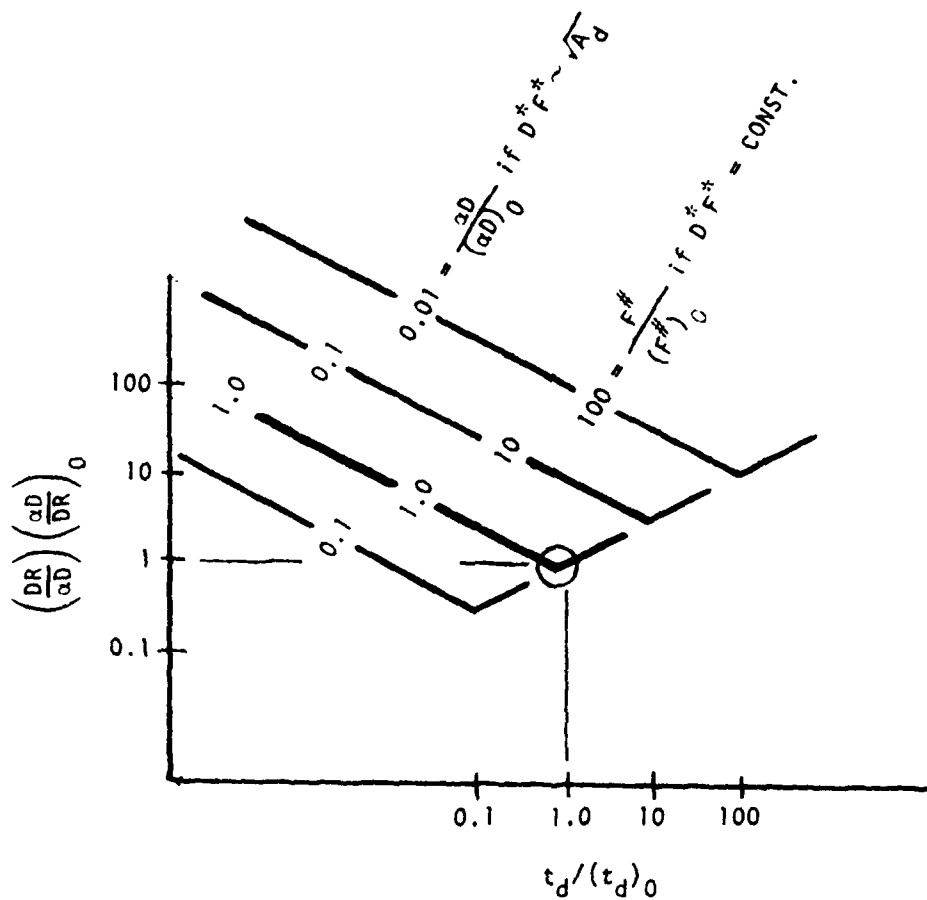


Figure 2.5 Schematic of a Dynamic Range Scaling Nomograph

SECTION 3

THE BASELINE SYSTEMS

Early in the study, we developed four FTS system concepts representing levels of technology ranging from "completely proven" to beyond the state-of-the-art.* The original intention was to determine the detection capabilities of four corresponding configurations for a variety of target, atmospheric and background conditions, as a function of target range and available measurement time.

It was realized subsequently that the performance of the most advanced concept could not be estimated unless efforts beyond the scope of the study were undertaken to determine the characteristics of the large-mosaic detectors and some of the optical elements. Also, the consensus of those present at an early Air Force program review meeting was that one of the proposed concepts was basically not viable, but had features that could be usefully employed in one of the less advanced concepts. Thus, the number of baseline configurations was reduced to three, and the decision was made to evaluate only the second, and not discuss the third further. It was agreed also that nomographs would be developed to allow the performance of the selected baseline configuration to be scaled with respect to basic radiometric parameters such as collector diameter, detector IFOV and measurement time.

Tables 3.1 and 3.2 define the general characteristics of the baseline FTS configurations. Configuration 1 consists of a conventional Michelson interferometer cube and drive mechanism with a four by four mosaic of detectors, a series of cold filters that can be introduced sequentially (or

*The system concepts were selected with the help of Bartlett Systems, Inc.

Table 3.1 Baseline Configuration I

SYSTEM	<p>CONVENTIONAL SINGLE-PORT MICHELSON INTERFEROMETER WITH MOSAIC FOCAL PLANE</p> <p>Resolved spectral interval, $\Delta\nu = 0.10 \text{ cm}^{-1}$ (one-sided interferogram)</p> <p>Spectral range, 3.3-12.6 μm (one beamsplitter)</p> <p>Number of cold filtered spectral bands ≈ 20</p> <p>Cold filter spectral width $\sim 25 \text{ cm}^{-1}$ to $\sim 200 \text{ cm}^{-1}$</p> <p>Scan time, TBD for each species; nominally 10 secs.</p> <p>Scans per target (number of bands per target facility or co-adds per single band), 10</p>
OPTICS	<p>Collector diameter, $D = 4$ inches</p> <p>$F\# = 3$</p> <p>IFOV = 0.656 mrad (≈ 10 m footprint at 50,000 foot range)</p> <p>Overall system efficiency, $\bar{\epsilon} \approx 0.22$</p> <p>Emissivity to detector, $\bar{\epsilon} \approx 0.17$</p> <p>Optical transmission, $\tau \approx 0.29$</p> <p>Cooling: cold shield, spectral filter and f-cone cooled sufficiently to contribute negligible background.</p> <p>Telescope uncooled or cooled passively.</p>
DETECTORS	<p>Material: Si:Ga, Si:Bi or HgCdTe</p> <p>Element size, $x = 9.5 \text{ mils} = 0.24 \text{ mm}$</p> <p>Array size, $4 \times 4 = 16$ detectors</p>
SIGNAL PROCESSING	<p>Subtraction of pairs of IFOV's</p> <p>Gain switching, 6 bits,</p> <p>A/D conversion, 15 bits (32,000 resolution levels)</p>

Table 3.2 Baseline Configuration 2

SYSTEM	<p>FOUR-PORT INTERFEROMETER WITH TWO DICHOIRCS AND FOUR SPECTRALLY OPTIMIZED DETECTOR ARRAYS</p> <p>Resolved spectral interval, $\Delta\nu = 0.10 \text{ cm}^{-1}$ (one-sided interferogram)</p> <p>Spectral range, 3.3-12.6 μm (one beamsplitter)</p> <p>Number of cold filtered spectral bands, ≈ 20</p> <p>Cold filter spectral width $\sim 25 \text{ cm}^{-1}$ to $\sim 200 \text{ cm}^{-1}$</p> <p>Scan time, t_d = minimum value for BLIP performance.</p> <p>Scans per target (number of bands per target facility or co-adds per single band), 40</p>
OPTICS	<p>Collector diameter, $D = 4$ inches</p> <p>$F\# = 3$</p> <p>IFOV = 0.656 mr (≈ 10 m footprint at 50,000 foot range)</p> <p>Overall system efficiency, $\bar{\epsilon} \approx 0.20$</p> <p>Emissivity to detector, $\bar{\epsilon} \approx 0.25$</p> <p>Optical transmission, $\tau \approx 0.26$</p> <p>Cooling: cold shield, spectral filter and f-cone cooled sufficiently to contribute negligible background.</p> <p>Telescope uncooled or cooled passively.</p> <p>Optical layout: see Fig. 3.1</p>
DETECTORS	<p>For 3.2-3.7 μm region, InSb</p> <p>For 3.7-4.5 μm region } InSb</p> <p>For 4.5-4.8 μm region }</p> <p>For 7.5-13.0 μm region, HgCdTe or Si:xx (xx = Ga, Bi or As)</p> <p>Element size, $x = 9.5$ mils = 0.24 mm</p> <p>Array size (four arrays), $4 \times 4 = 16$ detectors per array</p>
SIGNAL PROCESSING	<p>Background reduction effected by second input port (2nd FOV or internal reference). May not require gain switching.</p>
ADVANTAGES	<p>Dichroic separation permits simultaneous examination of four spectral regions (simultaneous detection of more species, and greater detectability of species). Significant dynamic range reduction due to second input port.</p>

possibly a cold CVF). The system operates at a spectral resolution of 0.1 cm^{-1} , and has an IFOV (each detector) of 0.656 mr. The scan time is considered a variable that can be adjusted according to mission constraints and/or the number of different target species that must be detected during the available measurement time. It was known (from Ref. 2) that the maximum dynamic range in the interferogram would be of the order of 2×10^6 (21 bits) which would require some method, such as gain switching, to reduce the dynamic range to the manageable value of 2^{15} . The system employs uncooled optics, but has a cold-shielded focal plane as well as cold filters.

Configuration 2 has the same foreoptics and gross radiometric specifications, but is a four-port interferometer employing two dichroics. The diagram of Fig. 3.1 shows that replacement of the two plane mirrors of the conventional scanning Michelson by corner reflectors results in dual input/output ports. Dichroics in the two output ports channel the encoded radiation to four separate cold-filtered detector mosaics, covering different portions of the total 2.9 - 13 μm spectral range. This arrangement allows "simultaneous" detection of up to four species, and increased measurement time (greater detectability) for any single species.

In the configuration shown, the second input port allows illumination of the back side of the beamsplitter by a reference blackbody (although the illuminating source could instead be a different portion of the external scene). The effect is to subtract the reference blackbody spectrum from the input spectrum (or to subtract the spectra of displaced IFOV's), which corresponds to a potentially large reduction in the dynamic range of the interferogram.

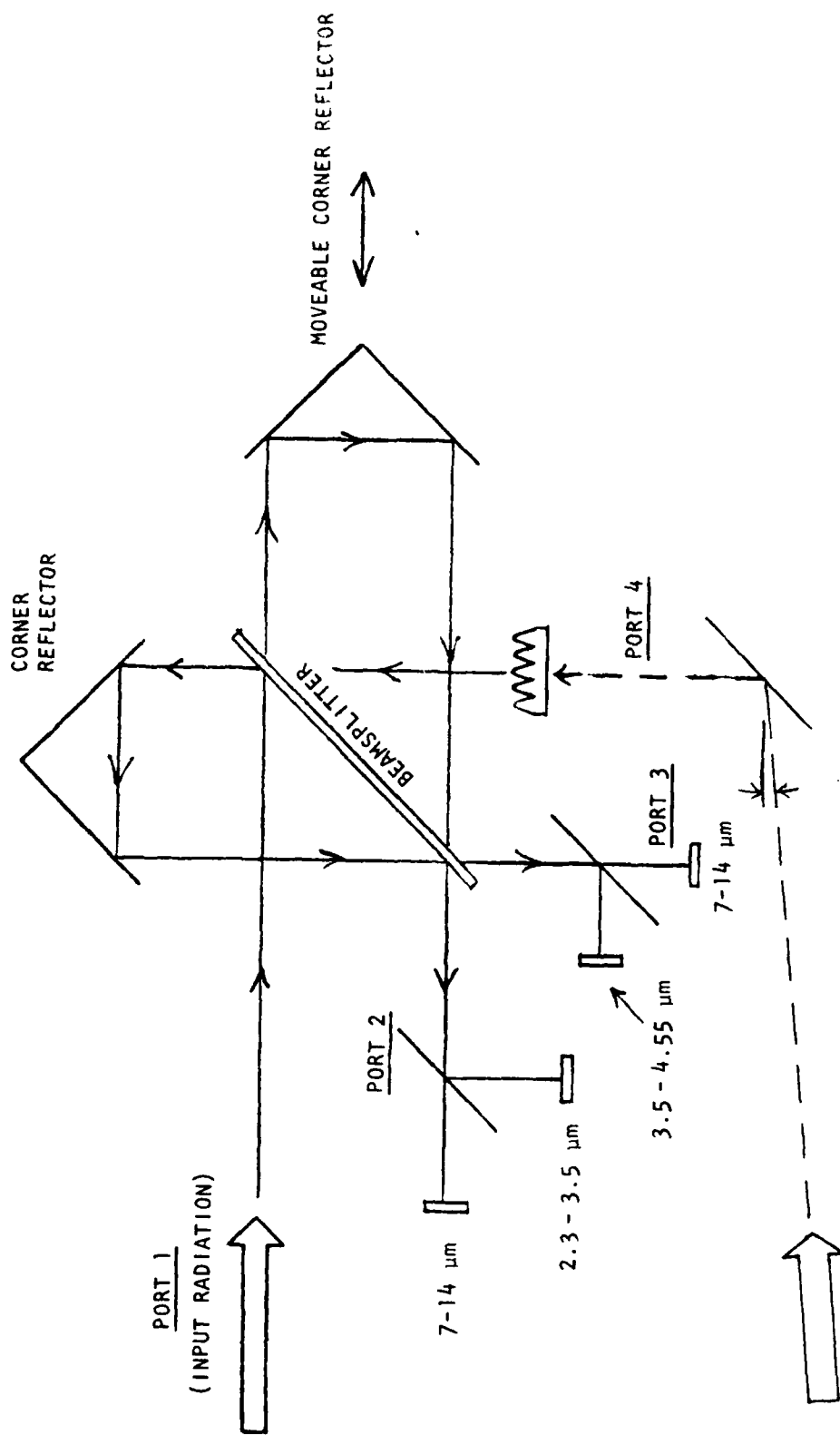


Figure 3.1 Optical Layout for Baseline Configuration 2

In the case where both input ports receive external radiation, the configuration performs an optical subtraction of the radiances reaching a given detector from different parts of the scene. Thus, it is not required to subtract the outputs of different detectors to suppress the background, as in Configuration 1. However, the noise in the difference spectrum (the signal to be analyzed) is the same for both configurations: a $\sqrt{2}$ increase in the NESR of Configuration 2 results from doubling the total band photon radiance on the BLIP detector (the effect of the second input port), whereas in Configuration 1 the effective $\sqrt{2}$ increase is the result of subtracting two independent noise signals.*

If the second input port is a blackbody reference channel, and the continuum portion of the external scene spectrum is approximately a blackbody at the same temperature as the internal reference, then it is, again, not necessary to subtract the outputs of different detectors. The decision to use an internal versus external reference should be based on the expected spatial homogeneity of the background, the expected amount of spectral structure in the background (this determines the maximum reduction in dynamic range using the blackbody reference), the ability to predict the average spectral radiance of the background, and the impact of the decision on optical design complexity.

The MDQ values given in Section 1 and Vol. II represent Baseline Configuration 2. The assumed radiometric properties (reflectivities, emissivities, etc.) of the optical elements of Configuration 2 are given in Section 1.

* Actually, the photon flux from external sources in Configuration 2 would be doubled, but the flux from internal sources would increase by somewhat less than a factor of 2. The assumption of $\sqrt{2}$ increase in NESR is, therefore, somewhat pessimistic.

It should be noted that the effects on \overline{NESR} of port 4 are not included in the \overline{NESR} values tabulated in Section 1 and Vol. 11; rather, the $\sqrt{2}$ increase is attributed to IFOV subtraction in the data processing. If the band photon radiances (BPR's) given in these sections are used to evaluate detector performance at different background flux levels for Configuration 2, the BPR's should be increased by a factor of 2. Note, also, that the scan time is fixed at the minimum value corresponding to background-limited performance ($\min t_d$) in order to facilitate scaling via the nomographs given in Section 1.4.

SECTION 4

EFFECTS OF ATMOSPHERIC TRANSMITTANCE (RADIANCE) VARIATIONS AND OFF-NADIR VIEWING

4.1 Summary

The minimum detectable amounts of the target gases depend, in part, on the transmittance/emission properties of the intervening atmosphere, which, in turn, are determined by the atmospheric composition and number of air masses in the line-of-sight. We recall that the minimum detectable quantity (MDQ) corresponding to specified detection and false detection probabilities is inversely proportional to $\sigma' / (\sqrt{2} \overline{\text{NESR}})$ where σ' is the standard deviation of the normalized contrast spectrum $\tau_v \alpha_{gv}$, and $\overline{\text{NESR}}$ is the average system noise equivalent spectral radiance over the detection band. The atmospheric transmittance τ_v in the regions of target emission lines influences σ' , while the atmospheric band photon radiance (and its background absorption) affect the system $\overline{\text{NESR}}$. In this section we consider the effects on MDQ of substituting the Midlatitude Winter model atmosphere for the Midlatitude Summer model, and the effect of increasing the nadir view angle from 0 to 45 degrees. Because of the amount of computation involved, we evaluated the MDQ variations for only six of the 15 selected detection bands. However, these are representative of the range of variations to be expected for all detection bands.*

MDQ was defined as the minimum detectable target gas column thickness per unit difference between the average spectral radiances of blackbodies at the target and background temperatures. As long as column thickness (number

* The choice of NO_2 detection band was changed after this work was performed on the basis of new information on band strengths. This section treats the $\nu_1 + \nu_3$ band, but the preferred detection band is NO_2 (ν_2).

of observed molecules per unit area) is measured along the line-of-sight and the target always fills the IFOV, there are no geometrical "range-squared" or "cos θ " effects in calculating the MDQ. Of course, the "quantity available for detection" can depend on the viewing angle and range, depending on the details of the target plume and viewing geometries. Hence, minimum detectable mass flow rates or effluent densities may depend explicitly on the nadir view angle, as well as on the calculated MDQ. For example, if the MDQ, as defined above, happened to increase by the factor 1.1 in going zero to 45 degrees, and the target gas were represented as a slab parallel to the earth's surface, then, since the quantity available for detection increases by the factor $\cos 45^\circ = \sqrt{2}$, the minimum detectable volume concentration would change by the factor $1.1/\sqrt{2}$; i.e., it would actually decrease.

The MDQ, as defined above, varies as

$$\begin{aligned} \text{MDQ} &\sim \frac{\overline{\text{NESR}}}{\sigma} \\ &\sim (J)^{1/2}/\sigma \\ &= [\text{BPR} \cdot 0.0228 + J_I]^{1/2}/\sigma \end{aligned} \quad (1)$$

where J is the total photon flux density on the detector, J_I is the photon flux density contribution of internal sources, and BPR is the band photon radiance of the external scene (atmosphere plus background). The factor 0.0228 converts band photon radiance to detector photon flux density for the baseline system (optics transmission = 0.261 and $F^\# = 3.0$).^{*} Thus, the MDQ's calculated for the Midlatitude Summer model atmosphere and nadir

^{*} See Eq. (23) in Section 2.5.

viewing can be scaled easily to other cases provided that BPR and σ' are determined for the other cases.

The model atmospheres most readily useable for FASCOD1 computations of τ_v (or σ') and in computations of the band photon radiance are the six incorporated into the LOWTRAN series of computer codes. The most significant differences among the models are the total vertical water vapor amounts, which are listed in Table 4.1 in units of precipitable centimeters (pr. cm). Note that there is a ten-fold variation in total H_2O between the wettest and driest models, and that the two models selected to represent atmospheric effects in the MDQ (the Midlatitude Summer and Winter models) represent total moisture amounts of 3.0 and 0.87 pr. cm. (which differ by a factor of 3.5). These variations can be expected to have significant effects on the MDQ for molecules whose detection bands coincide with regions of H_2O absorption. By comparison, a nadir viewing angle change from 0 to 45 degrees causes a relative increase in air mass of only $\sqrt{2}$ for all atmospheric species.

Table 4.1 Vertically Integrated Moisture Content w of the LOWTRAN Model Atmospheres

Model No.	Name	w (pr. cm.)
1	Tropical	4.2
2	Midlatitude Summer	3.0
4	Subarctic Summer	2.1
6	1962 U.S. Standard	1.43
3	Midlatitude Winter	0.87
5	Subarctic Winter	0.42

The LOWTRAN models encompass nearly the full range of moisture amounts encountered in the atmosphere and are quite representative of different latitude zones. This is illustrated in Fig. 4.1, taken from Rosen et al.⁹, which shows the latitude variation of the H_2O column thickness (after

averaging over longitude) for six years of observation. Superimposed on Rosen's plot are the H_2O column thicknesses represented by the LOWTRAN model atmospheres (Table 4.1).

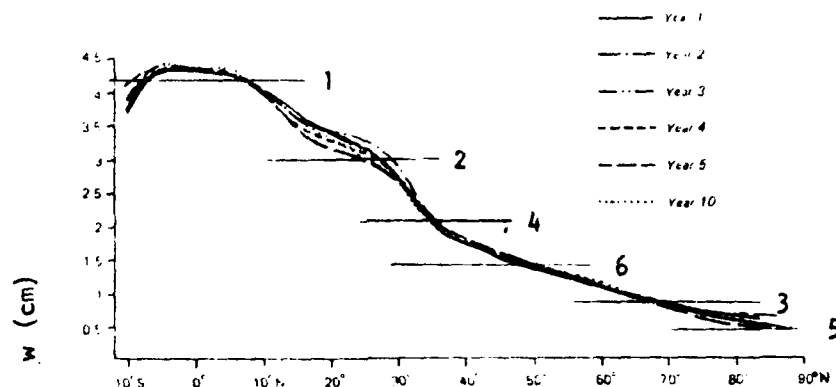


Figure 4.1 Meridional Profiles of the Zonal Mean Vertically Integrated Moisture Content $[w]$ for each of the Years Studied. From Rosen et al.⁹

The results of the calculation of MDQ variation with model atmosphere and nadir viewing angle are summarized in Table 4.2. The table gives the lowest and highest values of relative MDQ which correspond, respectively, to the combinations:

- a.) Midlatitude Winter, nadir angle = zero, and
- b.) Midlatitude Summer, nadir angle = 45° .

Table 4.2 Maximum Variation of MDQ for the Model Atmospheres/Nadir Angles Considered

Molecule, Band (cm^{-1})	MDQ relative to Ref. case	
	(lowest)	(highest)
NO_2 (2850-2935)	0.75	1.05
HCl (2900-3000)	0.73	1.53
DF (2700-2900)	0.75	1.06
HBr (2450-2650)	0.74	1.05
CH_4 (1295-1310)	0.39	2.80
SO_2 (1090-1210)	0.53	1.26

The values in the table are relative to the MDQ's reported in Section 1 for the Midlatitude Summer case and nadir angle = zero; i.e., a value of 0.5 indicates that the MDQ is one-half of the previously reported value (the molecule is "more easily detectable" by a factor of two).

It should be noted that the Winter model was used in combination with an assumed surface temperature of 273°K (H_2O freezing point): The MDQ's for most of the selected detection bands vary strongly with surface temperature (through the BPR), because most of the bands coincide with regions of high atmospheric transmittance.

The results of Table 4.2 show that the MDQ varies by a factor of less than 2.4 between the lowest and highest values, except for CH_4 , where the ratio of highest and lowest MDQ is approximately 7. These relative variations are explained by the fact that the methane detection band is in a region of strong water vapor absorption, while the other detection bands contain only isolated H_2O lines and/or a relatively weak H_2O continuum. It is recalled that CH_4 was one of the molecules that is difficult to detect through a Midlatitude Summer atmosphere (the minimum detectable concentration for a 10-meter cloud thickness and 5°C temperature difference was 163 ppmV). The implication of the results in Table 4.2 is that CH_4 might be easily detectable through a dry Arctic atmosphere, and might be impossible to detect in useful quantities in the Tropics. It is possible that the CH_4 ν_3 band in the 3000-3025 cm^{-1} region would be a better choice than the ν_4 band for the tropical case.

The results shown in Table 4.2 for SO_2 represent an approximate upper limit on the MDQ variation for all molecular detection bands in the 8 - 12.7 μm region (the selected NH_3 , HNO_3 , $C_2H_4O_2$ and CH_3I bands). The

results obtained for NO_2 , HCl , DF and HBr are roughly indicative of the results that would be expected for the N_2O , CO and HI detection bands. These conclusions are based on comparisons of LOWTRAN average transmittances for the different detection bands.

4.2 Details of the Calculations

The six particular detection bands appearing in Table 4.2 were selected on the basis of several considerations. First, we wished to represent molecules with sparse line spectra (such as HCl and DF), as well as those with overlapping spectral lines (such as NO_2). We also wanted to include bands of both high and low atmospheric transparency, and bands at short and long wavelengths (the InSb and HgCdTe detector regions). To facilitate the selection of bands we performed LOWTRAN 4 calculations to obtain, for all of the 15 detection bands, values of average spectral transmittance for both the Midlatitude Winter and Summer model atmospheres and for nadir view angles of zero and 45 degrees. These results are shown in Table 4.3.

Table 4.3 shows that the average band transmittances are generally greater than 33 percent, with the exceptions of the CO_2 band (which is somewhat of a special case) and the HF and CH_4 bands, which are in regions of strong H_2O absorption. It is interesting to note that the average transmittance is higher over the HF band than it is over the CH_4 band even though we found that CH_4 was detectable and HF was not. One of the reasons for this apparent inconsistency is that the average (low-resolution) transmission is not representative of the transmissions at the line centers in the case of a molecule with widely separated lines. In fact, the spectral contrast plot given in Vol. II for HF at 300°K contains only the P11 and P12 lines of the 1-0 band. The detection band also includes the P13 and P14 lines at

Table 4.3 Average atmospheric spectral transmission over the selected detection bands for Midlatitude Winter and Summer model atmospheres and nadir view angles of 0 and 45 degrees. (Computed using LOWTRAN 4).

Molecule (Detection Band)	Nadir View Angle (Degrees)	AVERAGE TRANSMISSION	
		Winter	Summer
HF(3240-3440)	0	0.276	0.088
	45	0.214	0.053
HCl(2900-3000)	0	0.565	0.400
	45	0.500	0.328
NO ₂ (2850-2935)	0	0.767	0.644
	45	0.721	0.577
DF(2700-2900)	0	0.853	0.737
	45	0.820	0.681
HBr(2450-2650)	0	0.874	0.833
	45	0.835	0.785
CO ₂ (2375-2400)	0	0.174	0.171
	45	0.124	0.121
N ₂ O(2160-2210)	0	0.442	0.407
	45	0.374	0.339
CO(2130-2185)	0	0.681	0.584
	45	0.622	0.516
HI(2100-2200)	0	0.616	0.530
	45	0.553	0.460
CH ₄ (1295-1310)	0	0.169	0.069
	45	0.117	0.038
SO ₂ (1090-1210)	0	0.836	0.648
	45	0.796	0.566
NH ₃ (915-970)	0	0.904	0.686
	45	0.874	0.595
HNO ₃ (887.5-902.5)	0	0.923	0.659
	45	0.896	0.562
C ₂ H ₄ O ₂ (880-1000)	0	0.873	0.661
	45	0.837	0.567
CH ₃ I(790-990)	0	0.880	0.615
	45	0.845	0.515

3326.21 cm^{-1} and 3369.90 cm^{-1} , but these apparently coincide with very strong atmospheric H_2O lines, and, hence, do not appear in the contrast spectrum.

The LOWTRAN 4 average transmittances, although not accurate indicators of available signal radiance for the HF, HCl, DF, HBr, CO and HI bands, are still useful for determining which of these bands are most likely to be affected by atmospheric variations. Based on the values in Table 4.3, and the other considerations mentioned above, we selected NO_2 , HCl, DF, HBr, CH_4 and SO_2 as a subset of detection bands that should adequately represent the effects of atmospheric and nadir angle variations.

The low-resolution spectral transmittances obtained from LOWTRAN 4 (in the process of computing the average band transmittances) were plotted for the two extreme cases: Midlatitude Winter, vertical viewing (maximum spectral transmittance), and Midlatitude Summer, 45-degree viewing (minimum transmittance). The 16 selected detection bands and the several other candidate bands considered are indicated in the spectra (Figure 4.2). This figure is a convenient display of the locations of the detection bands relative to the major atmospheric absorption bands.

The relative MDQ's for the four different cases were obtained by evaluating Eq. (1) and normalizing with respect to the value obtained for the reference case: Midlatitude Summer and nadir view angle $\theta = 0$. The results will be displayed in the matrix format defined in Fig. 4.3. Note that two values of relative MDQ are given for each of the winter cases. The values in parentheses correspond to an assumed surface temperature of 300°K, the same value used with the Midlatitude Summer model atmosphere. The other values correspond to an assumed surface temperature of 273°K (32°F), which is a more realistic surface temperature for a winter model. By providing

Figure 4.2 Atmospheric transmittance of a vertical path through the Midlatitude Winter model atmosphere (upper curve) and a path at 45 degrees zenith angle through the Midlatitude Summer model atmosphere (lower curve). Figure 4.2a covers the 600-1200 cm^{-1} region, Fig. 4.2b the 1200-1800 cm^{-1} region, Fig. 4.2c the 1800-2400 cm^{-1} region, Fig. 4.2d the 2400-3000 cm^{-1} region, and Fig. 4.2e the 3000-3600 cm^{-1} region. The selected detection bands (solid bars) are indicated, as well as the other candidate detection bands considered for NO_2 , N_2O , CH_4 and SO_2 (dashed bars). The transmittance spectra were computed using the LOWTRAN 4 code.⁴

Figure 4.2a The 600-1200 cm^{-1} region

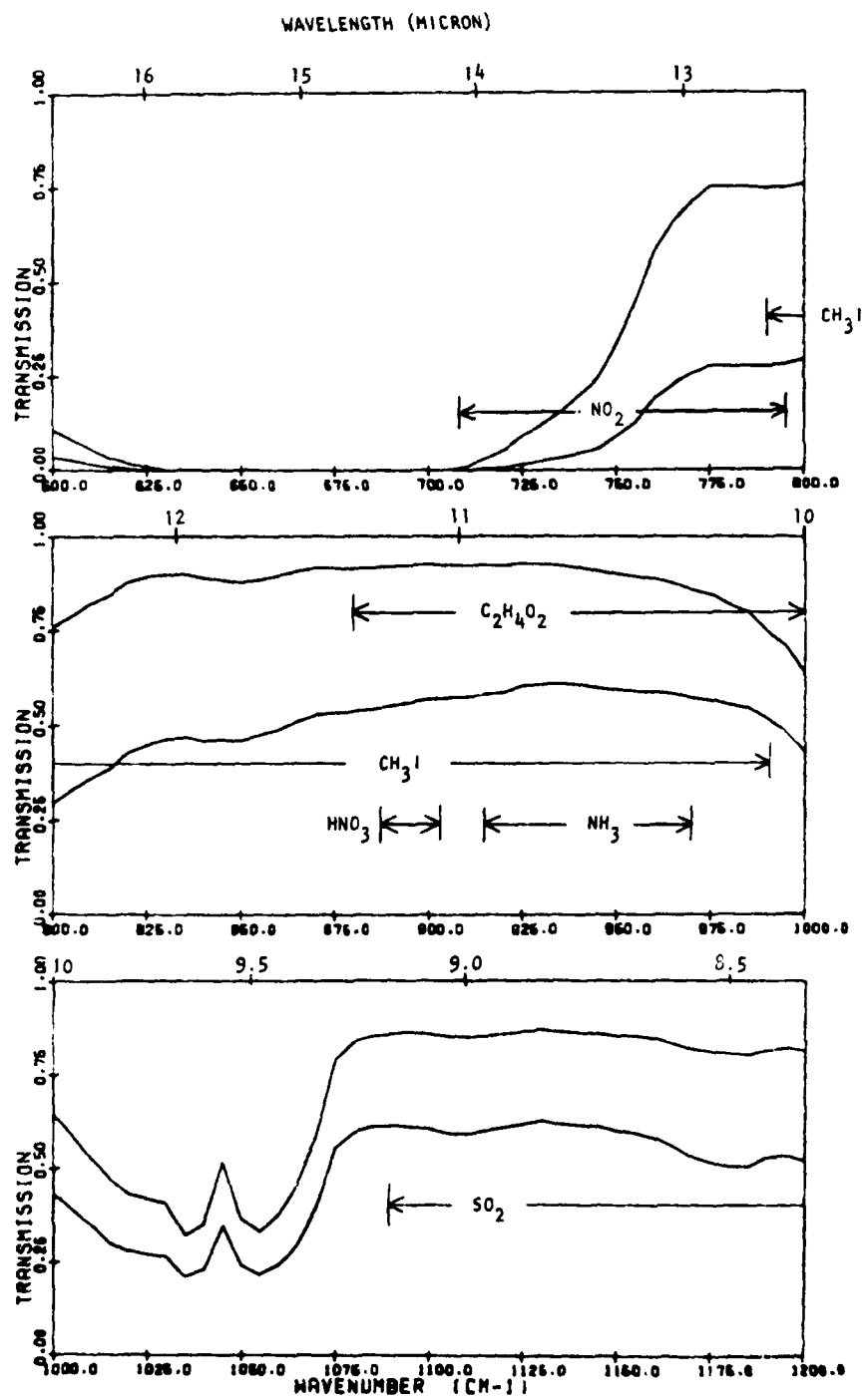


Figure 4.2b The 1200-1800 cm^{-1} region

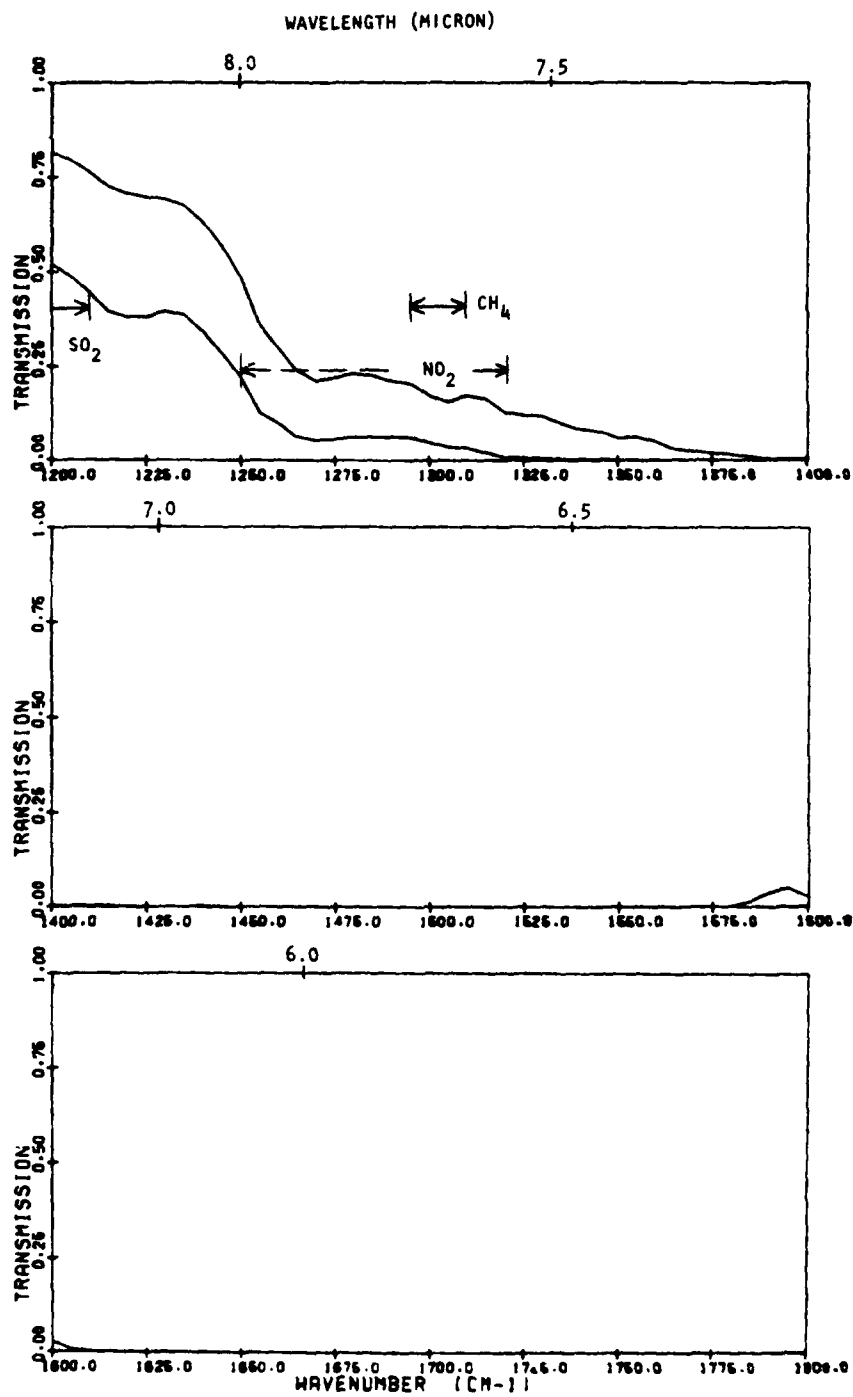


Figure 4.2c The 1800-2400 cm^{-1} region

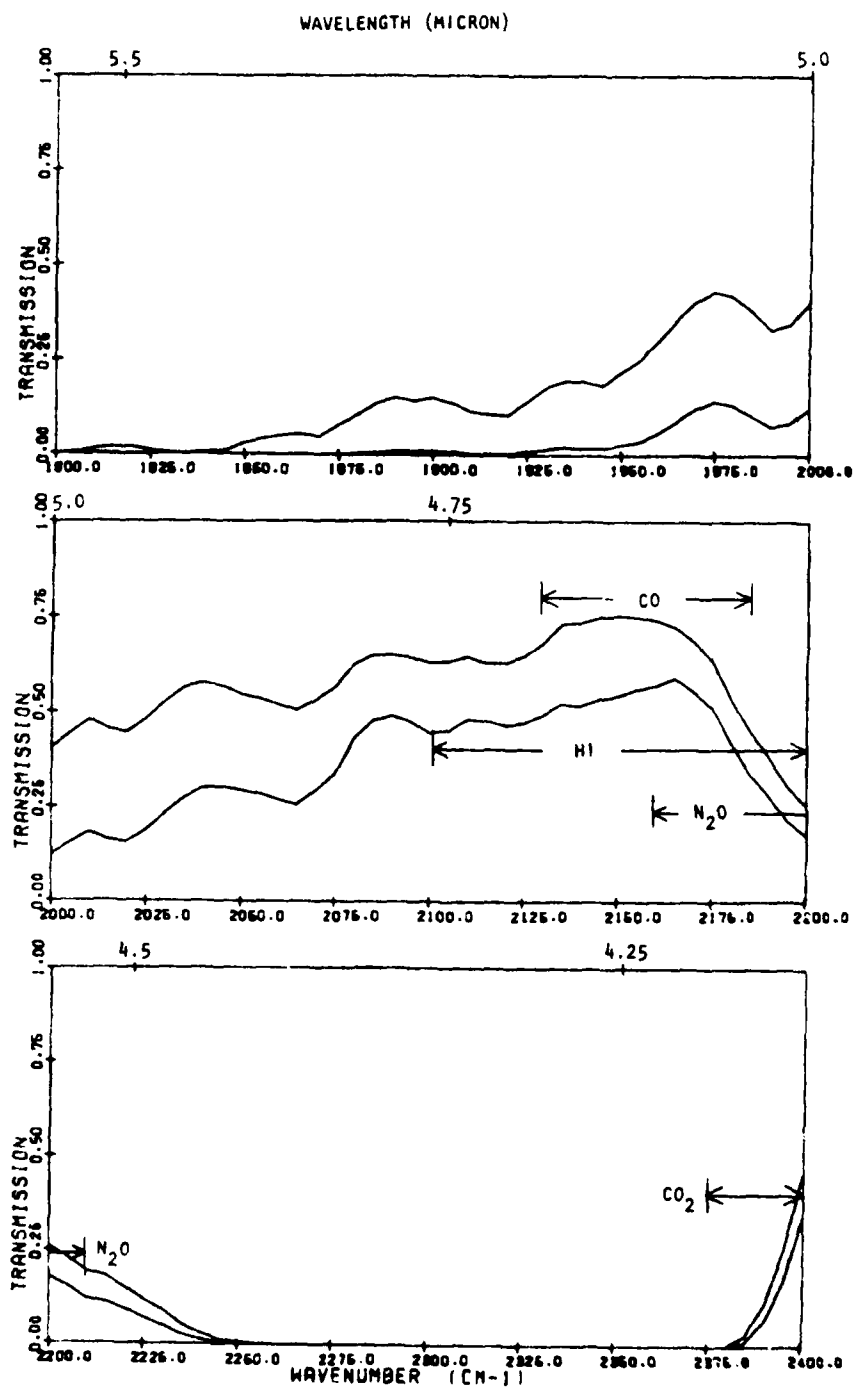


Figure 4.2d The 2400-3000 cm^{-1} region

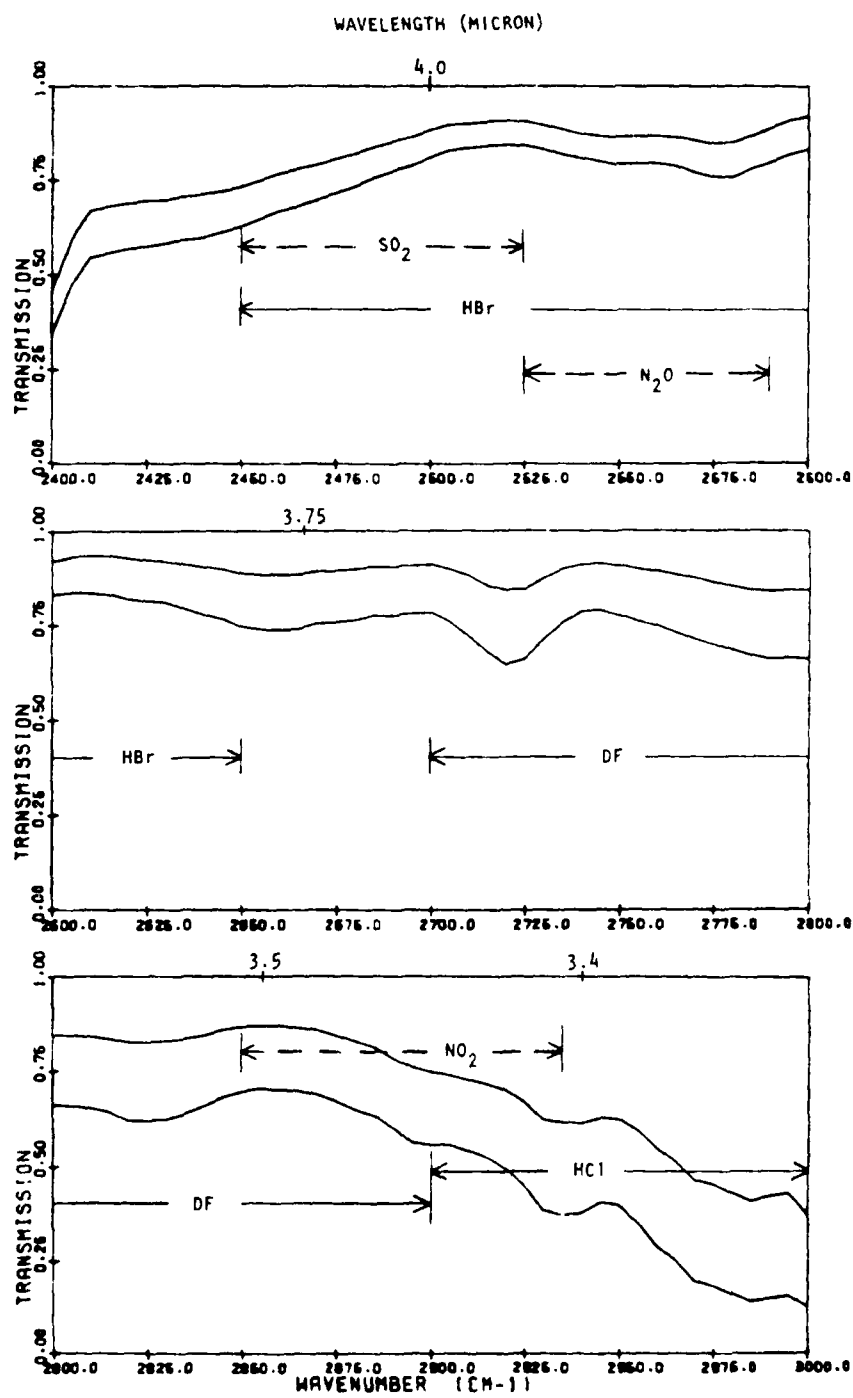


Figure 4.2e The 3000-3600 cm^{-1} region

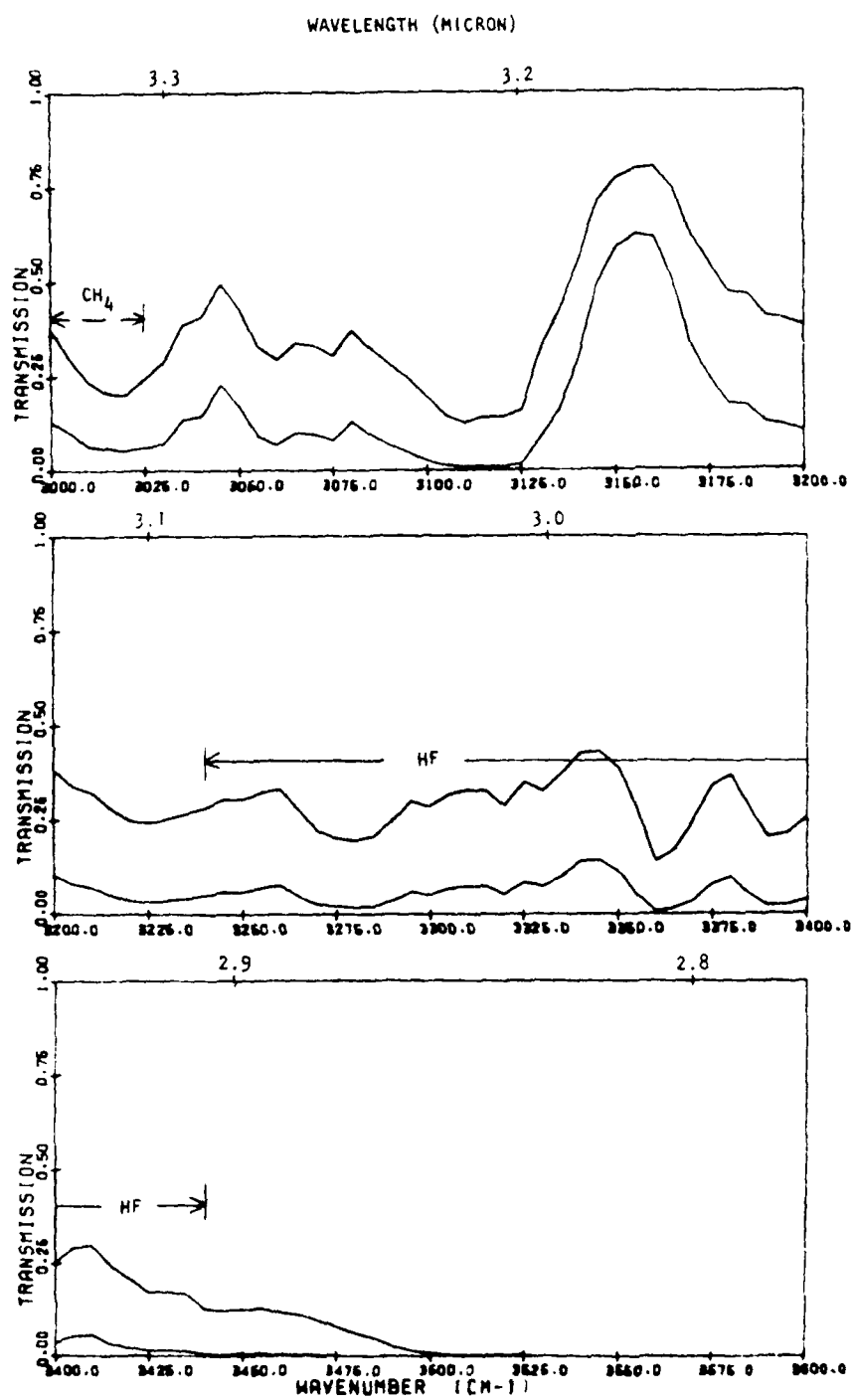


Figure 4.3 Format of Table 4.4 for Relative MDQ Values

		Midlatitude Atmosphere	
		<u>WINTER</u>	<u>SUMMER</u>
Angle from nadir	<u>$\theta = 0$</u>	XX (XX)	1.0
	<u>$\theta = 45^\circ$</u>	XX (XX)	XX

the results for both temperatures, we can assess how much of the MDQ variation results from atmospheric variations as compared to background temperature variations. It is emphasized that background temperature variations affect the MDQ only through the system \overline{NESR} ; the difference between target and background temperature is of consequence only when MDQ is converted to minimum detectable column thickness or minimum detectable volume concentration.

The final results are displayed in Table 4.4. In addition to relative MDQ, we show the corresponding band photon radiances BPR in photons/sec cm^2 sr and the standard deviation σ' of the contrast spectral radiance; these are shown as pairs of matrix elements with the uppermost value equal to the BPR. Beneath each BPR, σ' matrix we give the value of the photon flux density on the detector due to internal sources. These additional values allow recalculation of the total photon flux density on the detector, the system \overline{NESR} , and required dynamic range.

Note that for the first four molecules in Table 4.4 the background temperature has a much larger effect on MDQ than the model atmosphere. For SO_2 the model atmosphere and background temperature both have significant

AD-A108 299

UTAH STATE UNIV LOGAN ELECTRO-DYNAMICS LAB
DOWN-LOOKING INTERFEROMETER STUDY II, VOLUME I.(U)
MAR 80 A S ZACHOR

F/O 13/2

UNCLASSIFIED

SCIENTIFIC-2

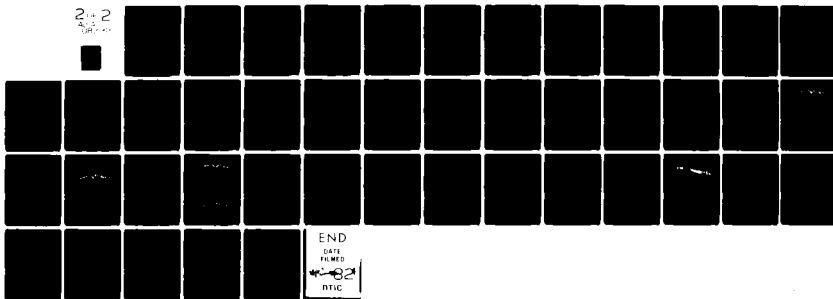
AFGL-TR-80-0236

F19628-77-C-0203

NL

2-2
2-2

2-2



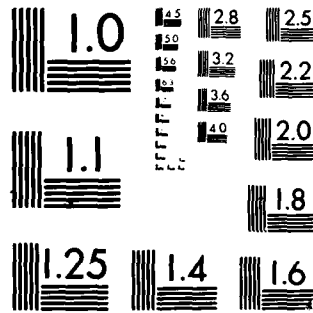
END

DATE

FILMED

82

DTIC



MICROCOPY RESOLUTION TEST CHART
NATIONAL BUREAU OF STANDARDS-1963-A

Table 4.4 Relative MDQ, Band Photon Radiances, and σ' for Midlatitude Winter and Summer Model Atmospheres and for $\theta = 0$ and 45 Degrees

Molecule (Detection Band)	Relative MDQ		Band Photon Radiance, and σ'	
NO ₂ (2850-2935)	0.75(0.90)	1.0	$1.28(3.54) \times 10^{13}$	3.41×10^{13}
			2.22×10^{-20}	1.99×10^{-20}
	0.77(0.92)	1.05	$1.29(3.41) \times 10^{13}$	3.26×10^{13}
			2.17×10^{-20}	1.88×10^{-20}
			8.5×10^{11}	
HCl (2900-3000)	0.73(0.84)	1.0	$1.10(2.71) \times 10^{13}$	2.56×10^{13}
			1.18×10^{-19}	9.81×10^{-20}
	1.08(1.23)	1.53	$1.11(2.53) \times 10^{13}$	2.37×10^{13}
			7.94×10^{-20}	6.32×10^{-20}
			8.0×10^{11}	
DF (2700-2900)	0.75(0.92)	1.0	$0.43(1.30) \times 10^{14}$	1.23×10^{14}
			1.04×10^{-19}	9.39×10^{-20}
	0.78(0.94)	1.06	$0.42(1.26) \times 10^{14}$	1.18×10^{14}
			1.00×10^{-19}	8.78×10^{-20}
			3.0×10^{12}	
HBr (2450-2650)	0.74(0.91)	1.0	$1.05(3.40) \times 10^{14}$	3.39×10^{14}
			2.31×10^{-20}	2.10×10^{-20}
	0.76(0.93)	1.05	$1.08(3.32) \times 10^{14}$	3.28×10^{14}
			2.25×10^{-20}	1.99×10^{-20}
			8.2×10^{12}	

effects, while for CH_4 , the MDQ is determined primarily by the atmosphere. Note also that for NO_2 , DF and HBr, the variation of nadir view angle has an almost negligible effect on MDQ.

SECTION 5

EFFECTS OF INACCURATE PREDICTIONS OF ATMOSPHERIC AND/OR TARGET GAS ABSORPTIONS, OF SPECTRAL INTERFERENCES AMONG TARGET SPECIES, AND OF INCOMPLETE BACKGROUND SUBTRACTION

In Section 2, we defined a procedure for obtaining the statistics of a spectral correlation-detection process in which the only interference was system (detector) noise. That treatment ignored three "real-world" effects likely to degrade the system performance; these are

- a.) imprecise knowledge of the atmospheric spectral transmittance τ_v and/or target gas spectral absorption coefficient α_{gv} ,
- b.) spectral interferences (overlap) between two or more of the species to be detected, and
- c.) different line-of-sight atmospheric properties and/or backgrounds in the two IFOV's used to obtain the contrast spectral radiance; i.e., incomplete subtraction of the net atmosphere-plus-background spectral radiance.

The analysis portion of Section 2 consisted of developing a formula for the coefficient of correlation ρ between the measured contrast spectrum and a reference spectrum. We found that ρ could be expressed as a ratio involving statistical descriptors of the reference spectrum, the quantity of target gas present, the system \overline{NESR} , and combinations of independent unit normal variates. Repeated evaluations of this expression using computer-generated random numbers allowed us to determine the statistics of ρ , in particular, the detection/false detection probabilities corresponding to various threshold levels on ρ , as functions of the several free parameters in the expression. These results were used to determine minimum detectable target gas quantities corresponding to a baseline system \overline{NESR} and stated levels of detection probability and false detection probability.

In this section we will redefine the contrast spectral radiance and reference spectrum to include the three effects described above, and present corresponding generalized expressions for ρ . We will then present the results of computations that show the relative changes in minimum detectable quantity corresponding to assumed models of the interference effects. Derivations of the generalized equations for ρ are not included since these follow the same basic approach used in Section 2 (and Appendix A) for the ideal case.

5.1 Real-World Effects in the Observed Contrast Spectral Radiance

Let N , with subscripts 1 or 2, denote the total upwelling spectral radiance observed in two different IFOV's (subscripts v and g used in previous sections will be omitted to simplify the notation; e.g., τ_v will be written as τ , τ_1 or τ_2 and α_{gv} as α). The first IFOV contains no target gas, and observes spectral radiance

$$N_1 = N_1^a + \tau_1 N_1^s, \quad (1)$$

where N_1^a denotes the contribution of the atmosphere, and $\tau_1 N_1^s$ the contribution of the ground surface (background) with the effect of atmospheric transmittance (τ_1) included. The second IFOV, containing a cloud (slab) of the target gas at ground level, observes spectral radiance

$$N_2 = N_2^a + \tau_2 (1 - \tau^g) B(T^g) + \tau^g \tau_2 N_2^s, \quad (2)$$

where τ^g is the spectral transmittance of the gas slab, and $B(T^g)$ is the spectral radiance of a blackbody at the temperature T^g of the target gas. N_2^a , N_2^s and τ_2 are analogous to N_1^a , N_1^s and τ_1 , and represent the uncontaminated atmosphere and background viewed by the second IFOV, which may be different than those in the first IFOV. Equations (1) and (2) correspond to

infinite resolving power. Also, in Eq. (2), it is assumed that the atmospheric transmittance between the sensor and the top of the cloud can be approximated by the transmittance of the entire atmosphere (τ_2) when no gas cloud is present; this assumption is valid if the physical cloud thickness is small compared to one scale height of the atmosphere.

The contrast spectral radiance ΔN is equal to $N_2 - N_1$. If we add and subtract $\tau_2 N_2^S$ to N_2 , perform the subtraction and collect terms, the result is

$$\begin{aligned}\Delta N &= [N_2^a + \tau_2 N_2^S] - N_1 + \tau_2 (1 - \tau^g) B(T^g) - [\tau_2 N_2^S - \tau^g \tau_2 N_2^S] \\ &= N_2(\text{"no gas"}) - N_1 + \tau_2 (1 - \tau^g) [B(T^g) - N_2^S] \\ &\equiv \xi + \tau (1 - \tau^g) [B(T^g) - N^S]; \quad \xi \equiv N_2(\text{"no gas"}) - N_1.\end{aligned}\quad (3)$$

Here, ξ is defined as the difference in net spectral radiances produced by the (uncontaminated) atmospheres and backgrounds in the two IFOV's, and τ and N^S (note subscript "2" is omitted) are the transmittance of the atmosphere and the intrinsic background radiance in the IFOV containing the target.

If the target gas slab is optically thin, Eq. (3) reduces to

$$\begin{aligned}\Delta N &= \xi + \tau \alpha u [B(T^g) - N^S] \\ &\approx \xi + \tau \alpha u \langle B(T^g) - N^S \rangle,\end{aligned}\quad (4)$$

where $\langle \rangle$ denotes a spectral average, α is the spectral absorption coefficient of the target gas, and u is the optical thickness (column density) of the target cloud. To the extent that the spectral radiance difference ξ can be tolerated as an "error" in the spectral measurement, and $\tau \alpha$ (previously denoted $\tau_v \alpha_{gv}$) can be predicted, the detectable quantity is

$$D \equiv u \langle B(T^g) - N^S \rangle . \quad (5)$$

However, if we acknowledge that the measurement contains spectral noise n , and that the target may occupy a fraction F of the IFOV, the contrast spectral radiance becomes

$$\begin{aligned} \Delta N &= \xi + \tau \alpha F u \langle B(T^g) - N^S \rangle + n \\ &= D \tau \alpha + \xi + n , \end{aligned} \quad (6)$$

where the detectable quantity is now

$$D = F u \langle B(T^g) - N^S \rangle . \quad (7)$$

As in the ideal case (Section 2), u can be obtained from the inference of D , provided F and $\langle B(T^g) - N^S \rangle$ can be inferred independently. If, in addition, the physical thickness of the target cloud can be estimated, then the gas density or volume concentration can be determined.

Note that the definition (7) of the detectable quantity is the same as the one given in Section 2, except that the background is assumed to have an arbitrary radiance spectrum N^S rather than a blackbody spectrum $B(T^S)$. In order to treat D as a constant (spectral average), we must require that $N_2^S \equiv N^S$ not have spectral variations with structure comparable to that of $\tau \alpha$ or ξ , which is likely to be the case. Of course, ξ will have spectral structure comparable to that of $\tau \alpha$, since a component of ξ is the difference in atmospheric spectral radiances in the two IFOV's ($N_1^a - N_2^a$). It is likely that this component of ξ will degrade detection performance much more than possible differences in background surface spectral radiances.

Suppose there are other (unanticipated) gas species present in the target IFOV that have absorption lines or bands that overlap those of the target species: let D_1, D_2, \dots denote their detectable quantities ($D_n = F u_n < B(T^g) - N^S >$), and $\alpha_1, \alpha_2, \dots$ their spectral absorption coefficients. Then the actual contrast spectral radiance is

$$\Delta N = \tau D \left(\alpha + \alpha_1 \frac{D_1}{D} + \alpha_2 \frac{D_2}{D} + \dots \right) + \xi + n. \quad (8)$$

In the spectral correlation detection process proposed in this study, we attempt to detect the species of interest by thresholding on the normalized correlation between the measured contrast ΔN and a reference spectrum $\tau'\alpha'$, where τ' and α' represent estimates of τ and α . Specifically, the detection process consists of thresholding on the value of

$$\rho = \frac{\text{covariance of } \Delta N \text{ and } \tau'\alpha'}{(\text{std of } \Delta N) (\text{std of } \tau'\alpha')} \quad (9)$$

(std \equiv standard deviation)

It is evident that the detection probability and false target rejection capability will both be diminished by the noise term n , by the difference between $\tau\alpha$ and $\tau'\alpha'$, by the presence of interfering species (the terms $\alpha_1 D_1/D, \alpha_2 D_2/D, \dots$ in Eq. (8)), and by the residual atmosphere-background spectral radiance ξ . Equations 8 and 9 may be used to re-evaluate the statistics of ρ when one or more of the interference effects are included, and then to determine the corresponding increase in minimum detectable quantity for fixed detection/false detection probabilities. The following subsection concerns the development of parameterized expressions for ρ ; i.e., forms which do not require computer simulations involving the actual spectra $\tau\alpha$ and $\tau'\alpha'$.

5.2 Generalized Expressions for the Coefficient of Correlation ρ

Consider that the interference effects referred to above as a, b, and c each have "true" and "false" states, which we can denote as 1 and 0, respectively. The number of different combinations of states for all three effects is therefore $2^3 = 8$. We can label the combinations by the numbers 0 through 7, and readily identify the specific states by the binary equivalents of the labels:

<u>Combination</u>	<u>Effects</u>			(1 = "true", 0 = "false")
	<u>a</u>	<u>b</u>	<u>c</u>	
0	0	0	0	a(true) means
1	0	0	1	$\tau\alpha$ estimated by $\tau'\alpha'$
2	0	1	0	
3	0	1	1	b(true) means
4	1	0	0	$\alpha \rightarrow \alpha + \alpha_1 \frac{D_1}{D} + \dots$
5	1	0	1	
6	1	1	0	c(true) means
7	1	1	1	$\xi \neq 0$

We derived new expressions for ρ for combination 7 (all effects present simultaneously) and for combinations 1, 2 and 4 (each effect acting independently). The expressions for the other combinations were obtained by inference. As stated earlier, we will present only the results of the derivations.

It is convenient to first present the results obtained for combination 7, since all other results can be obtained by simple elimination of parameters and/or by substitution of degenerate forms for the equations defining parameters in the expressions for ρ . It should be remembered that ρ generally assumes different forms for $D = 0$ (the one used to compute false

detection probability) and for $D \neq 0$ (the one used to compute the detection probability).

5.2.1 Results for Combination 7

For this combination we find that the coefficient of spectral correlation between ΔN and $\tau'\alpha'$ is

$$\rho = \frac{\bar{\beta} + \frac{1}{z} \frac{1}{M} \sum_{i=1}^M x_i}{\left[\frac{1}{M} \sum_{i=1}^M \left(1 + \frac{1}{z} x_i \right)^2 \right]^{1/2}}, \quad (10)$$

where the x_i are independent unit normal random numbers, M is the number of resolved spectral elements comprising ΔN and $\tau'\alpha'$, and where

$$\bar{\beta} = \frac{\sigma_{01} + \sigma_{1\xi}}{\sigma_1 \left[\sigma_0^2 + 2\sigma_{0\xi} + \sigma_\xi^2 \right]^{1/2}}, \quad (11)$$

$$z = D \left[\sigma_0^2 + 2\sigma_{0\xi} + \sigma_\xi^2 \right]^{1/2} / (\sqrt{2} \overline{NESR}) \quad (12)$$

$$\sigma_0^2 = \langle (\tau\beta - \mu)^2 \rangle = \text{variance of } \tau\beta \text{ (actual } \tau\alpha\text{-type spectrum)} \quad (13)$$

$$\sigma_1^2 = \langle (\tau'\alpha' - \mu')^2 \rangle = \text{variance of } \tau'\alpha' \text{ (reference } \tau\alpha \text{ spectrum)} \quad (14)$$

$$\sigma_\xi^2 = \langle (\xi/D - \mu_\xi)^2 \rangle = \text{variance of } \xi/D \text{ (normalized spectrum error in background subtraction)} \quad (15)$$

$$\sigma_{01} = \langle (\tau\beta - \mu)(\tau'\alpha' - \mu') \rangle = \text{covariance of } \tau\beta \text{ and } \tau'\alpha' \quad (16)$$

$$\sigma_{0\xi} = \langle (\tau\beta - \mu)(\xi/D - \mu_\xi) \rangle = \text{covariance of } \tau\beta \text{ and } \xi/D \quad (17)$$

$$\sigma_{1\xi} = \langle (\tau'\alpha' - \mu')(\xi/D - \mu_\xi) \rangle = \text{covariance of } \tau'\alpha' \text{ and } \xi/D. \quad (18)$$

For $D \neq 0$, β is defined by

$$\beta = \alpha + (D_1/D)\alpha_1 + (D_2/D)\alpha_2 + \dots \quad (19)$$

while for " $D = 0$ "

$$\beta = (D_1/D)\alpha_1 + (D_2/D)\alpha_2 + \dots ; D \equiv \text{any value} \quad (19a)$$

In the case $D = 0$, which is used to obtain the false detection probability, ρ (and also $\bar{\rho}$ and z) are independent of D (see Eqs. 10-12, 15, 17, 18, 19a). Thus, any value of D may be used in Eqs. 12, 15, 17, 18 and 19a.

In the definitions (13)-(18), the symbols μ , μ' and μ_ξ denote the means of the spectral quantities included in the same set of parentheses. In particular, μ is the mean of $\tau\beta$, and, hence, it assumes different values for the cases $D \neq 0$ and " $D = 0$ ".

The parameter $\bar{\rho}$, like ρ , has the form of a coefficient of correlation. In fact, we see from Eq. (10) that it is the value assumed by ρ when there is no system noise (all $x_i = 0$). Likewise, we will find that $\bar{\rho} = 1$ when effects a , b and c are absent.

It is convenient to consider next the combinations 6, 3 and 2, which, like 7, have target species overlap as one of the interference effects.

5.2.2 Results for Combination 6

This combination is the same as 7 except that $c = 0$. That is, $\xi = 0$, and hence any variances or covariances with subscript ξ are equal to zero. Specifically, Eqs. (11) and (12) reduce to

$$\bar{\rho} = \sigma_{01}/(\sigma_1\sigma_0) \quad (11a)$$

$$z = D\sigma_0/(\sqrt{2} \text{ NESR}) \quad (12a)$$

σ_0^2 , σ_1^2 and σ_{01} are defined by Eqs. (13), (14) and (16). Equations (19) and (20) are still applicable.

5.2.3 Results for Combination 3

This combination is the same as 7 except $a = 0$. That is, $\tau'\alpha' \rightarrow \tau\alpha$ in Eqs. (14), (16) and (18). The other equations are unchanged.

5.2.4 Results for Combination 2

Combination 2 is the same as 6 except $a = 0$. That is, Eqs. (11) and (12) reduce to (11a) and (12a), and $\tau'\alpha' \rightarrow \tau\alpha$ in Eqs. (14), (16) and (18).

We next consider combinations 5 and 1, which are distinguished by the property $c = 1$ and $b = 0$ (different atmospheric and/or background radiances in the two IFOV's, but no spectral interferences among target species). Note that when a particular detection band contains no overlapping target species (or when overlapping species are not expected to occur simultaneously), the only combinations of interest are 5, 1, 4 and 0.

5.2.5 Results for Combination 5

Since there are no spectral interferences, $\alpha_1 = \alpha_2 = \dots = 0$, and therefore Eq. (19) gives $\beta = \alpha$ for $D \neq 0$ and $\beta = 0$ for $D = 0$. Alternately, we may write the entire set of equations in the form

$$\rho = \frac{\beta + \frac{1}{Z} \frac{1}{M} \sum_{i=1}^M x_i}{\left[\frac{1}{M} \sum_{i=1}^M \left(1 + \frac{1}{Z} x_i \right)^2 \right]^{\frac{1}{2}}}, \quad (20) \quad (\text{same as 10})$$

where, if $D \neq 0$

$$\rho = \frac{\sigma_{01} + \sigma_{1\xi}}{\sigma_1 \left[\sigma_0^2 + 2\sigma_{0\xi} + \sigma_\xi^2 \right]^{1/2}}, \quad (21) \quad (\text{same as 11})$$

$$z = D \left[\sigma_0^2 + 2\sigma_{0\xi} + \sigma_\xi^2 \right]^{1/2} / (\sqrt{2} \text{ NESR}) . \quad (22) \quad (\text{same as 12})$$

But for $D = 0$,

$$\rho = \sigma_{1\xi} / (\sigma_1 \sigma_\xi) \quad (23)$$

$$z = \sigma_\xi D / (\sqrt{2} \text{ NESR}) \quad (24)$$

where in Eqs. (23) and (24), D can have any value. The variances/covariances in Eqs. (20) through (24) are given by

$$\sigma_0^2 = \langle (\tau\alpha - \mu)^2 \rangle = \text{variance of } \tau\alpha \quad (25)$$

$$\sigma_1^2 = \langle (\tau'\alpha' - \mu')^2 \rangle \quad (26) \quad (\text{same as 14})$$

$$\sigma_\xi^2 = \langle (\xi/D - \mu_\xi)^2 \rangle \quad (27) \quad (\text{same as 15})$$

$$\sigma_{01} = \langle (\tau\alpha - \mu)(\tau'\alpha' - \mu') \rangle = \text{covariance of } \tau\alpha \text{ and } \tau'\alpha' \quad (28)$$

$$\sigma_{0\xi} = \langle (\tau\alpha - \mu)(\xi/D - \mu_\xi) \rangle = \text{covariance of } \tau\alpha \text{ and } \xi/D \quad (29)$$

$$\sigma_{1\xi} = \langle (\tau'\alpha' - \mu')(\xi/D - \mu_\xi) \rangle \quad (30) \quad (\text{same as 18})$$

Next, we will consider combinations 4 and 1. In these combinations both b and c are zero, which results in a degeneration of the equation that gives ρ when $D = 0$.

5.2.6 Results for Combination 4

When $D = 0$, we find that

$$\rho = \frac{\frac{1}{M^{\frac{1}{2}}} \sum_{i=1}^M x_i}{\left[\frac{1}{M^{\frac{1}{2}}} \sum_{i=1}^M x_i^2 \right]^{\frac{1}{2}}} \quad (31)$$

For $D \neq 0$, Eq. (20) or (10) is applicable. Combination 4 is the same as 5 except $c = 0$ ($\xi = 0$); hence, from Eqs. (21) and (22), we obtain

$$\bar{\rho} = \sigma_{01} / (\sigma_0 \sigma_1) \quad (32)$$

$$z = \sigma_0 D / (\sqrt{2} \text{ NESR}) \quad (33)$$

as the parameters to use in Eq. (20). σ_0^2 , σ_1^2 and σ_{01} are given by Eqs. (25), (26) and (28).

5.2.7 Results for Combination 1

This combination is the same as 5 except that $a = 0$. That is, $\tau' \alpha' \rightarrow \tau \alpha$ in Eqs. (26), (28) and (30). With this substitution σ_0^2 , σ_1^2 and σ_{01} become identical, as do $\sigma_{0\xi}$ and $\sigma_{1\xi}$. Thus, Eqs. (21) and (22) can be written

$$\bar{\rho} = \frac{\sigma_0^2 + \sigma_{0\xi}}{\sigma_0 \left[\sigma_0^2 + 2\sigma_{0\xi} + \sigma_{\xi}^2 \right]^{\frac{1}{2}}} \quad (34)$$

$$z = D \left[\sigma_0^2 + 2\sigma_{0\xi} + \sigma_{\xi}^2 \right]^{\frac{1}{2}} / (\sqrt{2} \text{ NESR}) \quad (35) \quad (\text{same as 22}),$$

which apply when $D \neq 0$. Equations (23) and (24) are applicable when $D = 0$,

except that $\sigma_{1\xi} \rightarrow \sigma_{0\xi}$ and $\sigma_1 \rightarrow \sigma_0$:

$$\bar{\rho} = \sigma_{0\xi} / (\sigma_0 \sigma_\xi) \quad (36)$$

$$z = \sigma_\xi D / (\sqrt{2} \text{ NESR}) \quad (37)$$

5.2.8 Results for Combination 0

This combination is the same as 4 except that $a = 0$. That is, $\tau'\alpha' \rightarrow \tau\alpha$ in Eqs. (26), (28) and (30). Then $\sigma_0^2 = \sigma_{01} = \sigma_1^2$, and Eqs. (32) and (33) reduce to

$$\bar{\rho} = 1 \quad (38)$$

$$z = \sigma_0 D / (\sqrt{2} \text{ NESR}) . \quad (39)$$

Equations (38), (39) and (20) define ρ for $D \neq 0$. For $D = 0$, ρ is given by Eq. (31). These are exactly the results obtained in Section 2 for the case $a = b = c = 0$ (note that $\sigma_0 = \sigma_1$ was previously denoted by σ').

5.3 General Influence of Real-World Effects in ρ , in the Detection/False Detection Probabilities, and in the Minimum Detectable Quantities

To understand how the "real world" effects influence the MDQ's, we must first consider how the probability density function (pdf) of the absolute correlation coefficient $|\rho|$ behaves with detector noise and with the types of interference described above. We are able to describe this behavior in general terms with the aid of hindsight gained from realistic experiments on the computer, and to show that one of the real-world effects will essentially eliminate any possibility of detecting some of the species of interest, unless the detection scheme described in Section 2 is modified. However, the required modification is very simple and appears to be quite

effective; that is, it results in only a slightly increased MDQ for the several species considered. Section 5.4 describes the modified detection procedure, and Section 5.6 presents some revised MDQ's for a worst-case situation. Section 5.5 describes the interference model used to compute the revised MDQ's.

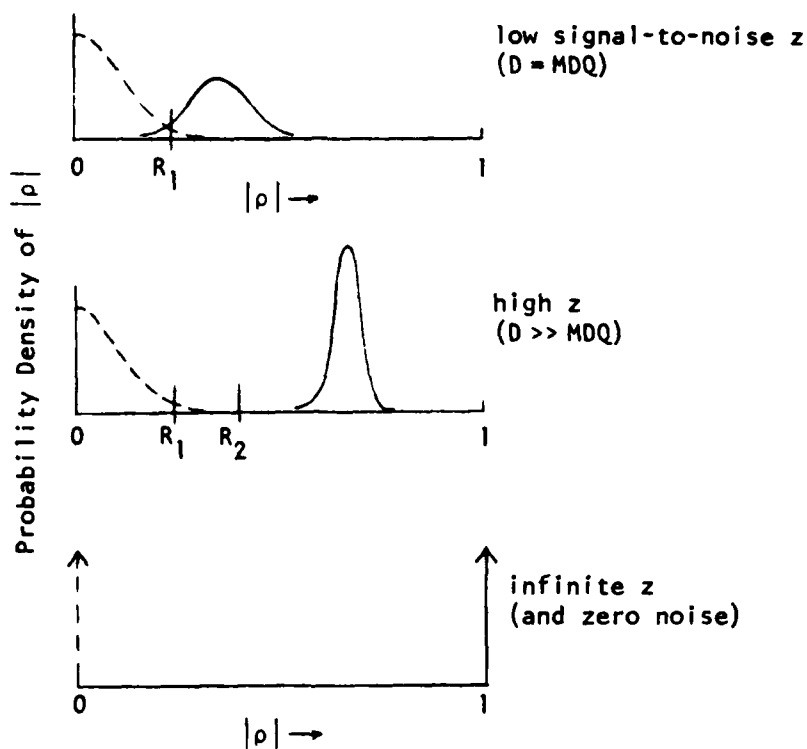


Figure 5.1 Pdf's of $|\rho|$ for the Ideal Case

Figure 5.1 shows how the pdf of $|\rho|$ behaves with signal-to-noise z in the case when detector noise is the only interference (the "ideal case", or case 0, which was treated in Section 2; the detection signal-to-noise z was denoted Z in that section). The dashed curve in the first part of the figure is the pdf when no gas is present ($D=0$), and the solid curve is the pdf when $D \neq 0$. Note that this is a schematic representation; the solid curve will generally not be symmetrical about its modal value. The area under each curve is unity. The area under the solid curve at $|\rho|$ greater than some threshold R_1 is the detection probability, while the area under

the dashed curve at $|\rho| > R_1$ is the false detection probability. The first part of the figure corresponds to low signal-to-noise z or to $D =$ the MDQ. For example, if $M = 1000$ resolution elements, a z -value of 0.13 gives detection/false detection probabilities of approximately 0.95 and 0.01, respectively, when the threshold R_1 is 0.075. Generally, as z is increased the solid curve moves towards higher $|\rho|$, and becomes narrower (of course, it maintains unit area). The dashed curve, however, is unchanged since it is independent of z [see Eq. (31)]. For high z -values we can choose a threshold R_2 that gives essentially unity detection probability and zero false detection probability. For infinite z the solid curve becomes a unit delta function at $|\rho| = 1$. If the detector noise is zero the dashed curve becomes a delta function at $|\rho| = 0$.

Figure 5.2 compares the pdf's for the ideal and non-ideal cases, where "non-ideal" means that one or more of the real-world effects can be present. In general, in the non-ideal case, the pdf for $D = 0$ (the dashed curve) and the pdf for $D \neq 0$ (the solid curve) are associated with different z -values and with different values of the parameter $\tilde{\rho}$. (We recall that $\tilde{\rho}$ is the value of the correlation coefficient when there is no detector noise; it is unity in the ideal case when $D \neq 0$). The position of the maximum in the dashed curve depends on both z and $\tilde{\rho}$, as does the "width" of the curve; the same is true of the solid curve. Part (b) of Fig. 5.2 is an example of the appearance of the pdf of $|\rho|$ for the non-ideal case. Note that both the dashed and solid curves (in this example) are shifted towards higher $|\rho|$ and are narrower relative to those for the ideal case. The shift occurs when the interferences in the spectrum have "accidental" correlation with the reference ($\tau'\alpha'$) spectrum. The narrowing of the curves occurs when the

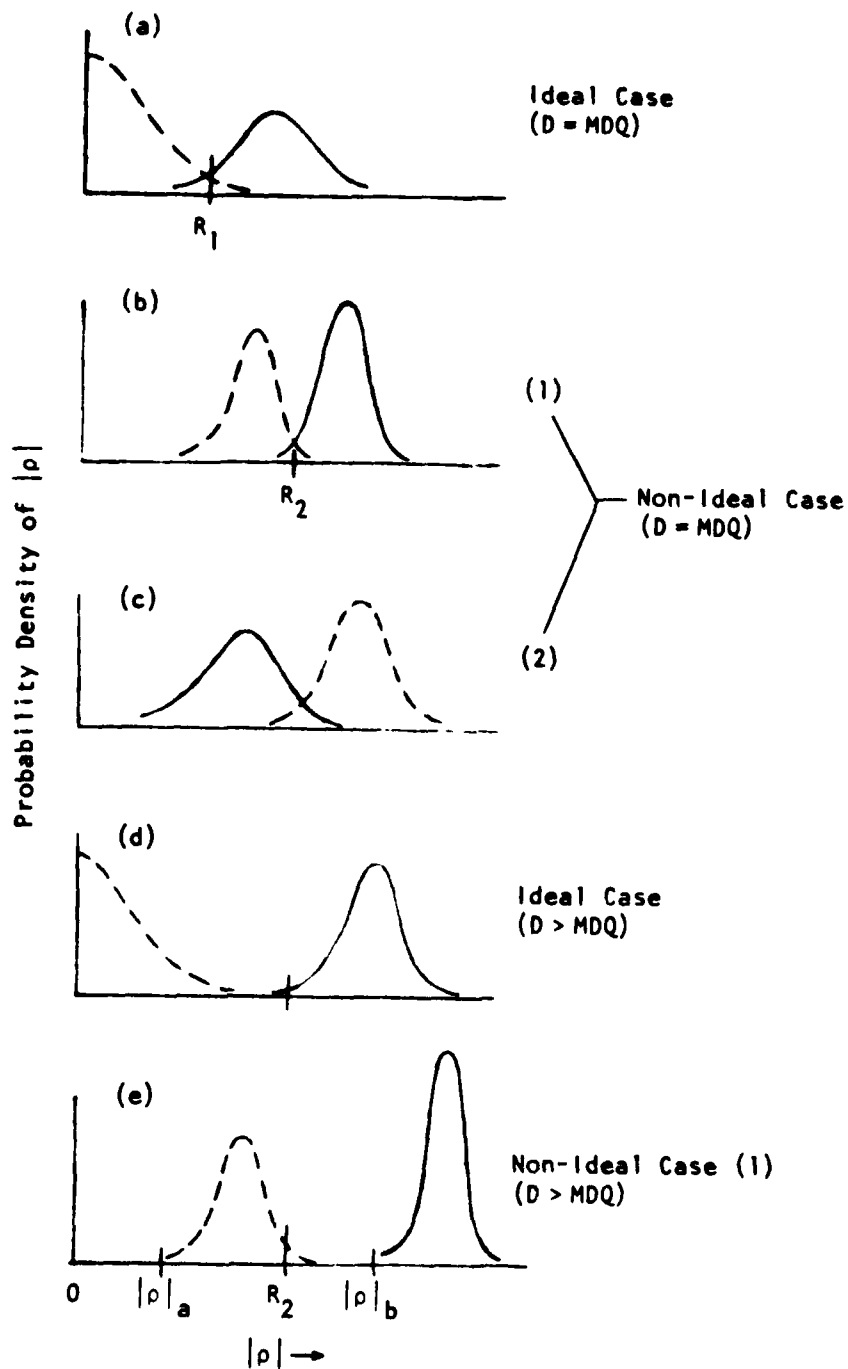


Figure 5.2 Pdf's of $|\rho|$; Ideal vs. Non-Ideal Case

interference increases the radiance observed in spectral resolution elements where the gas of interest emits (or increases the absorption when the gas of interest is observed in absorption); i.e., when the effective "signal-to-noise" is increased. However, the situation depicted in part (c) of Fig. 5.2 can also occur. Here the maximum of the dashed curve corresponds to larger $|\rho|$ than the maximum of the solid curve, which means that the presence of the gas of interest tends to decrease the value of the correlation coefficient.

Assume for the moment that part (b) of Fig. 5.2 is the only type of non-ideal situation that can exist. In this situation it is sometimes possible to choose a new threshold R_2 that gives detection/false detection probabilities on the order of 0.95/0.01 even for D equal to the MDQ of the ideal case. However, in order to achieve a 0.95 detection probability in the ideal case using this new threshold, D would obviously have to be larger than the original MDQ; that is, the pdf of $|\rho|$ would have to look like part (d) of Fig. 5.2. For this value of D the pdf of $|\rho|$ for the non-ideal case would look like part (e) rather than part (b) of the figure. The new value of D would be the new MDQ and R_2 would be the new required threshold on $|\rho|$.

The pdf's shown in parts (b) and (e) of Fig. 5.2 (and also part (c)) are the type that one encounters in modelling a particular or perhaps worst-case non-ideal situation. In practice, the interference can range in magnitude from zero (the ideal case) to the worst case situation, according to some other probability density function. The effect in part (b) is to broaden the two curves and shift the maxima towards smaller $|\rho|$. The same effect occurs in part (e), which tends to place more of the pdf areas in the vacant regions $(0, |\rho|_a)$ and $(R_2, |\rho|_b)$; however, the threshold R_2 will still result in adequate detection probability and adequate false target rejection.

Unfortunately, the two non-ideal situations depicted in parts (b) and (c) of Fig. 5.2 can occur with roughly equal (50 percent) probabilities for the type of interference represented by different atmospheric/background properties in the two detection IFOV's. This means that the best performance that can be achieved is roughly 50 percent detection probability and 50 percent false detection probability, which, of course, is an unacceptable level of performance.

5.4 Modified Detection Procedure

We will first illustrate how the different situations displayed in parts (b) and (c) of Fig. 5.2 can occur when the two IFOV's contain different amounts of water vapor, and then show how a simple modification of the correlation detection process can all but eliminate the effects of this type of interference.

Suppose that IFOV1 contains more H_2O than IFOV2 (we recall that IFOV2 contains the target gas). All of the selected detection bands are located in either the 3-5 μm region or the 8-13 μm region, where atmospheric H_2O has weak continuum absorption. Under normal conditions the tropospheric temperature lapse rate is positive (temperature decreases with altitude) and, hence, the H_2O acts as a net absorber rather than as an emitter. Consequently, the observed continuum radiance level will decrease as the H_2O column thickness in the IFOV is increased. The observed spectral radiances for the two IFOV's will look more or less as indicated in Fig. 5.3a, assuming the target gas is observed in emission (is hotter than the surface).

The detection bands will usually contain some strong atmospheric spectral lines, usually due to H_2O . In lines that are extremely strong ("opaque") the observed spectral radiance will be very small for both IFOV's, as

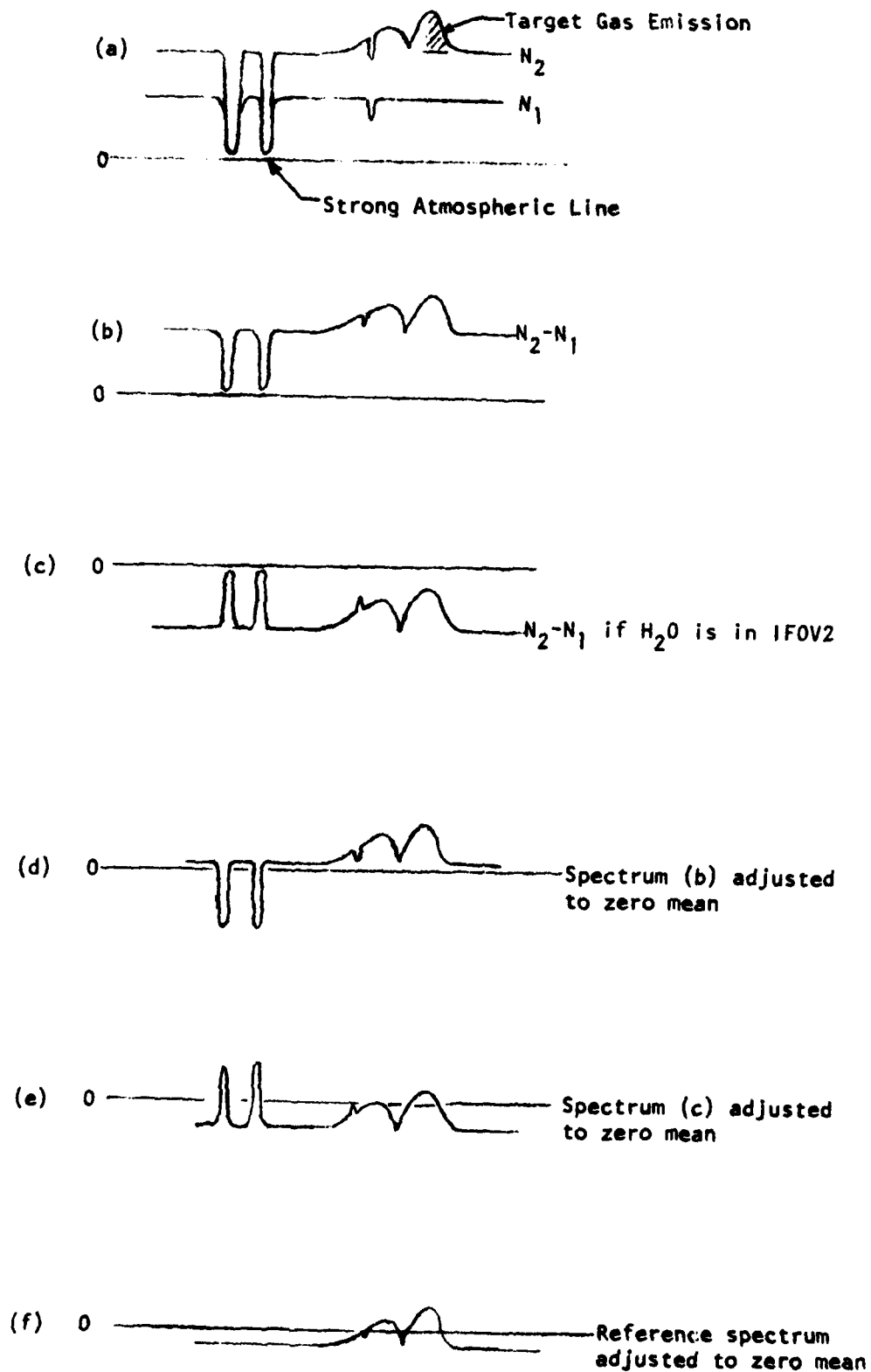


Figure 5.3 Effects of Strong Atmospheric Lines on the Mean of the Contrast Spectral Radiance

Indicated in Fig. 5.3a. The contrast spectral radiance $N_2 - N_1$ will resemble part (b) of Fig. 5.3. Clearly, if the excess H_2O is transferred from IFOV1 to IFOV2, the contrast spectrum would have the appearance of part (c) of the figure. What we wish to demonstrate is that parts (b) and (c) are the respective counterparts of the pdf's represented in parts (b) and (c) of Fig. 5.2.

We note that contrast spectrum 5.3b has a positive mean, and spectrum 5.3c has a negative mean. The two spectra adjusted to zero mean (an operation prescribed by the spectral correlation process) would look like Figs. 5.3d and 5.3e, respectively. The zero-mean spectra, of course, would be identical if the contributions of strong atmospheric lines were absent. In the correlation processing spectrum (d) or (e) is correlated with the zero-mean reference spectrum pictured in Fig. 5.3f. Generally (d) and (f) will have imperfect but high correlation while (e) and (f) will have imperfect but relatively low correlation. Low correlation is obtained in the latter case because small and/or negative values of apparent target spectral radiance coincide with high spectral radiance values in the reference spectrum (Multiplying the zero-mean contrast radiance by -1 would have no effect since we test on the absolute value of ρ ; it is necessary to test on $|\rho|$ because the target can be observed in either emission or absorption). We see that the correlation would actually be greater if IFOV2 contained no target gas. This results in the pdf's shown in part (c) of Fig. 5.2. When the IFOV containing the emitting target has less H_2O than the other IFOV the resulting pdf's look like Fig. 5.2a. Note that correlation coefficients higher than those of the ideal case can be obtained merely because the interference results in higher correlation signal-to-noise z .

An obvious solution to this dilemma is to exclude from the correlation process any spectral elements containing very strong atmospheric absorption lines. That is, we should assign zero values to their observed radiances and reduce the total number of spectral elements M in proportion to the number of assigned zeros. Note that the reference spectrum $\tau'\alpha'$ is effectively zero in the regions of opaque lines; hence, the real effect of modifying the correlation procedure is to prevent strong atmospheric lines from affecting the means of the observed radiance spectra for the two IFOV's. Clearly, the correlation processing must include subtraction of the mean spectral radiance: otherwise, the correlation would be reduced by different H_2O continuum levels and/or different surface temperatures in the two IFOV's.

5.5 Interference Model Used to Estimate Revised MDQ's

The sources of the target gas emissions are not likely to emit, simultaneously, species that have overlapping detection bands, at least for the 15 species considered. That is, interference type "b" need not be considered. In modelling the effects of interference type "c", we assumed that the only differences between the atmospheres/backgrounds observed by the two IFOV's are the H_2O column thicknesses and/or the background temperatures. In modelling interference type "a", we assumed that the estimated reference spectrum $\tau'\alpha'$ corresponds to an incorrect estimate of the H_2O column thickness; i.e., that $\alpha' = \alpha$, but $\tau' \neq \tau$ only because of the wrong H_2O column thickness.

One would not expect interference type "a" to degrade system performance nearly as much as type "b", since the latter can introduce lines in the contrast radiance spectrum whose positions are random with respect to the target gas lines. Also, the effect of different surface temperatures in the two IFOV's can be greatly reduced for many of the detection bands by

"pre-whitening" the observed contrast radiance spectrum; that is, by removing any slope or curvature in its envelope. Thus, in the modelling of interference effects this study emphasizes the case of different H_2O amounts in the two IFOV's. Spectral variations in earth background emissivity were not considered, because they probably have only low resolution features that can also be eliminated by pre-whitening.

We do not know of any data on H_2O vertical column thickness variations over horizontal distances of the order of 10 meters. However, a reasonable estimate of the maximum variation can be obtained by considering the mechanisms involved in the formation of fair weather cumulus clouds (this point of view was suggested to us by Dr. J. Bunting of AFGL). Generally, these low clouds are formed when ground level moisture rises and cools to the point where saturation occurs. A reasonable model for the vertical H_2O density profile (or dew point temperature profile) under the cloud is therefore obtained by assuming constant dew-point temperature from ground level up to the altitude where the actual temperature has lapsed to this value. For the LOWTRAN Midlatitude Summer, Subarctic Summer and Tropical model atmospheres, we find that this altitude is very close to one kilometer, which is the height usually observed for low cumulus cloud bases in these types of climate (they can be somewhat higher for extremely dry climates).

The assumption is made that the maximum difference in total H_2O in the two detection IFOV's is equal to the excess H_2O below the cumulus cloud, as defined by the above argument. That is, we assume that the worst case condition is when a cloud is about to be formed at one km in one of the IFOV's. The calculation of the H_2O difference, using LOWTRAN model atmospheres, is then quite simple: we merely determine the H_2O amount in the 0-1 km layer

assuming the LOWTRAN H₂O density varies linearly between 0 and 1 km, and subtract this from the amount obtained assuming the density is equal to the ground level value between 0 and 1 km. By this procedure we find that the differences are

- 0.15 pr cm for the Subarctic Summer model
(which has a total of 2.1 pr cm)
- 0.20 pr cm for the Midlatitude Summer model
(which has a total of 3.0 pr cm)
- 0.30 pr cm for the Tropical model
(which has a total of 4.2 pr cm)

In each case the difference is approximately seven percent of the total column thickness. In modelling the effects of the difference we used the Midlatitude Summer model and a difference of 0.2 pr cm. One calculation was made of the effects of simultaneous interferences "a" and "c"; in this case the "estimated" spectral transmittance represented an error in estimated H₂O amount equal to 0.4 pr cm.

5.6 Some Revised MDQ's

We examined the effects of the interferences for the preferred SO₂, HCl and HBr detection bands. We picked the SO₂ and HCl bands because their MDQ's are more strongly affected by H₂O variations and/or nadir view angle than the other bands, provided we exclude CH₄, which is only marginally detectable (see Table 4.2, Section 4). Also, SO₂ and HCl are different in that the former has significant overlap between its lines, while the latter has very widely separated lines. We selected HBr as the third band because it contains very little H₂O absorption.

Interference effects in SO₂ detection were partially evaluated for the original method of data processing, but a revised MDQ value was computed only for the revised method, which masks out strong atmospheric lines. For the

other two molecules we evaluated only the revised method. The revised method was implemented using the following simplified procedure: we first examined the previously mentioned spectral transmittance plots for the Midlatitude Summer model (see Section 1 and Vol. II), and determined the average value of the spectral transmittance envelope. We then selected a somewhat lower transmittance value to use as a threshold in the correlation processing. That is, spectral elements having predicted transmittances less than the threshold value were excluded when we evaluated the spectrum variances and covariances that determine the correlation coefficient ρ . For example, the ν_1 band of SO_2 has a spectral transmittance envelope equal to approximately 0.58; the selected transmittance threshold is 0.4. An examination of the spectral transmittance plot for this band shows this threshold will eliminate the effects of a large number of the atmospheric absorption lines, except perhaps in the far wings of the strongest lines.

5.6.1 The ν_1 Band of SO_2

We first computed the normalized contrast spectral radiance $\tau\alpha + \xi/D$ without spectral masking to demonstrate that strong H_2O lines have large contributions to the contrast. Figure 5.4a shows the normalized spectral contrast when IF0V2 contains SO_2 in the quantity 2.66×10^{11} (molec/ cm^2)(W/ $\text{cm}^2 \text{ sr cm}^{-1}$), which is equal to the MDQ for a dwell time of 10 seconds, and IF0V1 contains 0.2 pr cm more H_2O than IF0V2. Figure 5.4b is the normalized reference contrast spectrum $\tau\alpha = \tau'\alpha'$ plotted to the same scale as Fig. 5.4a. In the original method of data processing, detection of SO_2 would be based on the correlation of parts (a) and (b) of the figure. Note that the normalized spectral contrast $\tau\alpha + \xi/D$ will tend to be independent of D at frequencies where SO_2 is the only emitter, and varies as $1/D$ where H_2O

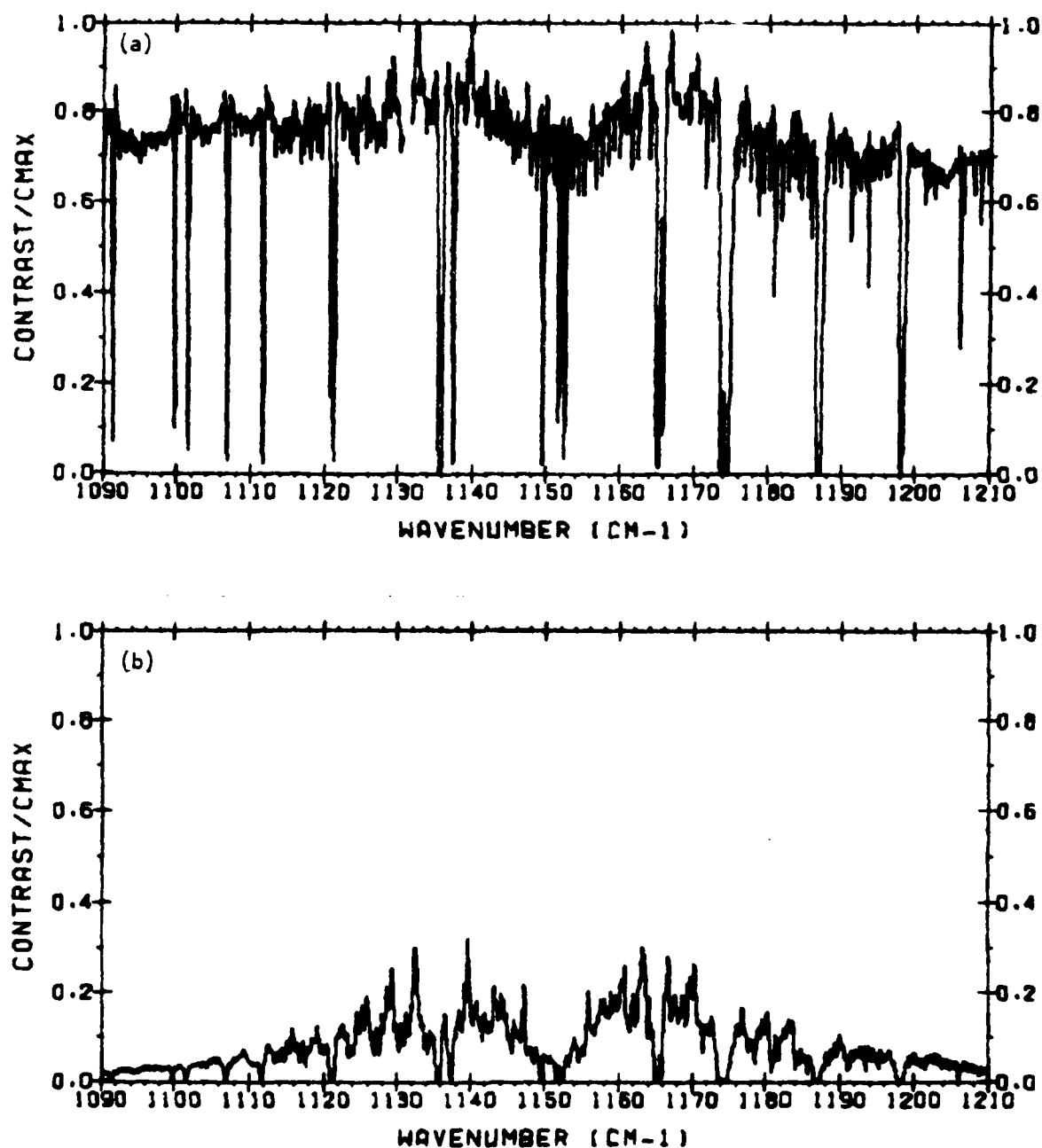


Figure 5.4 Part (a): Normalized contrast spectral radiance $\tau + \xi/D$ for the ν_1 band of SO_2 for $D = 2.66 \times 10^{11}$ (molec/cm²) ($\text{W/cm}^2 \text{ sr cm}^{-1}$). IFOV1 contains 0.2 pr cm more H_2O than IFOV2.

Part (b): The normalized spectral contrast τ plotted to the same scale as part (a).

or some other non-target species is the only emitter. However, on the normalized "zero-to-one" scales of the figures, the SO_2 features would tend to become more prominent as D increases. Note, also, that the H_2O lines in the SO_2 detection band have a significant effect on the mean value of the normalized spectral radiance (when D equals the MDQ for $t_d = 10$ seconds).

Figures 5.5a and 5.5b show the corresponding results when the excess 0.2 pr cm H_2O is in IF0V2 rather than IF0V1. Now, the actual spectral contrast is negative at all frequencies (the horizontal lines denote zero contrast; again, the scales are identical). It may be noted that the reference spectrum is somewhat smaller than for the case shown in Fig. 5.4. This is because the predicted reference spectrum is assumed to have no error ($\tau'\alpha' = \tau\alpha$), and because τ is now smaller as a result of the increased H_2O above the SO_2 in IF0V2.

The computed parameters that determine the statistics of $|\rho|$ for the two cases are:

	FIGURE 5.4 ($\Delta w = 0.2$ in IF0V1)	FIGURE 5.5 ($\Delta w = 0.2$ in IF0V2)
M	1200	1200
$\tilde{\rho}(D \neq 0)$	0.573	0.110
$z \cdot \overline{\text{NESR}}(D \neq 0)$	5.02×10^{-9}	4.14×10^{-9}
$\tilde{\rho}(D = 0)$	0.273	-0.273
$z \cdot \overline{\text{NESR}}(D = 0)$	4.28×10^{-9}	4.28×10^{-9}

We note that the presence of SO_2 tends to increase $|\tilde{\rho}|$ (and, hence $|\rho|$) as well as the correlation signal-to-noise z in the first case, while it has the opposite effect in the second case. If we were to use the above

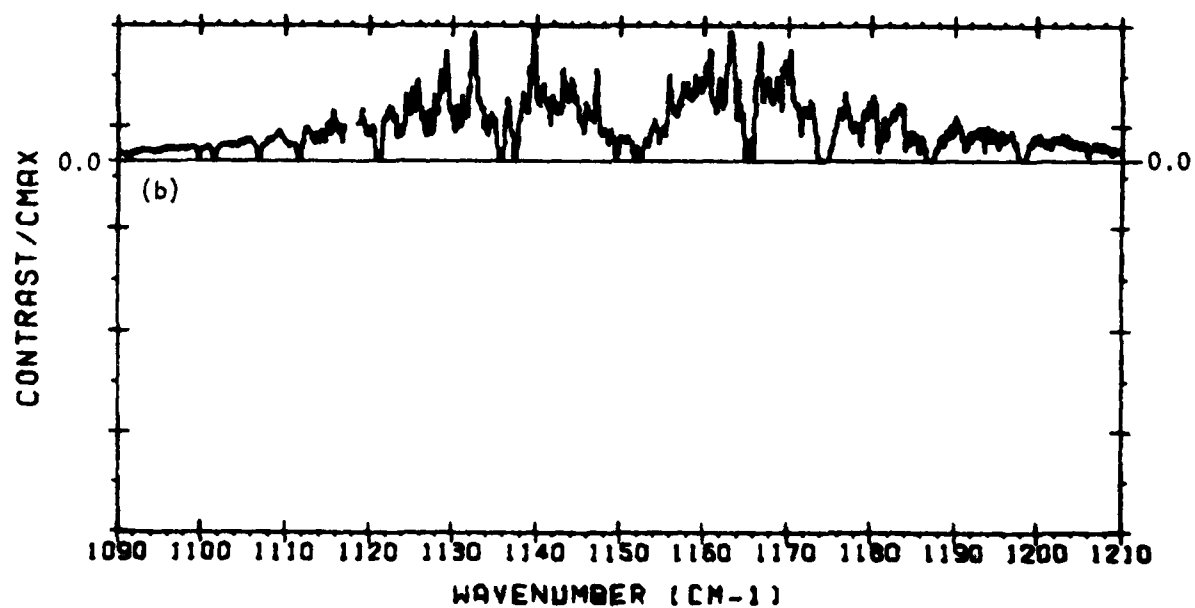
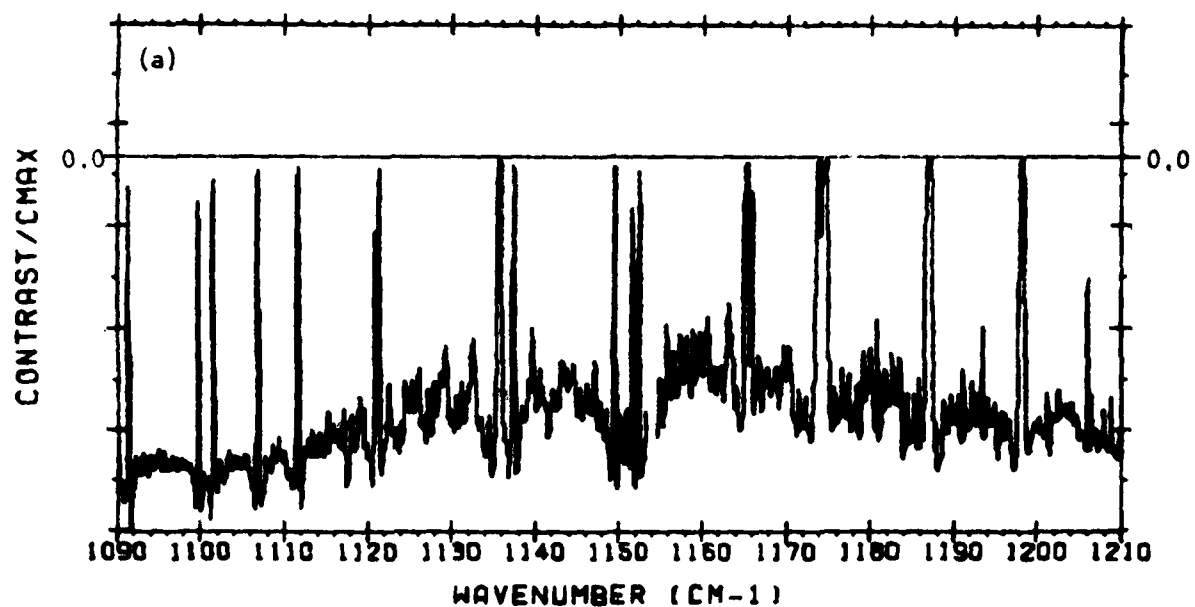


Figure 5.5 Same as Fig. 5.4, except that IFOV2 contains 0.2 pr cm more H_2O than IFOV1.

parameters to compute the pdf's of $|\rho|$, we would find that they resemble Figs. 5.2b and 5.2c, respectively.

Figures 5.6 and 5.7 show the result, in the contrast spectrum, of "masking out" spectral elements with transmittances less than the threshold transmittance value, 0.4. In these figures the excluded spectral elements have been assigned a contrast value equal to the mean contrast of the remaining elements (in the correlation processing they are simply excluded). Figure 5.6 represents the case of 0.2 pr cm excess H_2O in IFOV1; the number of elements remaining after applying the exclusion criterion is 926 compared to the original 1200. Figure 5.7 represents the case of 0.2 pr cm excess H_2O in IFOV2; the new M is 870. In the revised correlation procedure, the 926 surviving elements of Fig. 5.6 are correlated with corresponding elements of Fig. 5.4b; similarly, the 870 elements of Fig. 5.6 are correlated with those of Fig. 5.5b. Computations of $\tilde{\rho}$, z and the resulting detection/false detection probabilities yielded the following values:

	FIGURE 5.6 ($\Delta w = 0.2$ in IFOV1)	FIGURE 5.7 ($\Delta w = 0.2$ in IFOV2)
Threshold on τ	0.4	0.4
new M	927	871
$\tilde{\rho}(D \neq 0)$	0.731	0.857
$z \cdot \overline{NESR}(D \neq 0)$	1.81×10^{-9}	2.33×10^{-9}
(D = 2.66×10^{11} ; Z = 0.124 for 10 second dwell)		
$\tilde{\rho}(D = 0)$	-0.288	0.294
$z \cdot \overline{NESR}(D = 0)$	1.29×10^{-9}	1.26×10^{-9}
$P(T T)$ } for	~ 0.66	~ 0.97
$P(T O)$ } threshold 0.075	~ 0.05	~ 0.07
$P(T T)$ } for	~ 0.60	~ 0.95
$P(T O)$ } threshold 0.08	~ 0.035	~ 0.055

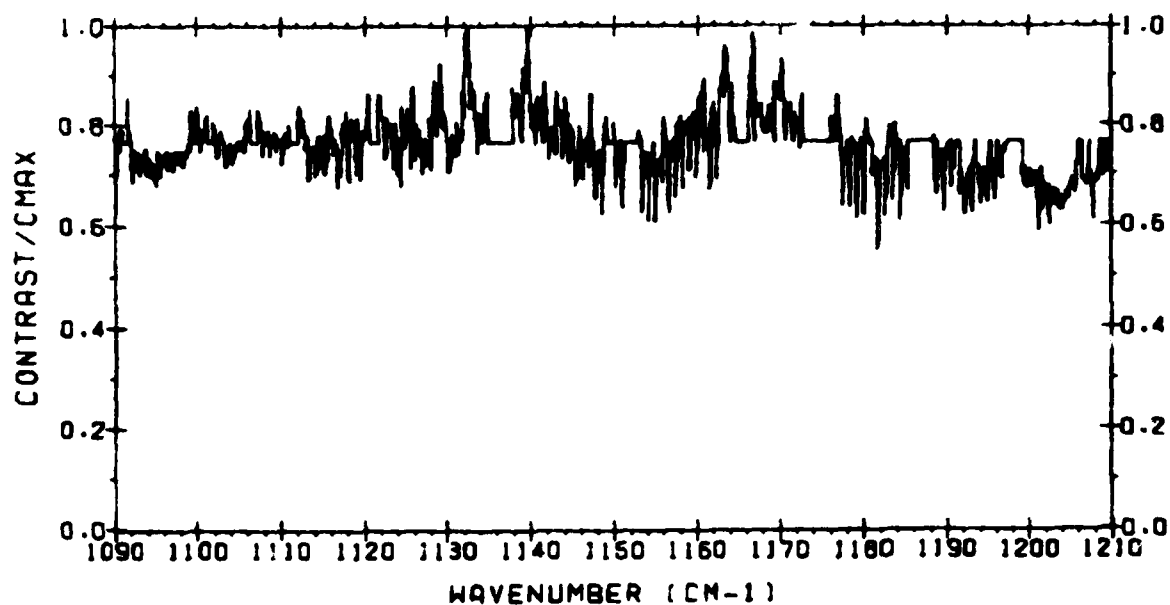


Figure 5.6 Same as Fig. 5.4a, except that spectral elements corresponding to $\tau < 0.4$ have been assigned a contrast value equal to the mean contrast of the remaining elements.

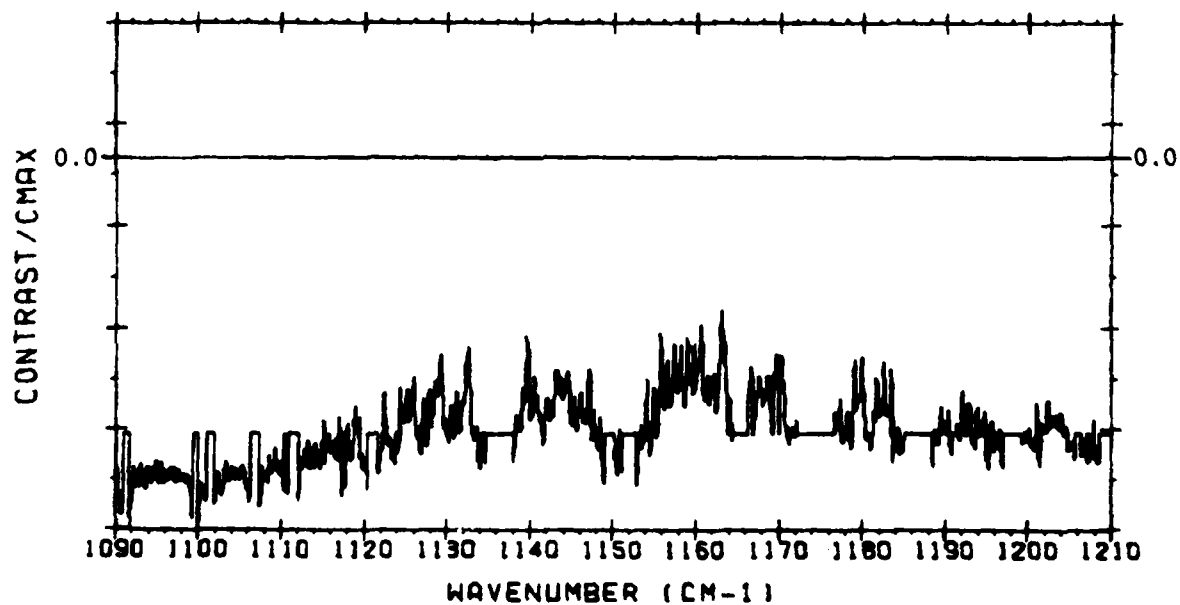


Figure 5.7 Same as Fig. 5.5a, except that spectral elements corresponding to $\tau < 0.4$ have been assigned a contrast value equal to the mean contrast of the remaining elements.

For the ideal case (no interferences) the MDQ corresponded to $Z = 0.124$ and $R = 0.075$, which resulted in detection and false detection probabilities of 0.94 and 0.01, respectively. Thus, it is interesting that only slightly degraded performance is obtained in the non-ideal case when the excess H_2O and the emitting target SO_2 occupy the same IFOV, while very poor performance is obtained when they occupy different IFOV's (e.g., 0.95/0.055 versus 0.66/0.05). It is interesting because it is really the former situation that led us to include spectral masking in the correlation processing. The explanation of these results is that weak atmospheric absorption lines become important after the effects of the strong lines have been eliminated. That is, weak atmospheric lines within the SO_2 band tend to add to the SO_2 lines if the SO_2 is observed in emission and the excess H_2O is in IFOV2 (see Fig. 5.3c), while they tend to attenuate the SO_2 lines if the excess H_2O is in the other IFOV (see Fig. 5.3b). In fact, the opposite of this "interesting" outcome would obtain if the SO_2 band is observed in absorption. In any case, it is evident that the SO_2 amount (MDQ) must be increased to ensure that adequate performance is obtained in all possible situations.

We recalculated the detection parameters for the "Figure 5.6 case" with D increased by the factor 1.5. All results were the same, except $\bar{p}(D \neq 0)$ which increased to 0.869, and $z \cdot \overline{NESR}(D \neq 0)$ which increased to 2.49×10^{-9} ; the corresponding $P(T|T)$ vs. $P(T|0)$ tradeoff improved, as indicated by the following set of values:

<u>R(threshold on ρ)</u>	<u>P(T T)</u>	<u>P(T 0)</u>
0.075	~0.99	~0.05
0.08	~0.985	~0.035
0.1	~0.92	~0.005

These values suggest that the MDQ for the non-ideal case is approximately 1.5 times that for the ideal case.

We also recalculated the detection parameters for the "Figure 5.6 case" with the additional assumption that the predicted $\tau\alpha$ spectrum is based on an estimate of H_2O column thickness that is too high by 0.4 pr cm. Again, D was taken as 1.5 times the original MDQ. The resulting $P(T|T)$ and $P(T|0)$ for $R=0.075$ are ~ 0.985 and ~ 0.055 , respectively. Thus we can say, generally, that real world effects do not increase the MDQ of SO_2 by more than a factor of 1.5, if spectral masking is used in the correlation processing, and if pre-whitening can be assumed effective in essentially eliminating the effects of background temperature/emissivity differences in the two IFOV's.

5.6.2 The HCl 2900-3000 cm^{-1} Detection Band

The normalized contrast spectral radiance $\tau\alpha + \xi/D$ for $D = 2.5 \times 10^9$ (molec/ cm^2)(W/ cm^2 sr cm^{-1}) is shown in Fig. 5.8a. This value of D is the MDQ for this band for a dwell time of 10 seconds. Spectral elements were masked out if their predicted transmittance was less than 0.45, which reduced the effective number of elements from 1000 to 617. Again, the plotted contrast of the masked elements is equal to the mean contrast of the remaining elements. Of course, for HCl, which has a very sparse emission spectrum, it would have been better to use the HCl spectral absorption coefficient as a criterion for masking, but it was easier to use the same type of criterion that was applied to SO_2 . Figure 5.8b shows the normalized reference contrast spectrum $\tau\alpha$ plotted to the same scale. Figure 5.8 represents the case of 0.2 pr cm excess H_2O in IFOV1.

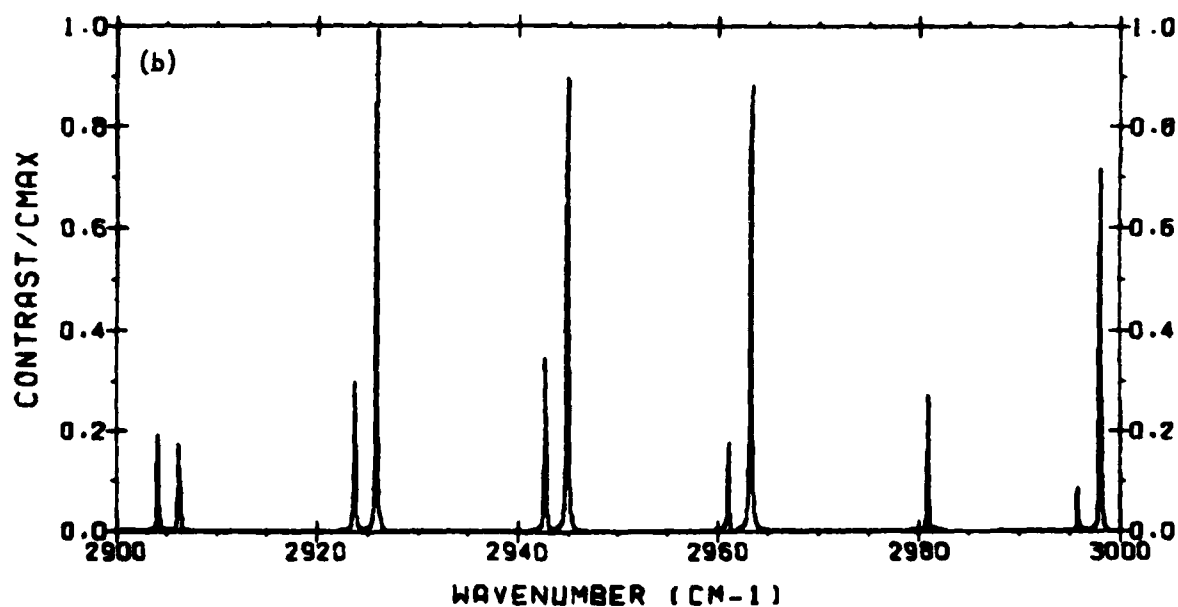
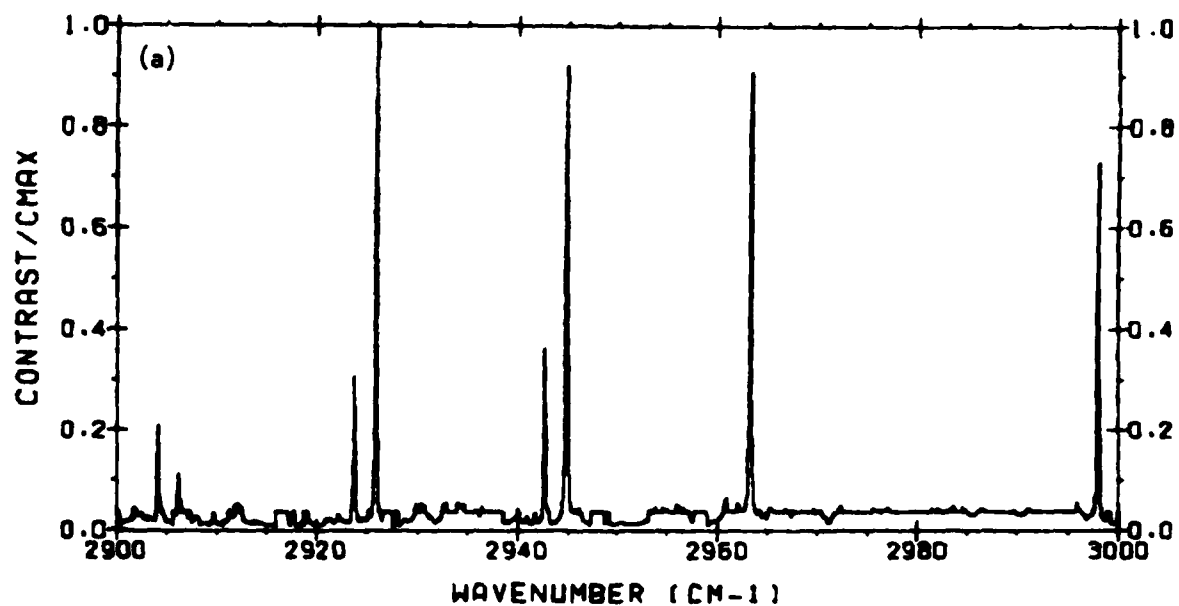


Figure 5.8 Part (a): Normalized contrast spectral radiance $\tau + \xi/D$ for the HCl 2900-3000 cm^{-1} detection band for $D = 2.9 \times 10^9$ (molec/cm^2) ($\text{W}/\text{cm}^2 \text{sr cm}^{-1}$). IFOV1 contains 0.2 pr cm more H_2O than IFOV2.

Part (b): The normalized spectral contrast τ plotted to the same scale as part (a).

Figure 5.9 shows the corresponding normalized contrast spectra when the excess H_2O is in IFOV2, with the HCl, rather than in IFOV1. The number of spectral elements that survived the masking criterion is 606.

The detection and false detection probabilities for the interference cases represented in Figs. 5.8 and 5.9, were found to be approximately 0.945/0.005 and 0.945/0.007, respectively, for a threshold value $R=0.1$. These values may be compared to the 0.955/0.02 probabilities obtained in the ideal case for $R=0.075$ with no spectral masking. This does not imply that the interferences improve performance, but rather that spectral masking would have resulted in slightly better HCl detection performance in the ideal case (as a result of increased variance σ_0^2 for the reference spectrum). These results show that interference type b has an insignificant effect on the MDQ for HCl.

5.6.3 The HBr 2450-2650 cm^{-1} Detection Band

Figure 5.10a gives the normalized spectral contrast $\tau\alpha + \xi/D$ for HBr when the quantity present is the MDQ for $t_d = 10$ seconds, and the excess H_2O is in IFOV1. The selected transmittance threshold is 0.65, which reduces the number of spectral elements from 2000 to 1805. Figure 5.10b gives the reference spectrum $\tau\alpha$.

For the ideal case with no spectral masking the MDQ corresponds to $P(T|T) = 0.942$ and $P(T|0) = 0.008$ for a threshold $R=0.06$. The detection and false detection probabilities corresponding to the interference case represented in Fig. 5.10 are approximately 0.92 and 0.02. Since these values represent acceptable performance, we can say that interference type b has an insignificant effect on the MDQ of HBr when the revised correlation procedure is used. The revised method is effective in spite of the fact that the

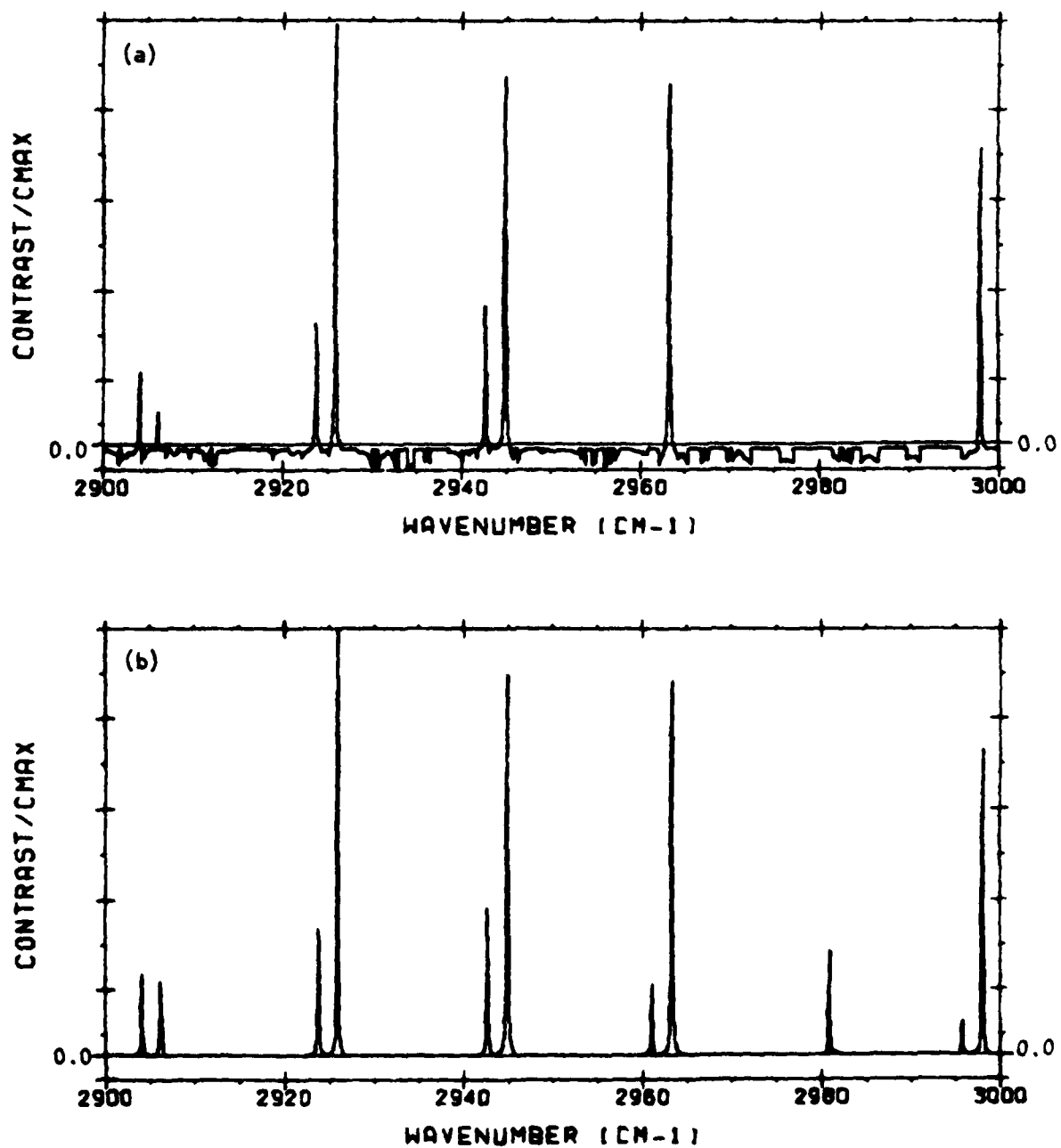


Figure 5.9 Same as Fig. 5.8, except that IFOV2 contains 0.2 pr cm more H_2O than IFOV1.

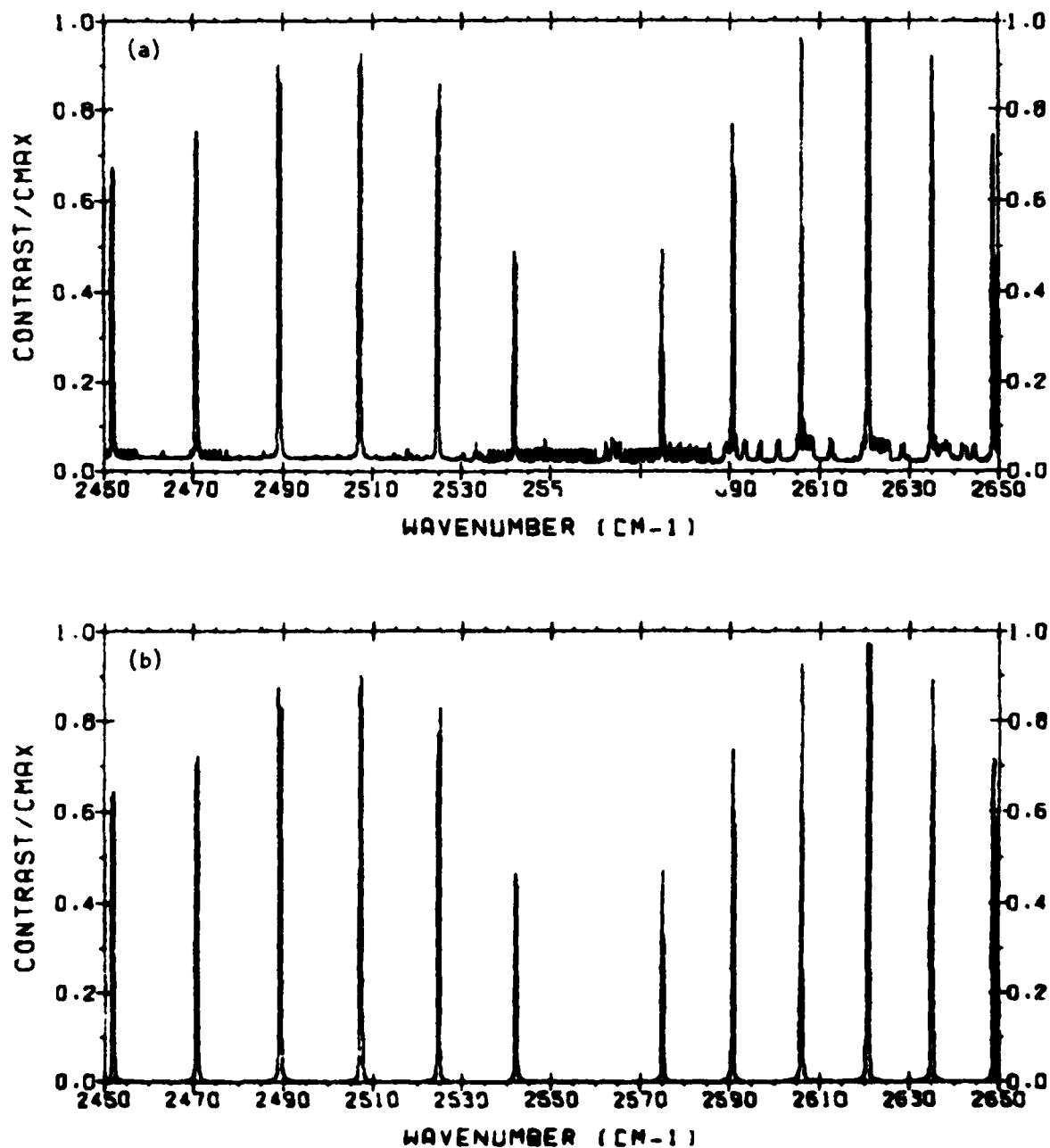


Figure 5.10 Part (a): Normalized contrast spectral radiance $\tau + \xi/D$ for the HBr 2450-2650 cm^{-1} detection band for $D = 2.44 \times 10^{10}$ (molec/cm^2) ($\text{W}/\text{cm}^2 \text{sr cm}^{-1}$). IF0V1 contains 0.2 pr cm more H_2O than IF0V2.

Part (b): The normalized spectral contrast τ plotted to the same scale as part (a).

transmittance envelope has a large variation over the blue wing of the $4.3 \mu\text{m}$ CO_2 band ($2450\text{--}2530 \text{ cm}^{-1}$) (see the HBr transmittance plot in Vol. II).

It should be noted that a significant part of the interference is attributable to the $\text{N}_2\text{O}(2\nu_1)$ band between 2525 and 2590 cm^{-1} . This band appears in the radiance contrast spectrum ξ because of the different amounts of H_2O below the N_2O in the two IFOV's. However, the effect of the $\text{N}_2\text{O}/\text{H}_2\text{O}$ is small when spectral elements are excluded on the basis of the predicted transmittance. For both the HCl and HBr detection bands a modest improvement in performance could be realized by excluding from the correlation nearly all spectral elements not containing HCl or HBr lines. This improvement would be realized in both the ideal and non-ideal cases, since its principal effect is to increase the apparent variance σ_0^2 of the reference spectrum $\tau\alpha$. The same argument applies to all species with sparse line spectra.

For HBr we also computed the effects of different background temperatures in the two IFOV's (without any difference in the H_2O column thicknesses). The computation is intended to show that prewhitening of the observed contrast radiance spectrum is an important part of the spectral correlation processing. Figure 5.11 shows the normalized spectral contrast $\tau\alpha + \xi/D$ when the background surface in IFOV1 is 10°C cooler than the background in IFOV2 (290K vs 300K). The same spectral elements have been excluded as a result of thresholding on the predicted transmittance, but now the spectral radiance differences in the N_2O band, in the H_2O lines above 2590 cm^{-1} , and in another atmospheric band below 2490 are very large as a result of the large background temperature difference. There is also a large variation in the continuum level of ξ/D that results from both the variation in atmospheric transmittance envelope

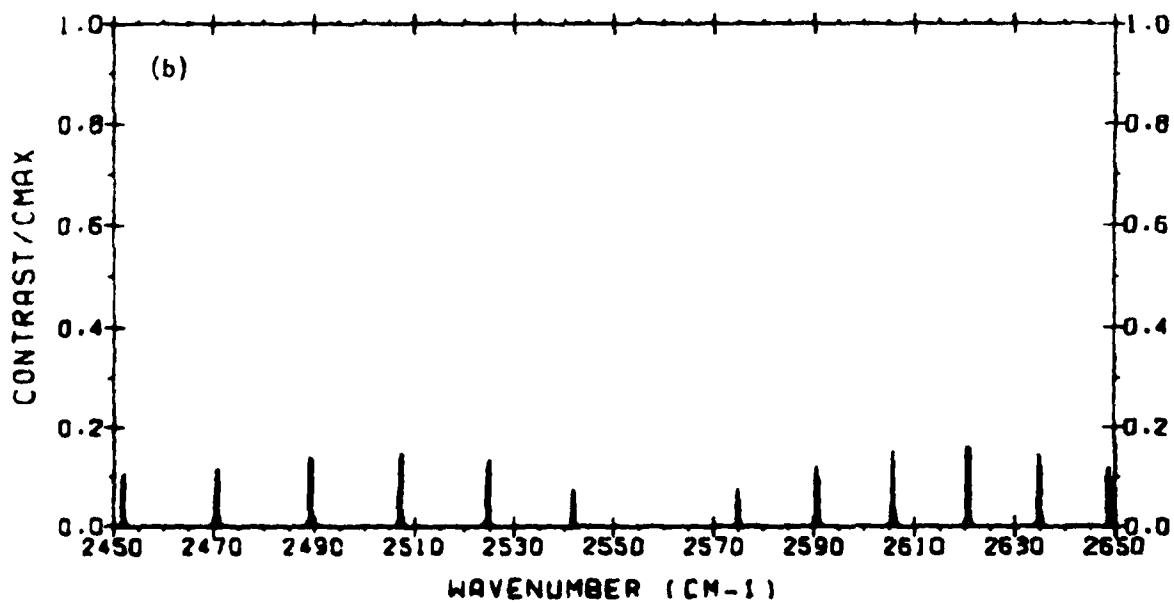
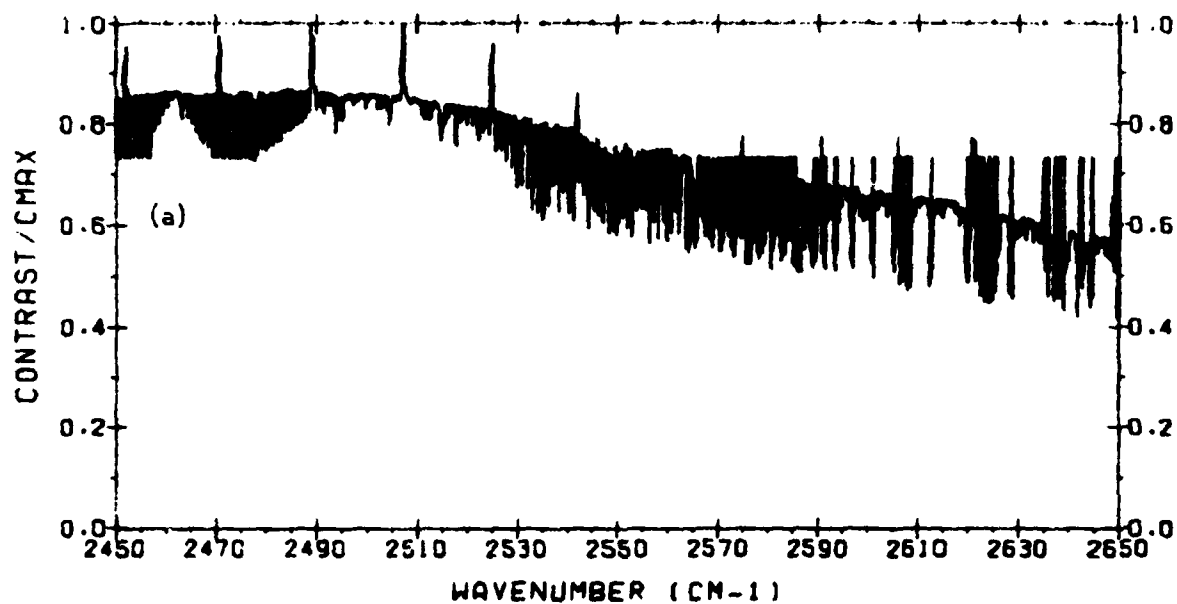


Figure 5.11 Same as Fig. 5.10, except the IFOV's have equal column thicknesses of H_2O and surface temperatures that differ by 10 degrees (290K² for IFOV1 and 300K for IFOV2).

and the different Planck function spectral slopes for the two background temperatures. Figure 5.11b shows the reference τ_a spectrum plotted to the same scale as Fig. 5.11a. If detection of HBr were based on the correlation of Figs. 5.11a and 5.11b (with no attempt to prewhiten Fig. 5.11a) the detection and false detection probabilities would be approximately 0.66 and 0.023, respectively. In other words, the occurrence of 10-degree surface temperature variations over a distance of 10 meters would lead to unacceptable performance unless an effective prewhitening scheme is implemented prior to spectral correlation.

The general features of Fig. 5.11a suggest that standard methods of prewhitening would not be effective unless they are preceded by somewhat elaborate methods of spectral rejection. Effective spectral rejection methods can probably be devised on the basis of *a priori* knowledge (e.g., the predictions of FASCOD1). It is also probable that useful spectral rejection methods must be devised individually for each of the detection bands of interest.

REFERENCES

1. System Design Study, SSG, Inc. (1979). Final report on Utah State University Subcontract SC-79-080 (U.S. Air Force prime Contract F19628-77-C-0203).
2. Down-Looking Interferometer Study, Bartlett Systems, Inc. (1977). Report BSI-7711, final report on Utah State University P.O. #33349 (U.S. Air Force prime Contract F19628-74-C-0130).
3. Vanasse, G.A., Stair, A.T. Jr., Shepherd, O., and Reidy, W.P. (1977) Background Optical Suppression Scheme (BOSS), AFGL-TR-77-0135
4. Selby, J.E.A., Kneizys, F.X., Chetwynd, J.H. Jr., and McClatchey, R.A. (1978) Atmospheric Transmittance/Radiance: Computer Code LOWTRAN 4, AFGL-TR-78-0053.
5. Clough, S.A., and Kneizys, F.X. (1979) Convolution algorithm for the Lorentz function, Appl. Opt. 18:2329.
6. Luther, F.M. (1976) Lawrence Livermore Laboratory First Annual Report to the High Altitude Pollution Program, FAA-EQ-77-6.
7. Kruse, P.W., McGlauchlin, L.D., and McQuistan, R.B. (1962) Elements of Infrared Technology, Wiley & Sons, New York, p. 361.
8. Ibid, p. 359.
9. Rosen, R.D., Salstein, D.A., and Peixoto, J.P. (1979) Mon. Wea. Rev. 107:26.

APPENDIX A

PROOF OF EQUATIONS 10 AND 11 IN SECTION 2

As stated, we will assume the atmospheric spectral transmittance and gas spectral absorption coefficient can be predicted exactly; i.e., $\tau'_v \alpha'_{gv}$ can be replaced by $\tau_v \alpha_{gv}$ in Eq. (9) of Section 2. We will still denote the spectral mean of $\tau'_v \alpha'_{gv} = \tau_v \alpha_{gv}$ by μ' , and the mean of ΔN_v by μ . With the above assumption, $\mu = D\mu'$ (see Eq. 8 in Section 2).

Let σ' denote the standard deviation of the reference spectrum:

$$\sigma' = \left[\langle (\tau_v \alpha_{gv} - \mu')^2 \rangle \right]^{1/2} \quad (A-1)$$

Equation (9) of Section 2 can then be written

$$\begin{aligned} \rho &= \frac{\langle (\Delta N_v - \mu) (\tau_v \alpha_{gv} - \mu') \rangle}{\sigma' \left[\langle (\Delta N_v - \mu)^2 \rangle \right]^{1/2}} \\ &= \frac{\langle [D(\tau_v \alpha_{gv} - \mu') + n_v] (\tau_v \alpha_{gv} - \mu') \rangle}{\sigma' \left\{ \langle [D(\tau_v \alpha_{gv} - \mu') + n_v]^2 \rangle \right\}^{1/2}} \end{aligned} \quad (A-2)$$

where the second form results from substituting Eq. (8) and $\mu = D\mu'$ into the first form.

Expand the numerator product and squared denominator term in (A-2), and then evaluate the spectral averages term-by-term. The result is shown in (A-3) where we have used (A-1) and written the spectral averages in terms of sums over M resolved spectral elements (the particular spectral elements that would be selected in the band of a given species to provide optimal detection).

$$\rho = \frac{D\langle(\tau_v \alpha_{gv} - \mu^-)^2\rangle + \langle n_v(\tau_v \alpha_{gv} - \mu^-)\rangle}{\sigma^- \left[D^2\langle(\tau_v \alpha_{gv} - \mu^-)^2\rangle + 2D\langle n_v(\tau_v \alpha_{gv} - \mu^-)\rangle + \langle n_v^2 \rangle \right]^{1/2}}$$

$$= \frac{D(\sigma^-)^2 + \frac{1}{M} \sum n_v(\tau_v \alpha_{gv} - \mu^-)}{\sigma^- \left[D^2(\sigma^-)^2 + \frac{2D}{M} \sum n_v(\tau_v \alpha_{gv} - \mu^-) + \frac{1}{M} \sum n_v^2 \right]^{1/2}} \quad (A-3)$$

Equation (A-3) for ρ can be simplified by making use of the general rule for determining the statistics of a weighted sum of independent normal variates: If v_1, v_2, \dots, v_n are independent normally distributed random variates with means and standard deviations $(\mu_1, \sigma_1), (\mu_2, \sigma_2), \dots, (\mu_n, \sigma_n)$, then the weighted sum $v = a_0 + a_1 v_1 + a_2 v_2 + \dots + a_n v_n$ is normally distributed with mean and standard deviation

$$m = a_0 + a_1 \mu_1 + a_2 \mu_2 + \dots + a_n \mu_n,$$

$$\sigma = (a_1^2 \sigma_1^2 + a_2^2 \sigma_1^2 + \dots + a_n^2 \sigma_n^2)^{1/2}. \quad (A-4)$$

Thus, the weighted sum

$$q \equiv \sum n_v(\tau_v \alpha_{gv} - \mu^-) \quad (A-5)$$

appearing in the numerator and denominator of (A-3) is a normal variate with zero mean (since the n_v have zero means) and standard deviation

$$\sigma = \left[\sum (\tau_v \alpha_{gv} - \mu^-)^2 \sigma_n^2 \right]^{1/2}$$

$$= \sigma_n M^{1/2} \left[\frac{\sum (\tau_v \alpha_{gv} - \mu^-)^2}{M} \right]^{1/2}$$

$$= \sqrt{2} \overline{NESR} M^{1/2} \sigma^- \quad (A-6)$$

where $\sigma_n = \sqrt{2 \text{ NESR}}$ is the standard deviation of the noise n_v .

Now, consider the scaled sum s of independent unit normal variates x_i (which have zero mean and unit standard deviation):

$$s = \sqrt{2 \text{ NESR}} \sigma' \sum_{i=1}^M x_i. \quad (\text{A-7})$$

By the addition rule for normal variates, s is normal with zero mean and standard deviation

$$\sigma = \sqrt{2 \text{ NESR}} \sigma' M^{1/2}; \quad (\text{A-8})$$

i.e., the random variate s is statistically identical to q , which means that the sum (A-7) can be used in place of (A-5). We note also that any of the random noise samples n_v is identical to $\sqrt{2 \text{ NESR}} x_i$, where x_i is unit normal; thus, the last term in the denominator radical in (A-3) can be written

$$\frac{1}{M} \sum n_v^2 = \frac{2(\text{NESR})^2}{M} \sum_{i=1}^M x_i^2. \quad (\text{A-9})$$

Substituting s for q in (A-3), and substituting (A-9) in the denominator, we obtain

$$\rho = \frac{D(\sigma')^2 + \frac{\sqrt{2 \text{ NESR}} \sigma'}{M} \sum_{i=1}^M x_i}{\sigma' \left[D^2(\sigma')^2 + \frac{2D \sqrt{2 \text{ NESR}} \sigma'}{M} \sum_{i=1}^M x_i + \frac{2(\text{NESR})^2}{M} \sum_{i=1}^M x_i^2 \right]^{1/2}} \quad (\text{A-10})$$

For $D=0$ (no target gas present)

$$\rho(D=0) = \frac{1}{M^{1/2}} \frac{\sum x_i}{\left[\sum x_i^2\right]^{1/2}} \quad (\text{A-11})$$

which is the same as Eq. (11) of Section 2.

Note that the bracketed term in the denominator of (A-10) is the sum of a perfect square, equal to

$$\begin{aligned} & \frac{1}{M} \sum_{i=1}^M \left[D^2 (\sigma')^2 + 2(D\sigma') \sqrt{2 \text{NESR}} x_i + 2(\text{NESR})^2 x_i^2 \right] \\ &= \frac{1}{M} \sum_{i=1}^M \left[D\sigma' + \sqrt{2 \text{NESR}} x_i \right]^2 \end{aligned}$$

Using this fact and dividing numerator and denominator by $D(\sigma')^2$, we find that for $D \neq 0$,

$$\rho = \frac{1 + \frac{1}{M} \frac{1}{Z} \sum_{i=1}^M x_i}{\left[\frac{1}{M} \sum_{i=1}^M \left(1 + \frac{1}{Z} x_i \right)^2 \right]^{1/2}} \quad (\text{A-13})$$

where $Z = (\sigma'D)/(\sqrt{2 \text{NESR}})$ is the ratio of rms signal to rms noise in the contrast radiance spectrum ΔN_v . This result is the same as Eq. (10) of Section 2.

APPENDIX B

VALIDITY OF THE APPROXIMATION $D^* \sim F^\#$

From Eqs. (22) thru (24) of Section 2.5, it is seen that the approximation requires that

$$\left[\frac{\tau}{(2F^\#)^2} + \frac{\tilde{\epsilon}}{1 + (2F^\#)^2} \right]^{-1/2} \approx CF^\# \quad (B-1)$$

for some choice of the constant C (assuming the optics and scene temperature are equal). If we let $\tau = 0.261$ and $\tilde{\epsilon} = 0.249$, and choose C such that the error in (B-1) is zero at $F^\# = 1$, then the error for $F^\#$'s up to 5.0 is as shown in Table B-1. Note that the maximum error is five percent.

Table B-1 Error in D^* Values Scaled Linearly with $F^\#$

$F^\#$	Percent Error in $D^* \sim F^\#$ ($C = 2.948$)
1	0
1.5	2.7
2.0	3.7
2.5	4.3
3.0	4.6
4.0	4.9
5.0	5.0

